Spring 2010

Development of ground-based search -coil magnetometer systems in the polar regions and studies of ULF Pc 1--2 wave propagation in the ionospheric waveguide

Hyomin Kim
University of New Hampshire, Durham

DEVELOPMENT OF GROUND-BASED SEARCH-COIL MAGNETOMETER SYSTEMS IN THE POLAR REGIONS AND STUDIES OF ULF Pc 1–2 WAVE PROPAGATION IN THE IONOSPHERIC WAVEGUIDE

BY

HYOMIN KIM

M.S. in Engineering, Dartmouth College 2004

DISSERTATION

Submitted to the University of New Hampshire
in Partial Fulfillment of
the Requirements for the Degree of

Doctor of Philosophy

in

Mechanical Engineering

May, 2010

This dissertation has been examined and approved.

Dissertation Director, Marc R. Lessard, Research Associate Professor of Earth, Oceans, and Space and Physics

Kent A. Chamberlin, Professor of Electrical and Computer Engineering

Ronald R. Clark, Professor Emeritus of Electrical and Computer Engineering

Richard E. Denton, Research Professor of Physics and Astronomy, Dartmouth College

Mark J. Engebretson, Professor of Physics, Augsburg College

Charles J. Farrugia, Research Associate Professor of Earth, Oceans, and Space and Physics

Date

ACKNOWLEDGMENTS

It has been a long journey since I left my home country, South Korea, and began a different but challenging life as a graduate student in the States. During the journey, there have been times when I wasn't sure that I had chosen the right path and this day would come. I can confidently assure myself that I have learned much more than space physics during the time spent in my graduate program. Whenever I felt that I was coming to a dead end, I tried to remind myself of the motto that I like - "Enjoy it if you can't avoid it." Whenever moments of discouragement and hardship occurred, a belief that taking a one step back leads to a leap forward strengthened my spirit. In taking classes and conducting research, I realize more and more that the learning process is to make ourselves aware of not only how much we know but also how much we don't know. What Newton said - "I do not know what I may appear to the world, but to myself I seem to have been only like a boy, playing on the seashore and diverting myself in now and then finding a smoother pebble or prettier seashell than ordinary, while the great ocean of truth lay all undiscovered before me." guided me not to make myself full of conceit.

This work would not have been completed without the valuable support and advice of many people. First of all, I heartily thank my advisor, Marc R. Lessard, whose encouragement, supervision and support enabled me to develop an understanding of the subject and pursue my academic goal in Systems Design to bridge space science and engineering. He introduced me to a variety of experiences in my research field such as the construction and installation of the search-coil magnetometer system and data analysis. His mentorship was paramount in encouraging me to grow not only as an experimentalist in space physics but also as an independent thinker. My trip to the Arctic and Antarctic regions for

the installation of the instruments will remain one of my most memorable experiences. I also acknowledge that this research was supported by National Science Foundation grants ANT-0838910, ANT-0839938, and ANT-0636874 to the University of New Hampshire.

I thank Mark Engebretson of Augsburg College for his knowledge and patience in answering my numerous questions about data analysis. I appreciate his time and effort for being a co-author of my research paper as well as a member of my thesis committee. His detailed information about ULF wave observations using magnetometer data formed one of the most critical parts in my thesis. Likewise, my thanks go to the other members of my thesis committee, Richard Denton of Dartmouth College, Kent Chamberlin, Ronald Clark, and Charles Farrugia, who provided important assistance and advice and inspired me to solve challenging problems that I encountered and keep my thesis topic on the right track. I thank Hermann Lühr of Helmholtz Centre Potsdam, GFZ German Research Centre for Geosciences for providing the CHAMP satellite data and very helpful information about data analysis. I would also like to thank a number of station crews in Svalbard, Greenland, Canada, and Antarctica for their reliable support in performing remote-data archive and monitoring instruments.

I have also had the pleasure of being in my research group, Magnetosphere-Ionosphere Research Lab (MIRL) at the Space Science Center, which is filled with numerous and exciting research projects and enthusiastic undergraduate and graduate students. I would like to thank Paul Riley for his profound knowledge and valuable experience in building and testing hardware. He was my company on field trips for the installation of the instruments that we developed. Without his significant contribution to the design, construction, and test of search-coil magnetometers, this thesis would not exist. I am grateful to Mark Widholm who provided me with valuable information about electronics and lab setups. Two undergraduate students, Chris Black and Matthew Young, full of academic passion, have

been always very helpful to build instruments and analyze data. Other graduate students in my group, Sarah Jones, Allison Jaynes, and Brent Sadler, have always been great friends and shared a great deal of useful information.

Most importantly, I would like to thank my loving wife, Yun-chu Cheong, who has always been supporting and encouraging me with her unwavering love, quiet patience, and firm belief in God. Whenever I felt overwhelmed and discouraged, she always stood next to me with her faith in me. Finally, my endless thanks should go to my parents, my brother, Hyojin, and his family - his wife, Heesung and their newborn baby, Ian, for their inestimable love and support in many ways, without which my study in the States as well as the completion of my thesis would not be possible.

Table of Contents

Acknowledgments iii

List of Figures x

List of Tables xxii

Abstract xxiii

1 Introduction 1

1.1 Solar-Terrestrial Environment 2

1.2 System Engineering of Magnetometer Project for Space Research 4

1.3 Waves in Space Plasma 5

1.3.1 Generation of Waves in Plasma 5

1.3.2 Types of Plasma Waves 7

1.3.3 Polarization of Waves 11

1.3.4 Geomagnetic Pulsations 12

1.4 Wave Propagation in the Ionospheric Waveguide 15

2 Development of Search-Coil Magnetometers 19

2.1 Introduction 19

2.2 Principle of Operation 20

2.3 Technical Details of the UNH ULF Search-Coil Magnetometer 22

2.3.1 Search-Coil Magnetic Sensor 23

2.3.2 Main Analog Electronics 25

2.3.3 Data Acquisition System 26

2.3.4 System Specification 27

2.4 Tests 30
2.4.1 Polarity Test 30
2.4.2 Frequency Response Test 30
2.4.3 Resolution Test 35
2.4.4 Deviation Tests 37
2.5 Installation in the Polar Regions 38

3 Ducting Characteristics of Pc 1 Waves at High Latitudes on the Ground and in Space 42
3.1 Introduction 42
3.2 Instrumentation and Data 45
3.3 Observations and Interpretations 48
3.3.1 Spectral Power Attenuation 51
3.3.2 Propagation Speed 54
3.3.3 Polarization 55
3.3.4 Spatial Extent of Wave Injection Region 60
3.4 Summary 67

4 Statistical Study of Pc 1–2 Wave Propagation Characteristics in the High-Latitude Ionospheric Waveguide 69
4.1 Introduction 69
4.2 Data Analysis 72
4.2.1 Instrumentation 72
4.2.2 Data Survey 73
4.3 Example Events 75
4.3.1 Example 1: Mar. 5, 2007 76

4.3.2 Example 2: Mar. 24, 2007 82
4.3.3 Example 3: Oct. 7, 2007 84
4.4 Statistical Results 91
4.4.1 MLT Occurrences 91
4.4.2 Spectral Power Attenuation and Ionospheric Conductivity 93
4.4.3 Polarization Characteristics 98
4.5 Summary 103

5 Summary and Conclusions 106
5.1 Development of Search-Coil Magnetometers 108
5.2 Ducting Characteristics of Pc 1 Waves at High Latitudes on the Ground and in Space 109
5.3 Statistical Study of Pc 1–2 Wave Propagation Characteristics in the High-Latitude Ionospheric Waveguide 110
5.4 Concluding Remarks 112

Appendices 113

Appendix A Polarization Analysis Technique 114
A.1 Polarization of Plane Waves 114
A.2 Polarization Analysis for Geomagnetic Pulsations 117
A.2.1 Theory 117
A.2.2 Implementation 121

Appendix B UNH ULF Search-Coil Magnetometer Technical Details 124
B.1 Search-Coil Magnetic Sensor Spool and Wiring Diagram 124
B.2 Electrical schematic of Preamp 126
B.3 Electrical schematic of Main Analog Electronics 126

B.4 Magnetometer System Cable Connection Diagram 126

B.5 Frequency Response Characterization of Search-Coil Magnetometer System Using Equivalent Circuit Model 129

B.5.1 Search-Coil Magnetic Sensor Model 129

B.5.2 Passive Low-Pass Filter Model 130

B.5.3 Active Low-Pass Filter Model 131

B.5.4 Modeling of the Overall Magnetometer System 133

APPENDIX C THE CHAMP SATELLITE FLUXGATE MAGNETOMETER DATA COORDINATE TRANSFORMATION 138

BIBLIOGRAPHY 141

List of Figures

1-1 The Earth's magnetosphere and its current system (with permission from Anthony T.Y. Lui at JHU/APL). 3

1-2 A sketch showing one use of the "system" of ground-based magnetometers, which provides spatially and temporally extended observations of the geomagnetic pulsations. 5

1-3 Charged particles gyrating around a guiding center in a uniform magnetic field. 6

1-4 Schematic illustration of frozen-in flux. In MHD fluid flow, the magnetic flux is frozen in to the fluid so that the fluid can move with the field lines. Therefore, the total magnetic flux through surface remains unchanged. . . . 9

1-5 Types of waves in a magnetized plasma. 11

1-6 Profiles of neutral atmospheric temperature and ionospheric electron density with the various layers designated (Courtesy of Bhamer, from Wikipedia public domain). 16

1-7 Conceptual sketch of the propagation of EMIC waves from the equatorial region in the magnetosphere to the ionospheric waveguide. 17

2-1 Schematic of search-coil magnetometer showing principle of operation based on Faraday's Law of induction. When the magnetic flux density through the coil changes, a voltage (emf) is induced in the coil. 21

2-2 Schematic diagram of the UNH ULF search-coil magnetometer system. . . . 23

2-3 UNH ULF search-coil magnetometer system. 24

2-4 Preamp board of the UNH ULF search-coil magnetic sensor. 25

2-5 UNH ULF magnetic sensor with annotations. 26

2-6 UNH ULF search-coil magnetometer main analog electronics. 27

2-7 PC104 module stack in the data acquisition system enclosure. The module consists of analog-to-digital converter (ADC), Microcontroller, GPS receiver, VGA graphic card, power supply board, and main analog electronics. 28

2-8 (a) Definition of signal polarity of the UNH ULF search-coil magnetic sensor; (b) test signal for sensor coil polarity test; (c) magnetometer output signal in response to the test signal. 31

2-9 A solenoid and an RC circuit for polarity test. This device is used externally near the search-coil magnetic sensor to test the sensor polarity. 32

2-10 (a) Square wave test signal generated by the main analog electronics of the UNH ULF search-coil magnetometer system; (b) output signal in response to the rising and falling transition of the test signal. 32

2-11 Test setup for frequency response and resolution characterization of the search-coil magnetometer system. 33

2-12 Test solenoid used for frequency response and resolution tests. 33

2-13 Bode plots of frequency response to the voltage output (top) and to the magnetic field (bottom) of the UNH ULF search-coil magnetic sensor (with preamp), showing that the frequency response is 0 – 10 Hz (specified at -3 dB corner frequencies). Note that DC magnetic field (when $f = 0$) is not detected by a search-coil magnetic sensor. 34

2-14 Bode plots of frequency response to the voltage output (top) and to the magnetic field (bottom) of the UNH ULF search-coil magnetometer system, showing that the frequency response is 0 – 2.5 Hz (specified at −3 dB corner frequencies). Note that DC magnetic field (when $f = 0$) is not detected by a search-coil magnetometer. 35

2-15 Screenshot of spectrum analyzer showing the search-coil magnetometer response to a 1 Hz (left) and a 2 Hz (right) test signal when the peak is 3.0 dB above the noise floor. This peak intensity corresponds to 8.8 pT and 5.5 pT, respectively. 36

2-16 Test setup for search-coil magnetic sensor deviation test. 37

2-17 Bode plot of frequency response for deviation tests of the 18 preamps (top) and the 15 main analog electronics (bottom). 38

2-18 (a) Polarity setup of the ULF search-coil magnetic sensor; definition of coordinate systems applied to the sensor installation and orientation of the sensors for ground installation (b) in the northern hemisphere and (c) in the southern hemisphere. 40

2-19 UNH ULF search-coil magnetic sensors (X and Y components) installed under the ground in Ny Ålesund, Svalbard. 41

3-1 Map of Antarctica showing the ULF search-coil magnetometer array used for this study. The geomagnetically most poleward station, P5, and the other four stations, P1, P2, SPA and HBA are aligned well with the magnetic meridian. This map also shows the southern hemisphere ground track of the magnetic field lines traversed by the CHAMP satellite from 0835 to 0845 UT on March 23 2007, based on data from the Satellite Situation Center Web utility, available at http://sscweb.gsfc.nasa.gov. 47

3-2 Stacked 0 – 1 Hz Fourier spectrograms in the X (north-south) (left panels) and Y (east-west) (right panels) components of the search-coil data showing the ULF Pc 1 waves recorded at the Antarctic stations, Halley (HBA), P2, South Pole (SPA), P1, and P5 from 0800 to 1300 UT on March 23, 2007. The stations are located along the magnetic meridian covering from geomagnetic latitudes of $-62°$ to $-87°$ with the lowest latitude station at the bottom of the plot. Spectral power attenuation as the waves are ducted poleward is clearly registered. X axis data from AGO P5 were unavailable during this interval. Note that the time intervals of Figure 3-3, Figure 3-5, and Figure 3-8 are indicated. 49

3-3 Temporal and spectral structures of the ULF Pc 1 waves (called "pearls") measured from HBA in a shorter time scale (from 1020 to 1050 UT). Wave modulation with approximately 3 min period is clearly shown. Note that the event during this period is indicated in Figure 3-2. 50

3-4 Power spectra ($\log_{10}$ power versus frequency) of the ULF Pc 1 events observed by the Antarctic search-coil array and wave power attenuations (in dB) over the distance from HBA (in km) at four selected frequencies (0.3, 0.4, 0.5, and 0.6 Hz) during the two time periods, (a) 0915 – 0945 UT and (b) 0945 – 1015 UT. The graphs for each time period display the results from both X and Y components. 52

3-5 Propagation time delay in the temporal and spectral structures observed from HBA and SPA. This event period is band-pass filtered over 0.3 – 0.5 Hz for the structures to be seen more clearly. The wave arrival time is delayed by $\sim$ 18 sec between the stations, which are separated by $\sim$ 1600 km. The wave packets and the spectral patterns that are compared for the timing are indicated by vertical lines. Note that the event during this period is indicated in Figure 3-2. 55

3-6 Polarization ellipticity (ε) of the ULF Pc 1 waves observed by the ground array from 0800 to 1300 UT on March 23, 2007 in a plot of frequency versus time. The ellipticity is shown in a color scale with -1 being LH circular polarization (negative ellipticity) and $+1$ being RH circular polarization (positive ellipticity). LP is defined as having $|\varepsilon| < 0.2$. Note that the time intervals of Figure 3-3, Figure 3-5, and Figure 3-8 are indicated. 57

3-7 Polarization angle (θ) of the ULF Pc 1 waves observed by the ground array from 0800 to 1300 UT on March 23, 2007 in a plot of frequency versus time. The angle change ranges between $-90°$ and $+90°$. The sign represents the direction of the angle with respect to the magnetic meridian in the north-south direction (X component in the magnetometer data) with positive angle being counterclockwise and negative angle being clockwise. Note that the time intervals of Figure 3-3, Figure 3-5, and Figure 3-8 are indicated. 59

3-8 Stacked spectrograms of the Y-component of the HBA search-coil data, the three components ($b_{\parallel}$, $b_{\perp\theta}$, and $b_{\perp\varphi}$) of the magnetic field data and the polarization ellipticities (in three ranges: LP, LHP, and RHP) from the fluxgate magnetometer of the CHAMP satellite during the event in this study. Band-limited ULF waves over the frequency band ($\sim$ 0.4 – 0.5 Hz) are observed approximately from 0840 to 0843 UT on Mar. 23, 2007. The satellite crossings over SPA, P2, and HBA are shown with the arrows. Note that the event during this period is indicated in Figure 3-2 61

3-9 Time-series plot of the two perpendicular components, meridional ($b_{\perp\theta}$) and azimuthal ($b_{\perp\varphi}$) perturbations from the CHAMP satellite magnetic field data (first and second panels, respectively) and the three components, B_x, B_y, and B_z, of the search coil magnetometer at Halley Station, Antarctica (third, fourth, and fifth panels, respectively) during a Pc 1 wave event from 0840 to 0844 UT on Mar. 23, 2007. 64

4-1 Stacked 0 – 1 Hz Fourier spectrograms in the Y (east-west) components of the search-coil data showing the ULF Pc 1 waves recorded at the Antarctic stations, Halley (HBA), AGO P2, South Pole (SPA), P1 and P5 from 0200 to 0600 UT on Mar. 5, 2007 (Example 1). 78

4-2 Power spectra ($\log_{10}$ power versus frequency) of the ULF Pc 1 events observed by the Antarctic search-coil array and the wave power attenuation (in dB) over the distance from HBA (in km) at four selected frequencies (0.55, 0.62, 0.69, and 0.76 Hz) during the two time periods, (a) 0220 – 0240 UT and (b) 0240 – 0300 UT on Mar. 5, 2007. The graphs for each time period display the results from both X and Y components. 79

4-3 Polarization ellipticity (ε) of the ULF Pc 1 waves observed by the Antarctic search-coil array on Mar. 5, 2007 in a plot of frequency versus time. Each panel is represented in a color scale with -1 being LH circular polarization (negative ellipticity) and $+1$ being RH circular polarization (positive ellipticity). LP is defined as having $|\varepsilon| < 0.2$. 80

4-4 Polarization angle (θ) of the ULF Pc 1 waves observed by the Antarctic search-coil array on Mar. 5, 2007 in a plot of frequency versus time. The angle ranges between $-90°$ and $+90°$. The sign represents the direction of angle with respect to the magnetic meridian in north-south direction (X component) with positive angle being counterclockwise and negative angle being clockwise. The panels on the left and right present positive ($\theta \geq 0$) and negative ($\theta < 0$) angles, respectively. 81

4-5 Stacked 0 – 1 Hz Fourier spectrograms in the X (north-south) components of the search-coil data showing the ULF Pc 1 waves recorded at the Antarctic stations, Halley (HBA), AGO P2, South Pole (SPA), and P1 from 1900 to 2130 UT on Mar. 24, 2007 (Example 2). 83

4-6 Power spectra ($\log_{10}$ power versus frequency) of the ULF Pc 1 events observed by the Antarctic search-coil array and the wave power attenuation (in dB) over the distance from HBA (in km) at four selected frequencies (0.27, 0.31, 0.35, and 0.39 Hz) during the two time periods, (a) 2010 – 2030 UT and (b) 2100 – 2120 UT on Mar. 24, 2007. The graphs for each time period display the results from both X and Y components. 84

4-7 Polarization ellipticity (ε) of the ULF Pc 1 waves observed by the Antarctic search-coil array on Mar. 24, 2007 in a plot of frequency versus time. Each panel is represented in a color scale with -1 being LH circular polarization (negative ellipticity) and $+1$ being RH circular polarization (positive ellipticity). LP is defined as having $|\varepsilon| < 0.2$. 85

4-8 Polarization angle (θ) of the ULF Pc 1 waves observed by the Antarctic search-coil array on Mar. 24, 2007 in a plot of frequency versus time. The angle ranges between $-90°$ and $+90°$. The sign represents the direction of angle with respect to the magnetic meridian in north-south direction (X component) with positive angle being counterclockwise and negative angle being clockwise. The panels on the left and right present positive ($\theta \geq 0$) and negative ($\theta < 0$) angles, respectively. 86

4-9 Stacked 0 – 1 Hz Fourier spectrograms in the X (north-south) components of the search-coil data showing the ULF Pc 1 waves recorded at the Antarctic stations, Halley (HBA), AGO P2, South Pole (SPA), and P1 from 0420 to 0640 UT on Oct. 7, 2007 (Example 3). 87

4-10 Power spectra ($\log_{10}$ power versus frequency) of the ULF Pc 1 events observed by the Antarctic search-coil array and the wave power attenuation (in dB) over the distance from HBA (in km) at four selected frequencies (0.30, 0.38, 0.46, and 0.54 Hz) during the two time periods, (a) 0440 – 0500 UT and (b) 0600 – 0620 UT on Oct. 7, 2007. The graphs for each time period display the results from both X and Y components. 88

4-11 Polarization ellipticity (ε) of the ULF Pc 1 waves observed by the Antarctic search-coil array on Oct. 7, 2007 in a plot of frequency versus time. Each panel is represented in a color scale with -1 being LH circular polarization (negative ellipticity) and $+1$ being RH circular polarization (positive ellipticity). LP is defined as having $|\varepsilon| < 0.2$. 89

4-12 Polarization angle (θ) of the ULF Pc 1 waves observed by the Antarctic search-coil array on Oct. 7, 2007 in a plot of frequency versus time. The angle ranges between $-90°$ and $+90°$. The sign represents the direction of angle with respect to the magnetic meridian in north-south direction (X component) with positive angle being counterclockwise and negative angle being clockwise. The panels on the left and right present positive ($\theta \geq 0$) and negative ($\theta < 0$) angles, respectively. 90

4-13 MLT distribution of ULF Pc 1–2 ducting events in the year 2007. 92

4-14 MLT distribution of ULF Pc 1–2 ducting events - clear poleward propagation versus irregular propagation. 94

4-15 Frequency distribution of two different Pc 1–2 wave propagation types - clear poleward propagation versus irregular propagation. Note that the occurrences of each propagation type are normalized. 95

4-16 Spectral power attenuation versus frequency under three ionospheric sunlight conditions. 98

4-17 Frequency distribution of Pc 1–2 ducting events under three ionospheric sunlight conditions. Note that the occurrences in each sunlight condition are normalized. 99

4-18 Ellipticity occurrence percentiles over distance using the data from the Antarctic array. Note that the events under dark ionospheric condition are not included due to insufficient number of events. 100

4-19 Plots showing the relationship between spectral power attenuation and polarization ellipse major axis angle at HBA using the data from the Antactic array. 101

4-20 Horizontal spatial distributions of polarization patterns for incident wave (left) and transmitted wave on the ground (right). Circles drawn with a broken line and a solid line are demarcations of the polarization sense and the major axis direction, respectively (after Fujita & Tamao (1988)). 102

A-1 An example of rotation of a plane wave at $z = 0$ as a function of time: right-hand circular polarization as seen in a plane perpendicular to the direction of propagation. 115

A-2 An example of representation of a polarized field by the convention in electromagnetics. This type of representation is called a hodogram. Clockwise (CW) sense and counterclockwise (CCW) sense of the field trace are designated as left-hand polarization (LHP) and right-hand polarization (RHP), respectively. Note that the convention in optics applies in the opposite way - CW is RHP and CCW is LHP. 116

A-3 An example of a hodogram from a computer-generated signal of multiple frequencies, amplitudes, and phase angles, which mimics a natural signal. . 117

B-1 Spool winding diagram showing how the wire is wound around the spool. . 124

B-2 UNH ULF search-coil magnetic sensor wiring diagram. 125

B-3 Electrical schematic of the preamp circuit for the search-coil magnetic sensor. 126

B-4 Electrical schematic of the main analog circuit of the search-coil magnetometer system. 127

B-5 ULF search-coil magnetometer system cable connection diagram. 128

B-6 Search-coil magnetic sensor model used in this study. 130

B-7 Magnitude and phase frequency response of the search-coil magnetic sensor model. 131

B-8 First order passive low-pass filter model used in this study. 131

B-9 First order active low-pass filter model used in this study. 132

B-10 Magnitude and phase frequency response of the preamp model. 134

B-11 Magnitude and phase frequency response of the main analog circuit model (Block 1). 134

B-12 Magnitude and phase frequency response of the main analog circuit model (Block 2). 135

B-13 Magnitude and phase frequency response of the main analog circuit model (Block 3). 135

B-14 Magnitude and phase frequency response of the main analog circuit model (Block 4). 136

B-15 Magnitude and phase frequency response of the main analog circuit model (Blocks 1 to 4). 136

B-16 Magnitude and phase frequency response of the overall magnetometer system model without the search-coil magnetic sensor. 137

B-17 Magnitude and phase frequency response of the overall magnetometer system model with the search-coil magnetic sensor. 137

C-1 Schematic diagram showing coordinate transformation from the CHAMP satellite coordinate system to the new coordinate system used in this study. 140

List of Tables

1.1 The classification of ULF geomagnetic pulsations (Jacobs et al. 1964). . . . 13

3.1 Geographic and geomagnetic locations of the Antarctic stations used in this study. Geomagnetic coordinates, dipole L-values, and MLT MN in UT are obtained from NASA GSFC Modelweb Website, http://modelweb.gsfc.nasa.gov /models/cgm/cgm.html, for epoch 2007, assuming an altitude of 100 km. . 46

ABSTRACT

DEVELOPMENT OF GROUND-BASED SEARCH-COIL MAGNETOMETER SYSTEMS IN THE POLAR REGIONS AND STUDIES OF ULF Pc 1–2 WAVE PROPAGATION IN THE IONOSPHERIC WAVEGUIDE

by

Hyomin Kim

University of New Hampshire, May, 2010

Search-coil magnetometers, which measure time-varying magnetic flux density (dB/dt) and its direction, have been developed for the observations of geomagnetic pulsations in the ultra low frequency (ULF) range (a few mHz to a few Hz). The design, fabrication, and test/calibration have been performed to detect very weak geomagnetic pulsations with approximately a few pT resolution over the frequency range 0 – 2.5 Hz and 100 μsec timing accuracy, given a system gain of 4.43 V/(nT·Hz) and 12-bit analog-to-digital converter (ADC) with GPS time stamps. These instruments are deployed in the Polar regions forming high latitude networks and conjugate measurement points between the northern and the southern hemispheres. In addition to the development and installation of the magnetometers, this thesis describes analysis of the data from the magnetometer systems, mainly focusing on ULF wave propagation in the ionospheric waveguide (duct) centered around the electron density maximum near the F2 ionization peak. The Antarctic magnetometer array observes well-defined, band-limited ULF Pc 1–2 waves with poleward spectral power attenuation over a very extensive latitudinal coverage from geomagnetic latitudes of $-62°$ to $-87°$ (over the distance of 2920 km). This is a clear indication of the propagation of the electromagnetic ion cyclotron (EMIC) waves in the ionospheric waveguide. This study

focuses on the ducting events by comparing spectral power attenuation factors and polarization patterns. A statistical survey of the events reveals that the attenuation factors are between $\sim$ 10 to 14 dB/1000 km and the polarization sense changes as the waves are ducted poleward from the low latitude regions. For a detailed event study, a CHAMP satellite conjunction is presented. During the overflight, a transverse and linearly polarized Pc 1 ULF wave was also found over a limited latitudinal extent ($-53°$ to $-61°$ ILAT), which supports the idea that EMIC waves are injected at low latitudes and ducted in the ionosphere. The results show the observations of ducted waves over such an unprecedented latitudinal extent, which have rarely been measured before, and thus provide very important information about ionospheric wave ducting characteristics.

CHAPTER 1

INTRODUCTION

The Sun and the Earth are closely linked through a stream of charged particles ejected from the Sun called the *solar wind* and the Sun's magnetic field carried by the solar wind called the *interplanetary magnetic field (IMF)*. This connection is often called the Sun-Earth connection or the solar-terrestrial environment. The physics involved in the space environment has been of interest not only because its complex nature is intriguing but also because it impacts life on Earth in many ways especially during the space era. For example, a large-scale geomagnetic field perturbation (e.g., geomagnetic storm or substorm) can disrupt or damage technologically complex systems such as electric power and telecommunication systems as well as spacecrafts in orbit.

This thesis presents a system design of ground-based instruments which measure the geomagnetic field in the ultra low frequency (ULF) range, called *search-coil magnetometers*, and the study of ULF geomagnetic pulsations using the magnetometer array. Multiple sets of magnetometers have been constructed to form ground-based magnetometer arrays in the polar regions, which enable us to perform large-scale systematic observations of ULF wave propagation in the ionosphere.

Various types of waves are generated in space plasma by electron and ion dynamics associated with the geomagnetic field. They play an important role in accelerating radiation belt particles and transporting magnetospheric energy to the ionosphere. Some of the energy

of the magnetospheric waves is transmitted to the ionosphere and the waves propagate in the ionospheric waveguide. For this reason, the wave activity seen on the ground can be used to study the magnetosphere-ionosphere coupling dynamics, part of the Sun-Earth connection. This chapter briefly describes an introduction to waves in plasma and wave propagation in the ionospheric waveguide. Chapter 2 presents the design, construction, and test of the ULF search-coil magnetometers for the ground-based array. Chapter 3 and Chapter 4 show the analysis of the ULF magnetic field data obtained from the magnetometer array and discuss the ULF wave propagation in the ionospheric waveguide. Chapter 3 also presents a satellite observation of the ULF wave in the ionosphere. Finally, the conclusions are summarized in Chapter 5.

1.1 Solar-Terrestrial Environment

The electromagnetic connection between the Earth's magnetic field and the solar wind induces various kinds of large-scale currents and confines the Earth's magnetic field, forming a unique solar-terrestrial environment which includes the dipole-like structure of the Earth's magnetic field called the *magnetosphere*. The outer boundary, called the *magnetopause*, separates the Earth's magnetic field from the IMF. Figure 1-1 shows the Earth's magnetosphere and its current systems.

A variety of solar activities (a long-term or short-term variation of the solar wind and the IMF) affect the Earth's magnetosphere and its coupling to the ionosphere, which can be described by magnetohydrodynamics (MHD). The manifestations of these variations include geomagnetic storms, substorms, electromagnetic wave pulsations over a wide range of frequencies, electron and ion precipitation to the ionosphere from space, aurorae, and many more. Especially, geomagnetic storms and substorms disturb the Earths magnetic fields and cause acceleration/depletion of high energy charged particles in the radiation belts. These

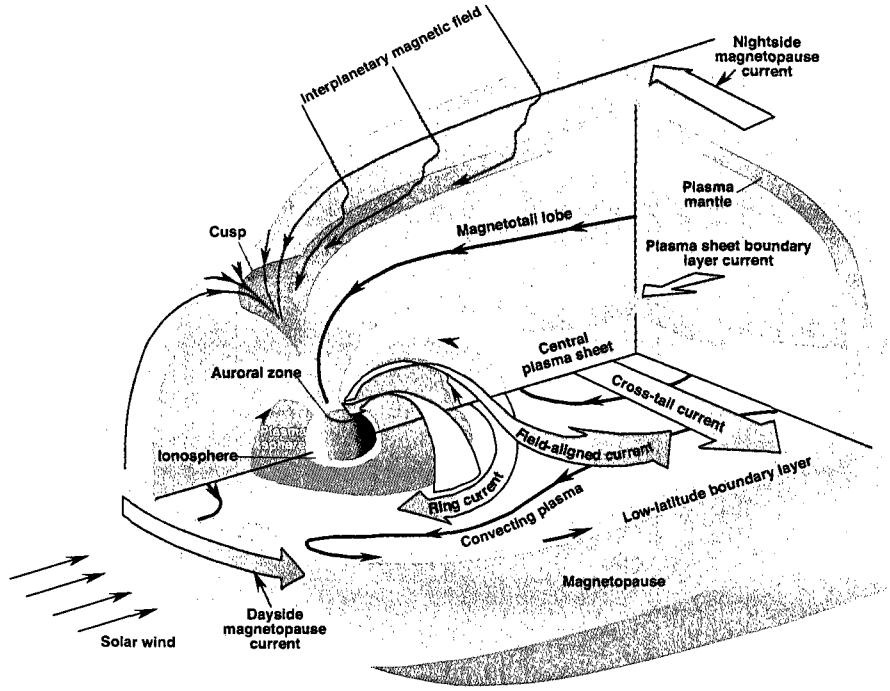

Figure 1-1: The Earth's magnetosphere and its current system (with permission from Anthony T.Y. Lui at JHU/APL).

phenomena can usually be detected by satellite-borne, rocket-borne, and ground-based instruments. Some of the typical, widely-used instruments are electric field antennas, imagers, particle detectors, and magnetometers.

The interaction between the ionosphere and magnetosphere characterizes the electrodynamic coupling affected by electric currents along the geomagnetic field lines, called *field-aligned currents* (FACs). The solar wind and outer magnetosphere act as a generator (i.e., by transferring mechanical energy to electromagnetic energy) and provide energy and momentum to the ionospheric load via FACs. The magnetosphere-ionosphere coupling process involves energy exchange between the two regions through plasma convection, Joule heating, auroral particle precipitation, ion outflow, and wave activities. The altered mag-

netospheric ion composition can have a significant effect on the magnetospheric dynamics. The waves in a space plasma transport magnetospheric energy to the ionosphere, determining the lifetime of trapped radiation, accelerating particles either stochastically or in resonance, and perhaps coupling solar wind energy to the magnetosphere.

1.2 System Engineering of Magnetometer Project for Space Research

The search-coil magnetometer is extremely sensitive and can detect time-varying magnetic fields (within the frequency response of the instrument) more than tens of thousands times weaker than the ambient magnetic field of the Earth. Ground-based observations of low-level magnetic field fluctuations provide important information about the magnetosphere and its coupling to the ionosphere. Coupling can occur in a variety of ways, encompassing a wide range of spatial scales and frequencies.

Single-point ground observations of the geomagnetic pulsations provide limited information about the wave source region since the ground-based magnetometer integrates signals over a horizontal extent of around 200 km (Baker et al. 1998) and the waves are predominantly observed from a region to which the source field line is mapped down. In addition, the existence of the ionospheric waveguide, in which the waves can propagate isotropically near the Alfvén speed, complicates the ground observations. An array of ground-based stations can provide spatially and temporally extended observations which can lead to a better understanding of wave propagation characteristics. If the ground stations are located over a large extent to form an array (especially along a magnetic meridian), time delays, determined by group velocity of the waves, and phase differences can be observed. Figure 1-2 is a simple sketch demonstrating the advantage of the "system" of ground-based magnetometers.

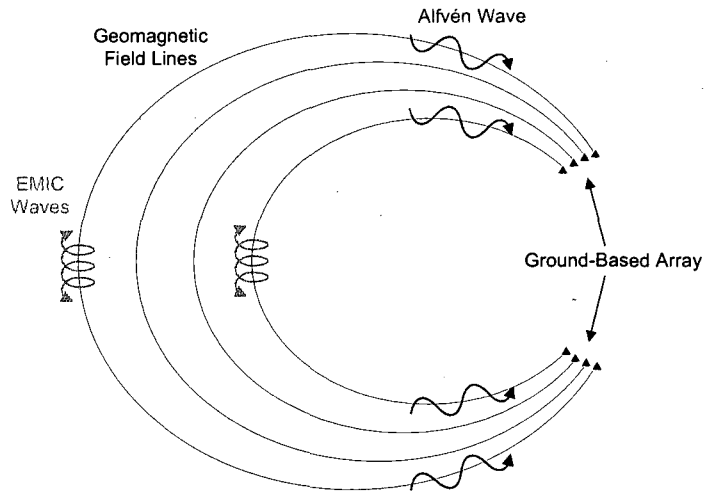

Figure 1-2: A sketch showing one use of the "system" of ground-based magnetometers, which provides spatially and temporally extended observations of the geomagnetic pulsations.

1.3 Waves in Space Plasma

1.3.1 Generation of Waves in Plasma

The collective behavior of magnetized plasma in space, combining mechanical forces due to gas-like properties of the plasma and electromagnetic forces due to charged particles, creates a unique type of waves in space, MHD waves, at low altitude where a cold magnetized plasma is found. They play an important role in transporting energy and accelerating plasma particles. Waves in plasma are typically generated by electron/ion cyclotron motion and plasma oscillation. The typical generation mechanisms of the waves in plasma are described briefly as follows.

Cyclotron (or Gyro) Motion The equation of motion for a particle of charge q and mass m under the Lorentz force (assuming $E = 0$ and $B = B_z$) can be represented as

$$m\frac{d\mathbf{v}}{dt} = q(\mathbf{v} \times \mathbf{B}) \tag{1.1}$$

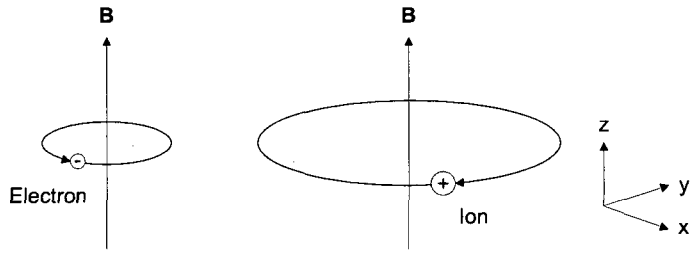

Figure 1-3: Charged particles gyrating around a guiding center in a uniform magnetic field.

which describes a simple harmonic motion at the *gyrofrequency* or *cyclotron frequency*, ω_g, which is represented as

$$\omega_g = \frac{|q|B}{m} \tag{1.2}$$

with the *gyroradius* (also called *Larmor radius*) defined as

$$r_g \equiv \frac{v_\perp}{\omega_g} = \frac{mv_\perp}{|q|B} \tag{1.3}$$

where $v_\perp$ is a velocity in the plane perpendicular to $\mathbf{B}$. The gyrating particle orbits around a center, called the *guiding center*, in a uniform magnetic field. The sense of rotation depends on the sign of the charge as shown in Figure 1-3. If the convention of the polarization sense is applied here, at ion cyclotron resonance, ω_{gi}, the macroscopic ion motion is circular and left-hand polarized and at electron cyclotron resonance, ω_{ge}, the macroscopic electron motion is circular and right-hand polarized. The direction of the gyrating particle motion is such that the magnetic field created by the gyration is opposite to the externally imposed field. Therefore, plasma particles reduce the ambient magnetic field and this behavior is called the *diamagnetic effect.*

Plasma Oscillation If the plasma is disturbed by external force (e.g., due to a charge or a density gradient), the plasma particles are accelerated in an attempt to restore

the charge neutrality. Due to their inertia the particles will move back and forth around the equilibrium position, resulting in fast collective oscillations. This oscillation is so fast that on the time scale of the oscillation the heavier ions do not have time to respond to the oscillation and may be considered as fixed. The frequency of the plasma oscillation is considered as a natural frequency of the plasma and can be represented as

$$\omega_p = \left(\frac{ne^2}{m\varepsilon_0}\right)^{1/2} \tag{1.4}$$

where n is particle number density (m^{-3}) and ε_0 is permittivity in free space.

1.3.2 Types of Plasma Waves

A variety of wave modes exist due to the complex interconnection between particles and fields, in which the waves propagate in an unmagnetized plasma or propagate parallel, perpendicular, or oblique to the ambient magnetic fields. When they are disturbed, waves in plasma oscillate around an equilibrium position because there are restoring forces involved in the oscillation. In an unmagnetized plasma, thermal pressure is the only restoring force, which leads to a wave mode called the *longitudinal, acoustic wave.* If a magnetic field is present in the plasma, the motion of charged particles is restricted. Particles can move freely along the magnetic field, but not perpendicular to the field due to the Lorentz force, $q(\mathbf{v}\times\mathbf{B})$, which causes the charged particles to gyrate about the magnetic field. Therefore, additional restoring forces, including magnetic pressure, $P_B(= B^2/2\mu_0)$ and the magnetic tension force, $\mathbf{M}_B(= (\mathbf{B}\cdot\nabla)\mathbf{B}/\mu_0)$, need to be considered. As a result, three MHD wave modes exist and, depending on how the waves propagate with respect to the ambient magnetic fields, are named pure (or oblique) *Alfvén waves*, *fast waves*, and *slow waves.* The Alfvén waves do not change the plasma and magnetic pressure or plasma density while the fast and slow waves cause changes of all of the plasma parameters, including the field-aligned

component of the magnetic field ($b_{||}$, which changes the field magnitude and the magnetic pressure. The magnetic field perturbation in the fast and slow waves lies in the plane of $\mathbf{B}$ and $\mathbf{k}$ (Kivelson & Russell 1995).

The MHD waves are described with the combination of Maxwell's equations (Faraday's law and Ampere's law) and Ohm's law ($\mathbf{E}+\mathbf{v}\times\mathbf{B}=0$), which also demonstrates the "*frozen-in flux*" condition. The concept of frozen-in flux is very important in understanding how the plasma is linked with the magnetic field lines. That is, in MHD fluid flow, the magnetic flux is frozen in to the fluid so that the fluid can move with the field lines (if the electrical conductivity of the fluid is large enough). Under the frozen-in flux condition, the total magnetic flux ($\Phi = \int \mathbf{B} \cdot d\mathbf{S}$) through a surface S remains constant even as the surface changes its location and shape over time. Schematic illustration of frozen-in flux is shown in Figure 1-4, in which an initial surface ($S(t_1)$) is changed to a surface at a later time ($S(t_2)$) due to plasma motion. The magnetic field is accordingly weakened or strengthened but the total magnetic flux through the surface remains unchanged. This can also cause the magnetic field line to bend to satisfy the frozen-in flux condition.

The Alfvén wave is purely transverse electromagnetic and can be represented as string-like low frequency (compared to the ion cyclotron frequency) oscillations of the magnetic field lines. The Alfvén wave propagates with the phase velocity,

$$\mathbf{v}_{ph} \equiv \frac{\omega}{k}\hat{\mathbf{k}} = v_A \cos\theta \tag{1.5}$$

where v_A is called the Alfvén velocity, which is represented as

$$v_A = \frac{B}{\sqrt{\mu_0 \rho}} \tag{1.6}$$

where μ_0 is permeability in free space and ρ is the total mass density of the charge plasma

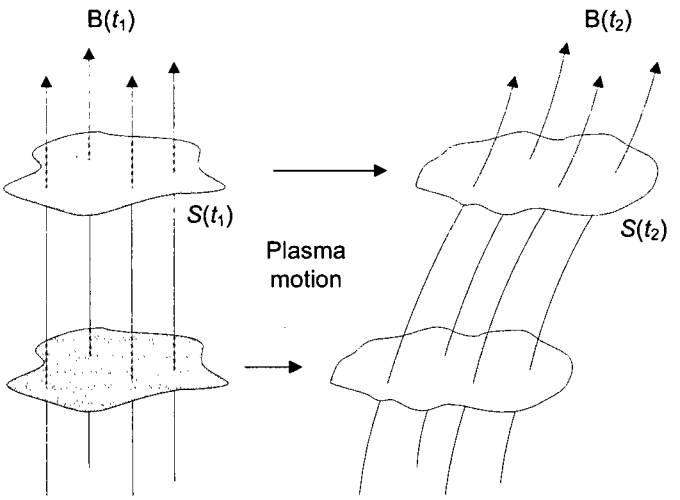

Figure 1-4: Schematic illustration of frozen-in flux. In MHD fluid flow, the magnetic flux is frozen in to the fluid so that the fluid can move with the field lines. Therefore, the total magnetic flux through surface remains unchanged.

particles. θ is the angle between $\mathbf{k}$ and $\mathbf{B}$. This means that the wave cannot propagate perpendicular to $\mathbf{B}$. Since the frequency of the Alfvén wave depends linearly on $\mathbf{k}_{\|}$, the Alfvén wave is non-dispersive. The group velocity of the Alfvén wave, $v_g = \partial\omega/\partial k$, at which wave energy (or wave packet) is carried, is parallel to the field lines ($\mathbf{v}_g = v_A\hat{\mathbf{B}}$) (Kivelson & Russell 1995).

The ion mass density provides the inertia and the tension force of the magnetic field line ($\mathbf{M}_B$) provides the restoring force. Therefore, the motion of the ions and the perturbation of the magnetic field are in the same direction and transverse to the direction of propagation of energy. The Alfvén wave is also called a shear Alfvén wave because there is no compression ($\mathbf{P}_B = 0$) of the plasma. The Alfvén wave is a major mechanism in accelerating charged particles in plasma. The Alfvén waves at low frequencies have a right-hand and a left-hand component, both of which are dominated by ion inertia. In general, Alfvén waves have an elliptical polarization, but they can become linearly polarized when the two oppositely

polarized modes have about equal amplitudes (Baumjohann & Treumann 1996).

The fast wave is a longitudinal wave of particles in a magnetized plasma, propagating in any direction and can transport energy in any direction ($\mathbf{v}_g = v_A\hat{\mathbf{k}}$). If the wave propagates in directions other than along $\mathbf{B}$ (i.e., if $\theta \neq 0$), the phase velocity (see Equation 1.5) is larger than v_A (Kivelson & Russell 1995). It is known that the Alfvén wave changes into the fast wave when the direction of propagation ($\mathbf{k}$) becomes close to perpendicular to the magnetic field. Since the fast mode wave can transport energy across magnetic field lines, magnetic pressure ($\mathbf{P}_B$) and the tension force ($\mathbf{M}_B$) are involved in the fast wave motion. The magnetic pressure fluctuates with the magnetic field in this wave mode. Thus the fast wave is also called a *compressional wave*. It is also known as *magnetosonic* or *magnetoacoustic* wave.

In the slow wave, total pressure (the sum of particle pressure and magnetic pressure) is approximately constant across $\mathbf{B}$ if $\mathbf{k} \parallel \mathbf{B}$ but not constant along $\mathbf{B}$. Its phase velocity is less than or equal to v_A, largest in the direction of $\mathbf{B}$ and the wave does not propagate perpendicular to $\mathbf{B}$ (Kivelson & Russell 1995). The magnetic tension force ($\mathbf{M}_B$) is not present. The slow wave is driven by field-aligned gradients of the total pressure and thus transports energy predominantly along the fields ($\mathbf{k} \parallel \mathbf{B}$). This wave mode is analogous to acoustic waves propagating along the field lines. The types of plasma waves are demonstrated in Figure 1-5.

Unlike the fast and slow mode waves, which change the pressure gradient, the Alfvén wave reduces only the bending of the magnetic field lines while plasma flow across the fields can increase the bending. The associated field perturbations create currents that reduce the additional curvature of the field lines. The currents are, in part, along the field lines so that the Alfvén wave induces the FACs, which play an important role in the magnetosphere-ionosphere coupling process (Kivelson & Russell 1995). Alfvén waves in association with

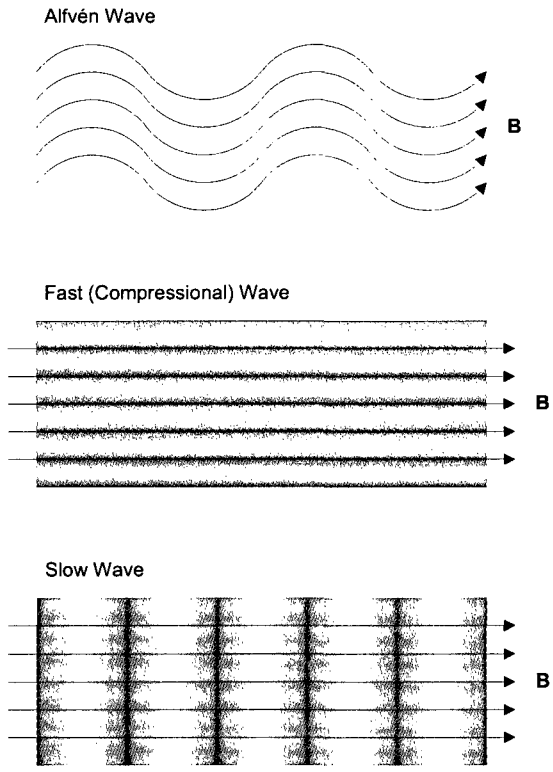

Figure 1-5: Types of waves in a magnetized plasma.

FACs have been observed by sounding rockets (e.g., Ivchenko et al. (1999)) and satellites (e.g., Gurnett et al. (1984), Chaston et al. (2002)).

1.3.3 Polarization of Waves

Polarization is a property of waves that describes the orientation of their oscillations. Depending on the direction of rotation of the field vector (electric field or magnetic field), polarization sense is defined: left-hand polarization (LHP), right-hand polarization (RHP), and linear polarization (LP). The wave polarization is one of the properties that provide the information about the wave and spatial characteristics of wave propagation and media. For example, it is known that electromagnetic ion cyclotron waves are LHP and the polarization changes during their propagation (e.g., due to the interaction with other waves or to

density gradients caused by heavy ions such as He^+ and O^+ (Horne & Thorne 1993)). For the geomagnetic pulsations observed on the ground, the polarization characteristics of the waves can provide information about the source region (Webster & Fraser 1985) and about the wave propagation from the source to the ground (Southwood & Hughes 1985). More detailed concepts and analysis techniques of polarization used in this thesis are described in Appendix A.

1.3.4 Geomagnetic Pulsations

Geomagnetic pulsations are short period (usually of the order of seconds or minutes) fluctuations of the Earth's magnetic field. The pulsation frequencies are lower than the natural frequencies of the plasma, such as the plasma frequency, ω_p, and the ion gyrofrequency, ω_{gi}. Such waves are referred to as ultra low frequency (ULF) waves. They are transitory variations with a small amplitude and leave no permanent effects on the field. Like longer period disturbances, such as magnetic storms, the energy that drives them is of solar origin, in contrast to the Earth's main field and secular variations which are of internal origin.

The notation and classification of ULF geomagnetic pulsations, which have been made based on early studies and observations, are given in Table 1.1 (see Jacobs et al. (1964)). The ULF pulsations were found to be grouped into two classes, continuous pulsations and irregular pulsations. The continuous pulsations are quasi-sinusoidal signals lasting more than several cycles and are broken into subclasses based on the wave period (T) or frequency (mHz), designating the subclass by a number (from Pc 1 to Pc 5). The Pc 1 and Pc 2 waves are typically associated with electromagnetic ion cyclotron (EMIC) waves. *Field line resonances* (FLRs), formed by standing Alfvén waves on the geomagnetic field lines, are usually observed in the Pc 5 range. The irregular pulsations are, on the other hand, broadband, short-lived signals, which contain spectral peaks at many different frequencies

Type		Period (sec)	Freq (mHz)
Continuous Pulsations	Pc 1	0.2 – 5	200 – 5000
	Pc 2	5 – 10	100 – 200
	Pc 3	10 – 45	22 – 100
	Pc 4	45 – 150	7 – 22
	Pc 5	150 – 600	2 – 7
Irregular Pulsations	Pi 1	1 – 40	25 – 1000
	Pi 2	40 – 150	7 – 25

Table 1.1: The classification of ULF geomagnetic pulsations (Jacobs et al. 1964).

(Pi 1 and Pi 2, based on the wave period or frequency) and are closely related to substorm activity.

The work done in this thesis is focused mostly on EMIC waves in the ULF Pc 1 (0.2 – 5.0 Hz) and Pc 2 (0.1 – 0.2 Hz) range (called Pc 1–2 hereinafter). EMIC waves are generally thought to be excited by the cyclotron instability of a hot, anisotropic ($T_\perp > T_\parallel$) distribution of medium energy ring current ions in the equatorial region of the magnetosphere in the energy range of ~1 – 100 keV during geomagnetic storms and substorms (Anderson et al. 1996, Kozyra et al. 1997, Jordanova et al. 2001, Thorne et al. 2006). Energy can be transferred from the particles to the waves when the particle gyrofrequency matches the Doppler shifted wave frequency. Because EMIC waves induce the cyclotron resonance of ring current particles, EMIC waves play an important role in causing rapid particle heating, pitch angle scattering and thus precipitation loss from radiation belts which are disturbed by geomagnetic storms or substorms. Measured EMIC wave amplitudes in space are typically in the range 0.1 – 10 nT.

A number of studies have reported observations of EMIC waves in the magnetosphere and the ionosphere. Simultaneous multipoint ground and satellite observations by Erlandson et al. (1996) estimated the latitudinal extent of the Pc 1 source at Viking's altitude from 63.7° to 64.7° invariant latitude (ILAT) ($L = 5.1$ to 5.5). The ST5 satellite observations of

Pc 1–2 waves by Engebretson et al. (2008) also showed a very narrow region of wave activity with a latitudinal extent of $\sim 0.5°$ to $1°$ in ILAT ($\sim$50 to 100 km). Anderson et al. (1992) reported the AMPTE/CCE satellite observations of Pc 1–2 waves in the equatorial magnetosphere over the range $L = 3$ to 9 and found that the waves were predominant at $L > 7$, concluding that plasma sheet ion distributions develop sufficient temperature anisotropy to generate EMIC waves on their open drift paths. The Polar satellite observations of Pc 1 waves in conjunction with ground observations (Mursula et al. 2001) reported that two EMIC wave bands (H^+ and He^+) are found around the plasmapause and the total Poynting flux of the He^+ band waves strongly directed downward away from the equator. The space-ground conjunction studies indicate that although the frequency response in space and the ground are similar, there are differences in both the spatial and temporal structures, suggesting that the wave structure is modified during propagation from the magnetosphere to the ionosphere.

EMIC waves are typically observed as Pc 1–2 type pulsations (e.g., as observed with search-coil magnetometers). It is generally accepted that left-hand polarized Alfvén EMIC waves propagate along the closed geomagnetic field lines from the magnetosphere to the ionosphere through field-aligned injection of the Alfvén wave and couple to right-hand polarized compressional (fast), isotropic waves in the ionospheric waveguide (Fraser 1975*a*,*b*, Fujita & Tamao 1988). It should be noted that EMIC wave polarization modes other than LHP (i.e., RHP or LP) can be found during propagation from the magnetosphere to the ionosphere (Young et al. 1981, Horne & Thorne 1993, Anderson et al. 1996, Denton et al. 1992). Horne & Thorne (1994) and Hu & Denton (2009) show that LHP EMIC waves generated near the equator become LP as they become oblique and propagate toward the ionosphere. Some of the energy of the field-guided signals is transmitted to the ionosphere near or in the auroral zone if the ionospheric conductance is matched to the Alfvén wave

impedance (see Lysak (2004)) and propagate in the ionospheric waveguide located around the F2 region in the ionosphere (see Section 1.4). Therefore, a signal observed on the ground may not be generated on the same field line as the incident Alfvén wave structure that generated it.

Although the solar induced wave energy in the Earth's magnetosphere is a small fraction of the energy present in the form of plasma and energetic particles (trapped radiation), waves are one of the most important components in the electrodynamics of the magnetosphere-ionosphere coupling. They play a role in transporting magnetospheric energy to the ionosphere; determining the life time of trapped radiation; accelerating particles either stochastically or in resonance; and, perhaps, even in coupling the solar wind energy itself to the magnetosphere.

1.4 Wave Propagation in the Ionospheric Waveguide

The ionosphere is the uppermost part of the atmosphere and consists of electrons and ions which are ionized by solar radiation, stretching from a height of about 50 km to 1000 km. The altitude range 150 – 500 km is termed the F region (O^+ dominant) and the altitude of maximum density there is termed the F peak. The F region consists of one layer at night while two layers, F1 and F2, appears during the day. The altitude range 90 – 150 km is called the E region and the ionization below 90 km is called the D region. NO^+ and O_2^+ become more dominant in the D and E regions (Kelley 1989). Typical profiles of neutral atmospheric temperature and ionospheric electron density are shown in Figure 1-6.

The ionospheric waveguide (or duct) is formed around the ionospheric F2 region altitude of the electron density maximum (or the Alfvén speed minimum since the electron density and Alfvén velocity profiles are almost mirror images near this region) at an altitude of ~400 km, bounded by the E region (~100 km) and a region where the Alfvén speed

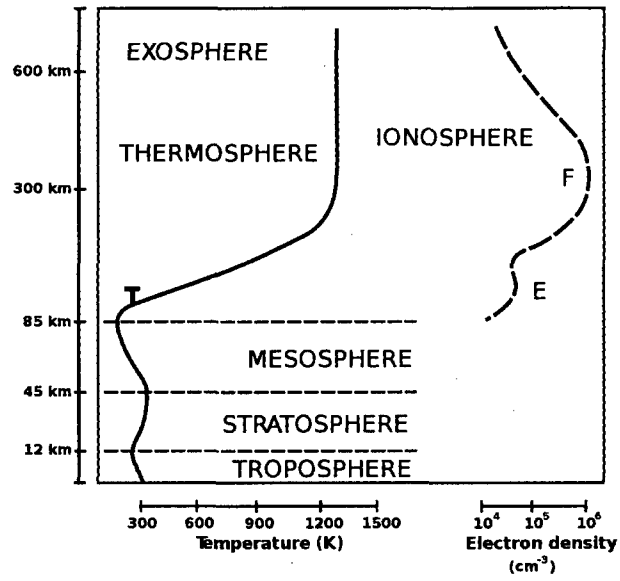

Figure 1-6: Profiles of neutral atmospheric temperature and ionospheric electron density with the various layers designated (Courtesy of Bhamer, from Wikipedia public domain).

increases sharply (~1000 km) (Tepley & Landshoff 1966, Manchester 1966, Greifinger & Greifinger 1968). The density structure forms a resonance cavity for Alfvén waves in the ionosphere and thus provides a waveguide for compressional waves that propagate across field lines (Greifinger & Greifinger 1968). The field line guided waves in the LHP (or LP) Alfvén mode are injected in the ionosphere and coupled to the RHP compressional isotropic waves, propagating horizontally in the waveguide (Fraser 1975*a*, Altman & Fijalkow 1980, Fujita & Tamao 1988). The mode conversion is caused by anisotropic Hall currents (e.g., Fujita & Tamao (1988)). ULF Pc 1–2 waves (especially, Pc 1 pearls) are one of the most efficiently propagated MHD waves in the waveguide. Figure 1-7 sketches the concept of the propagation of EMIC waves from the equatorial region in the magnetosphere to the ionospheric waveguide.

Since the waveguide boundaries are not perfect reflectors, waves attenuate during propagation in the waveguide. Moreover, the attenuation does not always occur in a consistent

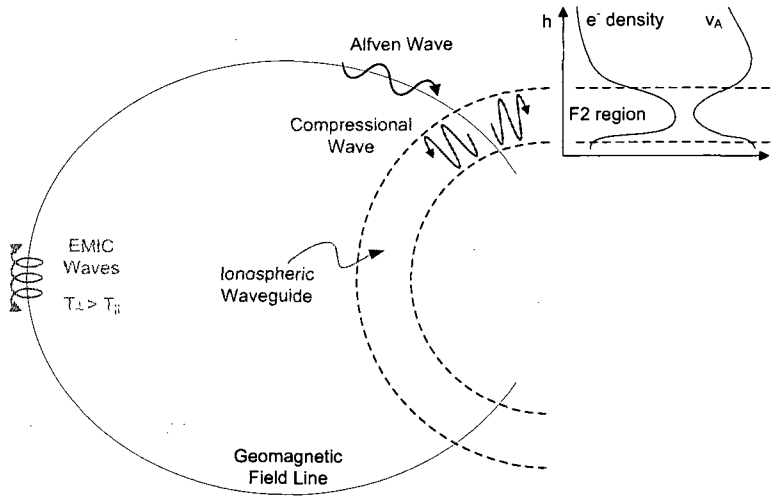

Figure 1-7: Conceptual sketch of the propagation of EMIC waves from the equatorial region in the magnetosphere to the ionospheric waveguide.

and linear fashion probably due to a leaky waveguide (Neudegg et al. 2000, Manchester 1968). In addition, the ionospheric inhomogeneity and superposition effects of ducted waves during propagation cause changes in polarization (e.g., change of polarization sense and polarization ellipse major axis angle).

Waves are identified as ducted in the ionospheric waveguide when identical spectral structures with wave power attenuation are observed from multi-point ground magnetometers located over a large extent. In other cases, some waves could be detected simultaneously by the spatially separated instruments, showing similar (but not identical) spectral structures. These waves might be generated from different L-shells in the magnetic field lines, causing similar spectral patterns over a distance. This is what needs to be distinguished from the ducted waves. In addition, one might argue that the waves with identical spectral pattern seen on the ground, being attenuated over a large extent, may not be ducted waves in the ionosphere but instead waves originating from a localized region and spreading out to a large extent in the form of an electromagnetic wave in free space. If this were

a valid scenario, the waves would not be able to be detected beyond the horizontal range that a typical ground magnetometer can cover (the spatial measurement range of a typical ground magnetometer is approximately 200 km as mentioned earlier (Baker et al. 1998)). Moreover, according to the far-field approximation in electromagnetics, the phase variation across the sensors is not observed or negligible if the wavelength is much larger than the distance between the sensors (in the case of Pc 1–2 waves, the wavelength is estimated to be much larger than the array spacing). However, the observations of the ducted waves do show phase delays, supporting the concept of wave propagation in the waveguide.

In this thesis, simultaneous observations of ULF Pc 1–2 waves are discussed using a a ground-based search-coil magnetometer array, spanning ~2920 km geographically, of which the coverage is much larger than the detectable range of a single search-coil magnetometer. By means of multipoint ground observations, the ducting effects of ULF Pc 1–2 waves are clearly observed.

CHAPTER 2

DEVELOPMENT OF SEARCH-COIL MAGNETOMETERS

2.1 Introduction

The search-coil magnetometer is widely used for space science research to measure low frequency magnetic field fluctuations and waves in space and on the ground. The magnetic field frequencies of interest in space physics typically falls into the ultra low frequency (ULF) range (a few mHz to a few Hz, as typically defined in space physics), which can be detected by a search-coil magnetometer. This type of magnetometer is very useful in space science research in that many phenomena in space plasma (e.g., plasma waves, ion cyclotron waves, etc.) are found in the ULF range.

A search-coil magnetic sensor is copper wire wound around a core of high permeability (μ) to draw a voltage across the coil when magnetic field through the search-coil changes over time. One of the major benefits of a search-coil magnetometer is that it can resolve changes in magnetic fields very quickly over a wide range of frequencies, up to a few MHz. Unlike fluxgate magnetometers, which measure ambient magnetic field intensity (B), responding only to low frequency magnetic field variations (suitable up to a few tens of Hz), search-coil magnetometers detect time-varying magnetic fields (dB/dt) with typically higher signal

resolution and sensitivity. The resolution and sensitivity can be improved relatively easily by increasing the number of turns of the wire, physical size of the core, or gain of amplifying electronics.

Since a search-coil magnetometer is sensitive to the magnetic field direction, it provides vector magnetic field information. Two or three orthogonally mounted search-coil magnetic sensors are used for the measurement of field direction. A search-coil magnetometer is especially suitable for space-borne instrumentation and unmanned ground-based configuration because of its low power consumption (~tens of mW), simple structure, and reliability. It is also relatively easy to build using mostly off-the-shelf components and materials.

2.2 Principle of Operation

A search-coil magnetometer is the simplest type of magnetic field sensor which measures magnetic field intensity and direction. The principle of operation is based on Faraday's Law of induction:

$$V_o = \oint \mathbf{E} \cdot d\mathbf{l} = -\frac{d}{dt} \int_A \mathbf{B} \cdot d\mathbf{A} = -n\frac{d\Phi_c}{dt} \tag{2.1}$$

The voltage (V_o) induced in turns of a coil (solenoid) is proportional to the number of turns of coil (n) and the time rate of change of flux (Φ_c) linked with the coil. Figure 2-1 describes the concept of the search-coil magnetometer. For more efficient induced voltage output from the coil (i.e., to increase flux density), a high permeability (μ) ferromagnetic core is typically used. The main advantage of using a high permeability core is the increase in sensitivity at a given sensor weight or the significant reduction in size and weight for a given sensitivity. If the coil is wrapped tightly around a long and thin core, reducing the coil's radial dimensions and thus the length of wire used, lower internal noise and higher sensor

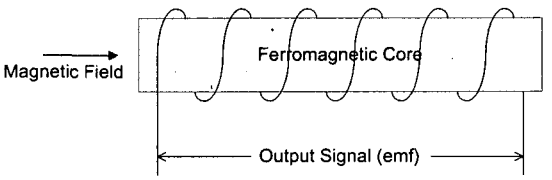

Figure 2-1: Schematic of search-coil magnetometer showing principle of operation based on Faraday's Law of induction. When the magnetic flux density through the coil changes, a voltage (emf) is induced in the coil.

bandwidth are expected (Boll & Overshott 1989). A search-coil magnetometer employs very simple electronics, which mostly consists of amplifiers and band-pass filters.

The sensitivity of the search-coil magnetometer depends on the permeability of the core material, the area of the coil (cross-sectional area where magnetic flux intersects), the number of turns of coil, and the rate of change of the magnetic flux through the coil. The sensitivity S_o of the coil is defined as

$$S_o = \frac{V_o}{fH} \ [\mathrm{V/(nT \cdot Hz)}] \tag{2.2}$$

where V_o is the open-loop peak output voltage of the coil, f is frequency, and H is magnetic field intensity. Assuming a sinusoidal magnetic flux variation,

$$\Phi_c = \Phi_{max} \cos(\omega t) \tag{2.3}$$

the open-loop peak output voltage of the coil is then obtained from the Equation (2.1),

$$V_o = \omega n \Phi_{max} = \omega n \mu_r \mu_0 H_i A_c \tag{2.4}$$

where μ_r is relative permeability, μ_0 permeability of vacuum, H_i magnetic field intensity inside the core, and A_c is the area of the coil. Using the relation, $\mu_r H_i = \mu_c H$ and the

cross-sectional area of the core $A_c = \pi D_c^2/4$ (D is the core diameter), the sensor output voltage can now be rewritten as

$$V_o = \frac{\pi^2}{2} n \mu_c \mu_0 D_c^2 f H \tag{2.5}$$

Therefore, the sensitivity defined in Equation (2.2) is then

$$S_o = 2\pi n A_c \mu_c \mu_0 = \frac{\pi^2}{2} n D_c^2 \mu_c \mu_0 \ [\mathrm{V/(nT \cdot Hz)}] \tag{2.6}$$

(Boll & Overshott 1989). The sensitivity of the search-coil magnetic sensor in this study is estimated by Equation 2.6 as shown in Section 2.3.4.

2.3 Technical Details of the UNH ULF Search-Coil Magnetometer

A search-coil magnetometer consists of two (or three) orthogonally mounted magnetic sensors, analog electronics, and data acquisition electronics. Figure 2-2 and Figure 2-3 show a schematic diagram and a picture of a search-coil magnetometer system developed at the University of New Hampshire, respectively. Signals detected by the search-coil magnetic sensors are filtered and amplified by the analog circuit, and digitized and archived in the data acquisition system. A preamp is equipped in each magnetic sensor so the signals are amplified to a suitable level before being transmitted to the main analog electronics through a long cable (typically, approximately 200 m). The main analog electronics, including amplifiers and band-pass filters, are installed with the data acquisition electronics. The data acquisition electronics employs a multi channel analog-to-digital converter (ADC) and a microcontroller for data acquisition, storage (into a Compact Flash memory card or a Compact Disc) and system user interface. A GPS antenna/receiver is used to synchronize the

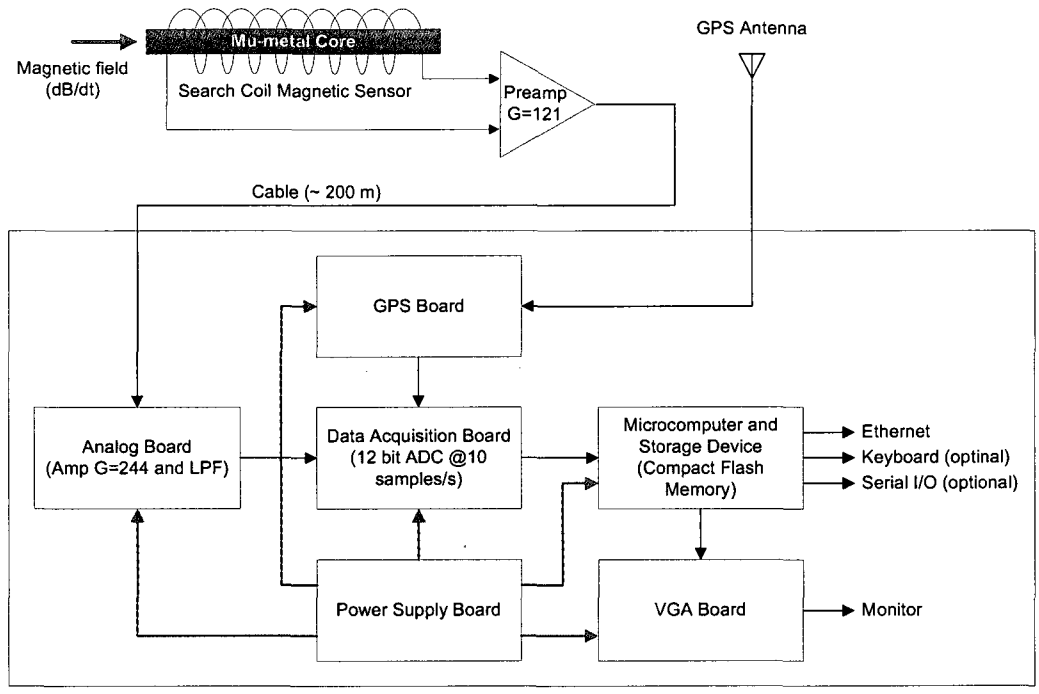

Figure 2-2: Schematic diagram of the UNH ULF search-coil magnetometer system.

data acquisition process for time reference with 100 μsec accuracy.

2.3.1 Search-Coil Magnetic Sensor

The search-coils that are used for this project have 160,000 turn coils of enamel-coated copper wire (AWG 36) wound around a 80 cm long $\times$ 2.54 cm diameter annealed μ-metal core. There are 16 individual wire spools, each of which has 10,000 turn coil. A test coil (of 10 turns) is placed on one of the spools (the one closest to the preamp), which is directly connected to the main analog electronics through the cable. A test signal (1 Hz square wave) from the main analog electronics excites the magnetic sensor through the test coil so that connectivity of the entire system can be checked. The spool coil winding, interconnection between the spools, and schematic diagram of the magnetic sensor are shown in Appendix B.1. The technical information for the core material used is as follows: Descrip-

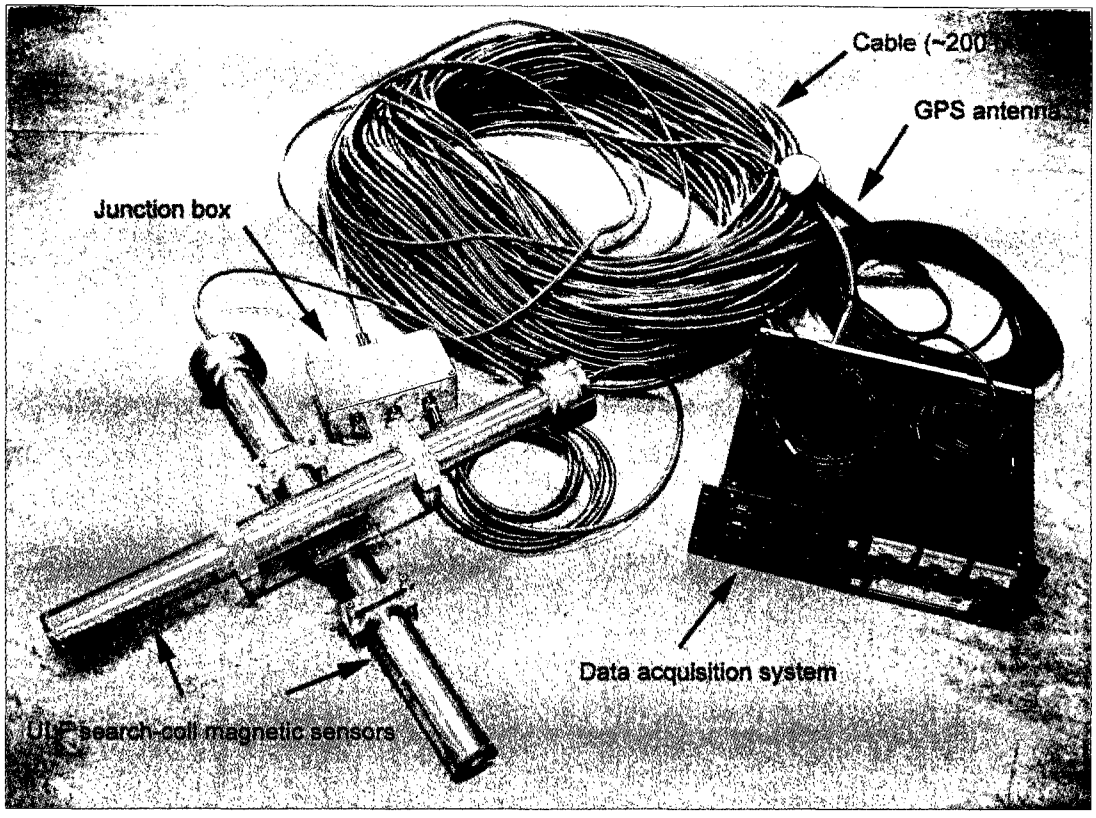

Figure 2-3: UNH ULF search-coil magnetometer system.

tion: MuShield magnetic shielding 2.54 cm diameter barstock (heat treated); Specification: MIL N 14411C COMP1, ASTM A 753 ALLOY 4 DC; Magnetic Properties: μ @40 G = 44250; μ @100 G = 51500; μ @2500 G = 183400; μ_{max} = 223668; H_c = 0.007.

Two identical magnetic sensors are mounted orthogonally to measure geomagnetic north-south and east-west wave activity. This setup identifies the polarization characteristics of magnetic field waves. In some cases, a third sensor is installed vertically to detect magnetic activity along the geomagnetic field line. The low-noise preamp, powered from the data acquisition electronics through the cable, is equipped in each magnetic sensor (Figure 2-4). The gain of the preamp is 121. An electrical schematic of the preamp is shown in Appendix B.2. The core and the wire spools are housed in a polycarbonate tube (82 cm

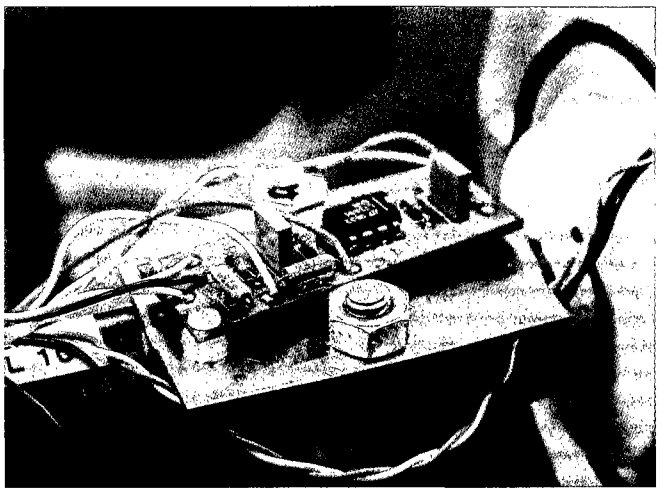

Figure 2-4: Preamp board of the UNH ULF search-coil magnetic sensor.

long × 6 cm diameter), on which a connector is attached (See Figure 2-5). The weight of one axis of the sensor is approximately 8 kg. All the materials used for the magnetic sensors are chosen to be non-magnetic to avoid any possible interference during measurement. A thin copper sheet is wrapped around the sensor housing in order to reduce external noise. Both sides of the sheet do not touch each other to avoid eddy current around the sheet although the eddy current might be negligible in the low frequency range (Figure 2-5 shows the sensor before the copper sheet is wrapped. See Figure 2-3 for completed sensor construction). More electrical specification along with the entire system specification is described in Section 2.3.4.

2.3.2 Main Analog Electronics

The main analog electronics provide input signal conditioning (band-pass filtering and amplifying) for three channels of analog input signals from the preamp in the search-coil magnetic sensors. The main analog electronics consists of a two-stage first-order passive low-pass filter and a two-stage first-order active low-pass filter, of which the total gain is 244. The passive filters employ RC type filters. Low-noise op-amps are used for the active

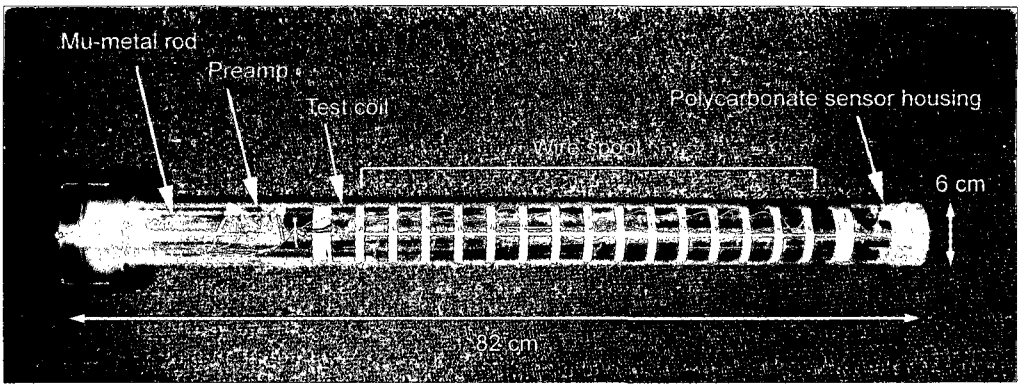

Figure 2-5: UNH ULF magnetic sensor with annotations.

filters. The high-pass filter RC constant is about 100 sec and therefore, a slow response of DC offset signal output to signal input is expected. Figure 2-6 shows the main analog electronics on PC104 (an embedded computer standard) PCB. An electrical schematic of the main analog electronics is shown in Appendix B.3.

2.3.3 Data Acquisition System

The data acquisition system digitizes the signals in three channels (signals from X, Y, and Z axis; currently, Z axis is not used) from the main analog electronics with a sampling rate of 10 Hz and saves the acquired data in its built-in Compact Flash memory. Optionally, the data can be archived in Compact Discs. Data sampling is synchronized to 1 pulse per second (PPS) GPS signal from a GPS antenna to provide time information to within 100 μsec accuracy. Data file length can be configurable from 1 second to 24 hours. Currently, the data acquisition system creates a data file that contains 24 hours worth of data. In the data acquisition system, there are five PC104 modules (see Figure 2-7) as well as the main analog circuit board as described below.

(1) Eagle PC104-30G Acquisition Board: 16 channel, $\pm$10 V differential analog input 12 bit ADC with an array of configurable input/output (I/O) and counters and timers.

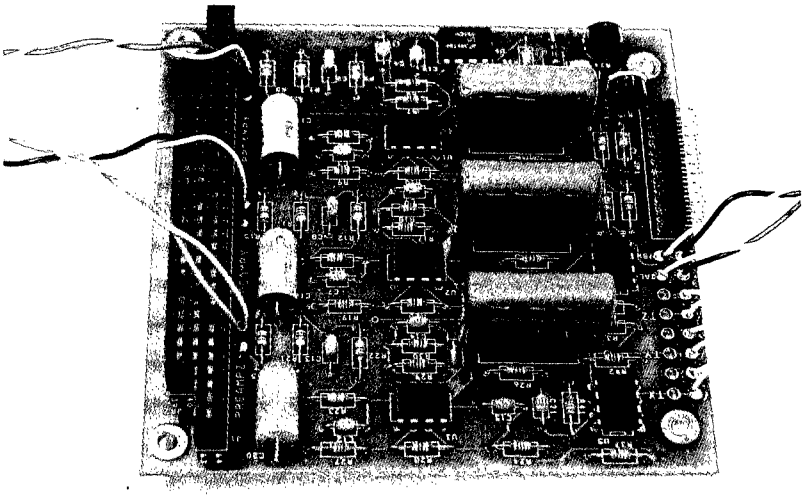

Figure 2-6: UNH ULF search-coil magnetometer main analog electronics.

(2) WinSystems PCM-SC520 PC104 Computer Board: includes an AMD x86 based processor, configurable volatile system memory, 4 serial ports, an IDE interface and a Compact Flash card which provides data storage as well as system boot information and acquisition software.

(3) RTD GPSHR 140 PC104 GPS Receiver: contains the NAVMAN GPS receiver module to provide GPS location and time information.

(4) VGA graphic card module: provides VGA display when connected to an external monitor.

(5) PC104 Power Supply: provides ± 12 VDC and $+5$ VDC.

2.3.4 System Specification

The technical details of the UNH ULF search-coil magnetometer system are specified below and a magnetometer system connection diagram is shown in Appendix B.4.

Type of instrument: 2-axis search-coil magnetometer

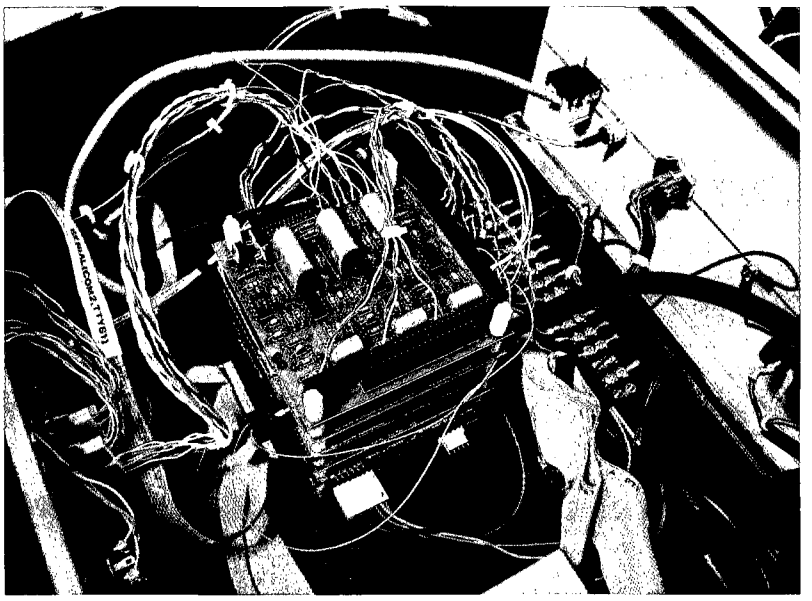

Figure 2-7: PC104 module stack in the data acquisition system enclosure. The module consists of analog-to-digital converter (ADC), Microcontroller, GPS receiver, VGA graphic card, power supply board, and main analog electronics.

Operating voltage: ± 12 VDC (analog), $+5$ VDC (digital)

Power consumption: 10 mA (5 mA + 5 mA, preamp), 36.8 mA (18.4 mA + 18.4 mA, main analog electronics)

Gain: preamp=121, main electronics=244

Magnetic sensor sensitivity: 150 μV/(nT $\cdot$ Hz)

System sensitivity: 4.43 V/(nT $\cdot$ Hz)

Frequency response: 0 – 2.5 Hz (-3 dB corner frequency, DC is not measured)

System resolution: $\sim$10 pT/$\sqrt{\text{Hz}}$ over the frequency response

Dynamic range: ± 2.26 nT over the frequency response

Analog input voltage range: ± 10 V

Signal input channels: 3 (X, Y, and Z), differential

ADC bit resolution: 1 pT $\cdot$ Hz (12 bits)

ADC sampling rate: 10 samples/sec

GPS timing: data sampling synchronized to GPS 1 PPS within 100 μsec accuracy

File storage: Compact Flash memory (128 MB to 4 GB+)

File length: configurable from 1 second to 24 hours

File storage format: binary with ASCII NMEA 0183 heading

File size: 10 samples/sec/ch $\times$ 3ch $\times$ 2 byte/sec $\times$ 1 hour = 216 kB

The coil gain (sensitivity) of the search-coil used for this study is 150 $\mu\mathrm{V}/(\mathrm{nT}\cdot\mathrm{Hz})$. Preamplifiers (gain = 121) at the coils provide mV signal levels for transmission to the main analog electronics (gain = 244). Therefore, the overall system provides the gain,

$$G_s = 150\mu\mathrm{V}/(\mathrm{nT}\cdot\mathrm{Hz}) \times 121 \times 244 = 4.43\mathrm{V}/(\mathrm{nT}\cdot\mathrm{Hz})$$

Bit resolution of this system associated with analog-to-digital conversion can then be estimated with an ADC analog input range and the system gain specified. The data acquisition system used in this study employs a 12 bit ADC with $\pm$10 V analog input range; the system resolution is

$$\text{System signal resolution} = 20\ \mathrm{V}/\mathrm{G_s} = 4.51\ \mathrm{nT}\cdot\mathrm{Hz}$$

and the bit resolution is

$$\text{Bit resolution} = \text{System signal resolution}/2^{12} = \sim 1\ \mathrm{pT}\cdot\mathrm{Hz}$$

2.4 Tests

2.4.1 Polarity Test

The polarity test is performed once the magnetic sensors are built to confirm that the sensors correctly measure increase/decrease of magnetic flux. Correct polarity is critical to identify wave polarization. For this project, a magnetic perturbation along the sensor axis in the direction toward the sensor connector is defined as a "positive" signal as shown in Figure 2-8a (See Section 2.5 for more detail). A test signal as shown in Figure 2-8b is applied to see if an output signal appears as displayed in Figure 2-8c. A search-coil magnetometer detects only a time-varying magnetic field (dB/dt), and therefore a positive output voltage will be induced when a test signal voltage increases (when $dB/dt > 0$). Output signal will be zero when there is no magnetic field change in time (when $dB/dt = 0$). A negative signal from the output will be measured when a test signal voltage decreases (when $dB/dt < 0$). A test signal for polarity test as shown in Figure 2-8b can easily be created by a simple RC circuit and a test solenoid (Figure 2-9).

The main analog electronics has a built-in test signal generator. The test signal generator is connected to the test coil in the search-coil magnetic sensor. The principle of operation is identical to the test RC circuit described above. A test signal can be generated by pushing a button located on the front panel of the data acquisition system. This test method is very useful for a system integrity check after the system is deployed for operation. The main analog electronics generates a square wave test signal and the system responds to the rising and falling transition of the square wave signal as shown in Figure 2-10.

2.4.2 Frequency Response Test

The frequency response test characterizes how the magnetometer system responds to magnetic fields over a specified range of frequencies by measuring output signals in response

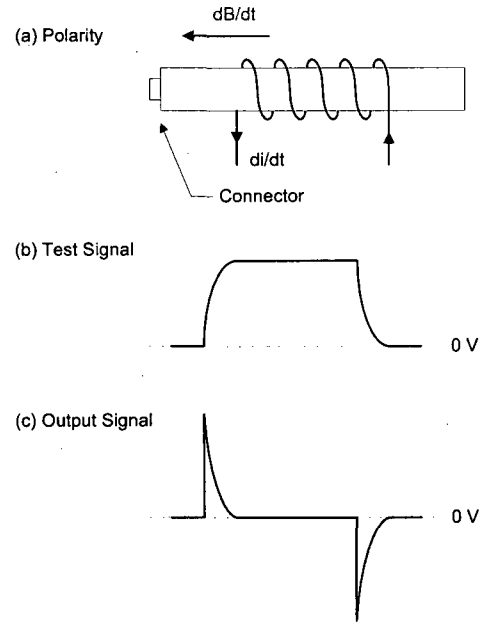

Figure 2-8: (a) Definition of signal polarity of the UNH ULF search-coil magnetic sensor; (b) test signal for sensor coil polarity test; (c) magnetometer output signal in response to the test signal.

to input signals. As shown in Figure 2-11, a test solenoid is used to generate a known input signal (time-varying magnetic field) around the magnetic sensor and the corresponding output signal from the magnetometer can be measured.

The test solenoid has 872 turns of wire wound around a PVC pipe of dimension large enough to provide uniform magnetic fields around the one-axis search-coil magnetic sensor under test (see Figure 2-12). This test is performed in the field where minimal electromagnetic interference (EMI) is expected although there is no information obtained as to what the level of EMI is during the test. Ideally, a calibration room which provides EMI shielding around the sensor is desired but no such facility is available at the University of New Hampshire. However, one can expect that the frequency response of the system can be obtained as long as an input signal is well-defined and generated without significant disturbance by

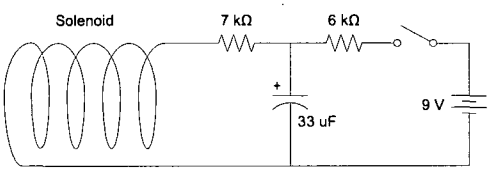

Figure 2-9: A solenoid and an RC circuit for polarity test. This device is used externally near the search-coil magnetic sensor to test the sensor polarity.

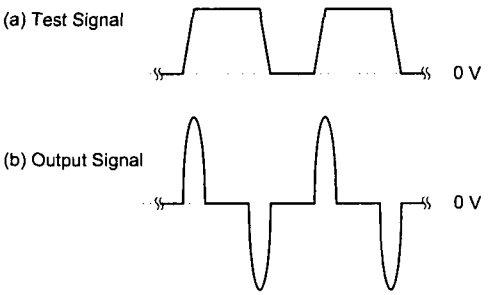

Figure 2-10: (a) Square wave test signal generated by the main analog electronics of the UNH ULF search-coil magnetometer system; (b) output signal in response to the rising and falling transition of the test signal.

EMI (observed from test equipment such as an oscilloscope). The search-coil sensors and the test solenoids are placed about 200 m away from the magnetometer electronics and the test equipments to isolate them from being disturbed electromagnetically. The test solenoid is approximately 50% longer in length and 100% larger in diameter. Since the magnetic field inside a solenoid is defined as

$$B = \mu_0 nI = \mu_0 nV/R \tag{2.7}$$

the coil constant of the solenoid (B/I) is 1.10 $\times 10^{-3}$ T/A ($= \mu_0 n$ where $\mu_0 = 4\pi \times 10^{-7}$H/m, $n = 872$). Therefore, with a known voltage across the resistor, R, (5 MΩ for this test) connected in series with the test solenoid, the magnetic field inside the test solenoid can be estimated when a signal is applied to the test solenoid by a function generator. The

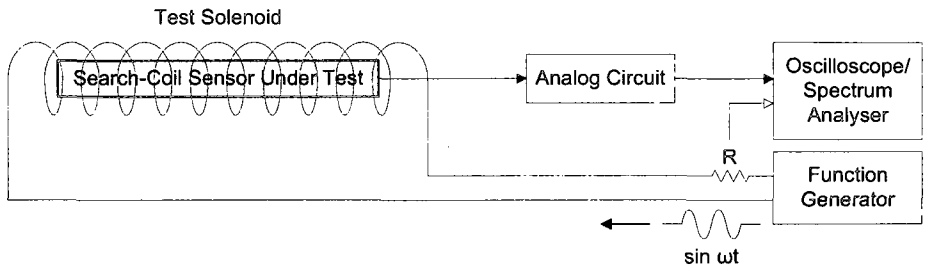

Figure 2-11: Test setup for frequency response and resolution characterization of the search-coil magnetometer system.

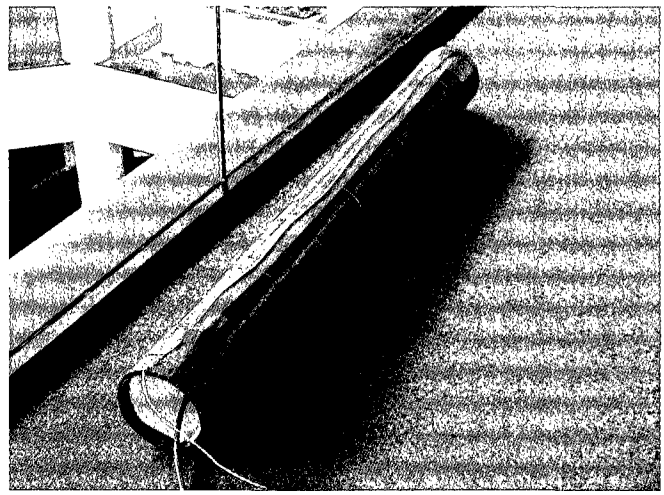

Figure 2-12: Test solenoid used for frequency response and resolution tests.

amplitudes of the output signals from the main analog electronics (the signals before they are digitized) are measured when a magnetic field intensity of 1.3 nT in the solenoid is created by a peak-to-peak voltage of 6 V_{p-p} across the resistor R, as shown in Figure 2-11, over the sweep frequency (0.1 – 30 Hz).

Bode plots of frequency response test results of the sensor and the overall magnetometer system in dB scale versus frequency are shown in Figure 2-13 and 2-14, respectively. A search-coil magnetometer measures time-varying magnetic fields only (dB/dt) and does not detect a DC magnetic field (when $f = 0$). The top panels of Figure 2-13 and 2-

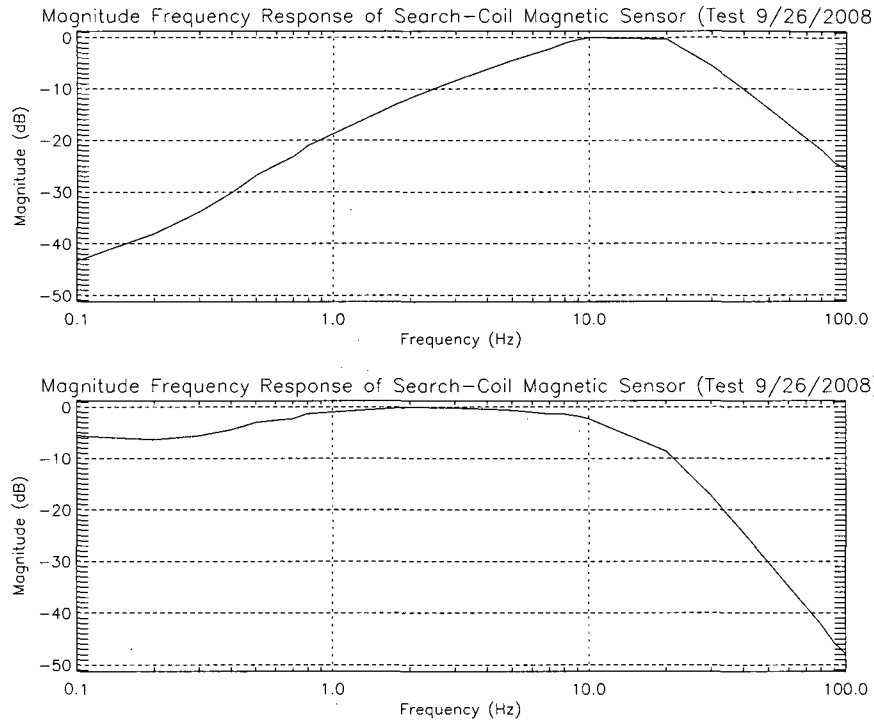

Figure 2-13: Bode plots of frequency response to the voltage output (top) and to the magnetic field (bottom) of the UNH ULF search-coil magnetic sensor (with preamp), showing that the frequency response is 0 – 10 Hz (specified at −3 dB corner frequencies). Note that DC magnetic field (when $f = 0$) is not detected by a search-coil magnetic sensor.

14 show the frequency response of the voltage outputs from the sensor and the overall magnetometer system, respectively. For a different type of representation of frequency response, the measured voltages from the magnetometer are divided by ω to show a plot of magnetic field (B) versus frequency (the bottom panels of Figure 2-13 and Figure 2-14) since the search-coil magnetometer measures $dB/dt = \omega B_0 \cos \omega t = \omega B$ assuming that the magnetic field can be represented as a sinusoidal signal, $B = B_0 \sin \omega t$. The result demonstrates that the frequency response of the search-coil magnetic sensor (with preamp) and the magnetometer system is 0 – 10 Hz and 0 – 2.5 Hz, respectively, at −3 dB corner frequencies. Frequency response characterization of each component of the magnetometer system using equivalent circuit models is described in Appendix B.5.

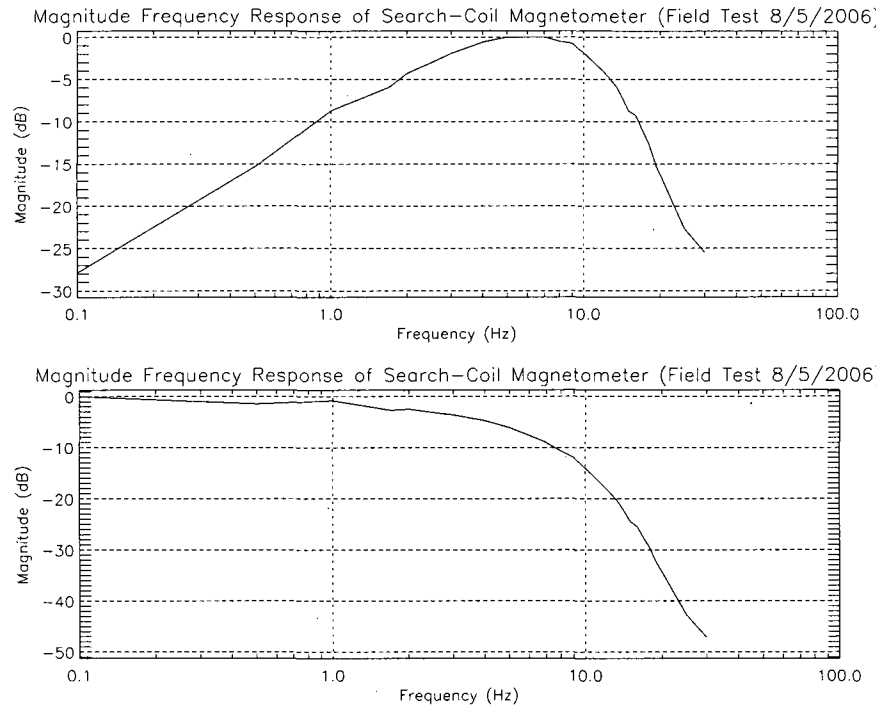

Figure 2-14: Bode plots of frequency response to the voltage output (top) and to the magnetic field (bottom) of the UNH ULF search-coil magnetometer system, showing that the frequency response is 0 - 2.5 Hz (specified at -3 dB corner frequencies). Note that DC magnetic field (when $f = 0$) is not detected by a search-coil magnetometer.

2.4.3 Resolution Test

The resolution of a magnetometer represents the smallest change in magnetic field it can detect. The test setup is identical to the one for the frequency response test except for the use of a spectrum analyzer to measure signals in the frequency domain in replacement of an oscilloscope. Instead of applying a signal with a fixed voltage and a frequency being swept to the test solenoid as conducted in the frequency response test, the resolution test is performed by adjusting the input voltage level (equivalently, the magnetic field inside the test solenoid) and observing a minimum discernable signal (MDS) from the magnetometer output at a fixed frequency. In this test, the MDS is defined as a spectral peak shown in 3 dB above the noise floor in response to an external magnetic field given by the test solenoid

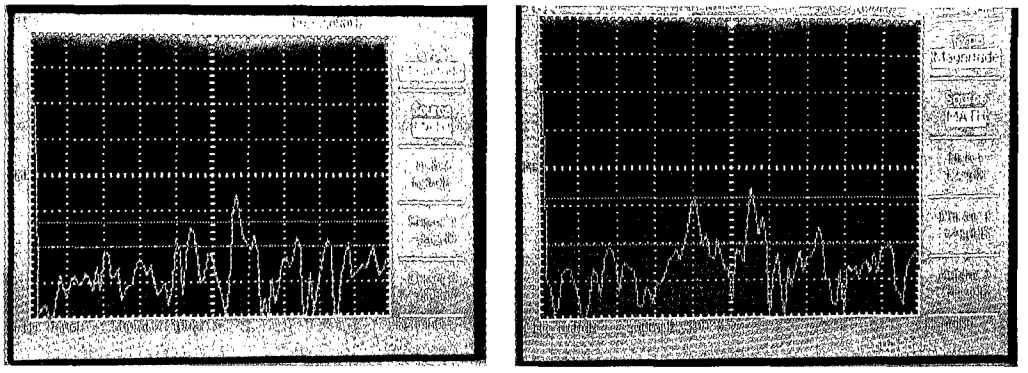

Figure 2-15: Screenshot of spectrum analyzer showing the search-coil magnetometer response to a 1 Hz (left) and a 2 Hz (right) test signal when the peak is 3.0 dB above the noise floor. This peak intensity corresponds to 8.8 pT and 5.5 pT, respectively.

at selected frequencies. In practice, the spectral peak seen in the output signal spectrum is read when the peak is 3 dB above the noise floor in the spectrum. The resolution of the magnetometer system is the magnetic field in the test solenoid when the MDS is observed. The magnetic field can be easily estimated using Equation (2.7) where V is the voltage across the resistor, R (10 MΩ for this test) as shown in Figure 2-11. Figure 2-15 shows the screenshots of the spectrum analyzer when it reads the resolution of 8.8 pT at 1 Hz and 5.5 pT at 2 Hz. The following is the summary of the resolution test result at selected frequencies.

Resolution = 8.8 pT/$\sqrt{\text{Hz}}$ @0.5 Hz (V_{in} = 80 mV)

Resolution = 8.8 pT/$\sqrt{\text{Hz}}$ @1 Hz (V_{in} = 80 mV)

Resolution = 5.5 pT/$\sqrt{\text{Hz}}$ @2 Hz (V_{in} = 50 mV)

Resolution = 8.8 pT/$\sqrt{\text{Hz}}$ @4 Hz (V_{in} = 80 mV)

Resolution = 11 pT/$\sqrt{\text{Hz}}$ @5 Hz (V_{in} = 100 mV)

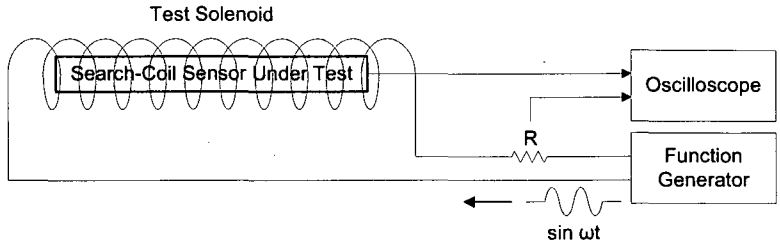

Figure 2-16: Test setup for search-coil magnetic sensor deviation test.

2.4.4 Deviation Tests

The deviation test is to confirm that the multiple magnetometer systems that will be deployed as an array perform the measurements of magnetic fields with minimal deviation between the systems and thus to ensure data quality appropriate for simultaneous observations. The deviation tests are conducted for the search-coil magnetic sensors and the analog electronics separately.

Search-Coil Magnetic Sensor Deviation Test The test setup for the search-coil magnetic sensor deviation test is similar to the one for the frequency response and resolution test except that the main analog electronics is not included in the sensor deviation test (see Figure 2-16). Input signals of peak-to-peak amplitude of $V_{p-p} = 0.144$ V across R (=1 $k\Omega$) over the sweep frequency range (0.1 – 100 Hz) are given by the function generator to the test solenoid to produce $B =\sim 160$ nT. The output voltages from each search-coil magnetic sensor are measured and compared with the outputs from the other sensors. The average output peak-to-peak voltage is approximately 3.8 V and the phase shift is $\pi/2$ over the flattop frequency response range.

Preamp and Main Analog Electronics Deviation Test This test is in principle a frequency response test only with either the preamp or the main analog electronics to confirm minimal deviation among the electronics. The input of each circuit is connected

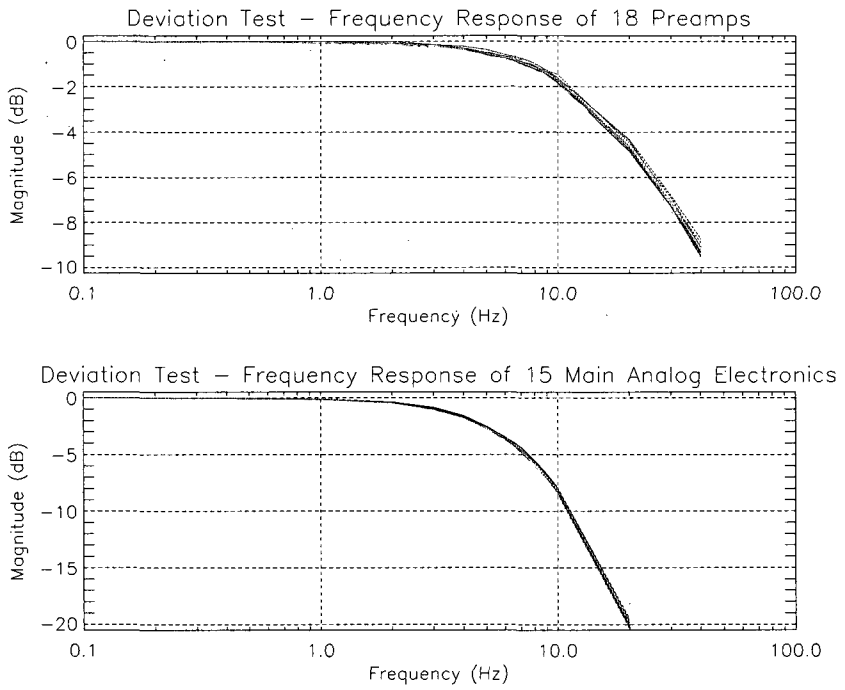

Figure 2-17: Bode plot of frequency response for deviation tests of the 18 preamps (top) and the 15 main analog electronics (bottom).

to a function generator so that an input signal (V_{p-p} = 20 mV) over the sweep frequency (0.1 – 40 Hz) is applied to the analog circuit input and the voltage of an output signal is observed using an oscilloscope. A total of 18 preamps and 15 main analog electronics have been tested for the deviation test. The deviation test results are shown in Figure 2-17. The standard deviation of the preamp outputs is 0.04 dB over the frequency range 0.1 – 5 Hz. The standard deviation of the main analog electronics outputs is also 0.04 dB over the frequency range 0.1 – 5 Hz.

2.5 Installation in the Polar Regions

The UNH ULF search-coil magnetometer systems are deployed in the polar regions such as Svalbard, Greenland, Canada, and Antarctica. Some of them are installed as a form of

array with multiple magnetometers being spaced at a distance. As mentioned earlier, the search-coil sensors are placed under the ground ~200 – 300 m away from the stations where the data acquisition systems are housed in order to protect them from being physically and electromagnetically disturbed. The magnetic field measurement using search-coil magnetometer is significantly affected by wind, too. Therefore, it is very important to secure the sensors.

The search-coil sensors are mounted on the ground with the Z sensor (up) along the geomagnetic field line, the Y sensor (east-west) horizontal and perpendicular to the Z sensor, and the X sensor (north-south) along the geomagnetic meridian, perpendicular to the Y and Z sensors. In some cases, a Z sensor is not used because measurements in the X and Y direction provide sufficient information about the magnetic activity (e.g., wave polarization).

The polarity setup of the ULF search-coil magnetic sensor, definition of coordinate system applied to the sensor installation, and orientation of the sensors for ground installation are shown in Figure 2-18. A magnetic perturbation along the sensor axis in the direction toward the sensor connector is defined as a "positive" signal, meaning that it produces a positive voltage out of the preamp when magnetic flux increases in the direction of the arrow as shown in Figure 2-18a. The orientation of the sensors when installed on the ground is determined by using Cartesian coordinate systems: X (geomagnetic north), Y (geomagnetic east) and Z (field line) in the northern hemisphere (Figure 2-18b); X (geomagnetic south), Y (geomagnetic east), and Z (field line) in the southern hemisphere (Figure 2-18c). The sensor 1 is oriented along the geomagnetic north-south direction (magnetic meridian), which can be found by on-site measurement using a compass, making an angle perpendicular to the local magnetic field inclination to the ground (= 90°− inclination). The inclination of the Earth's magnetic field can be obtained by an IGRF model. Figure 2-19 shows an example of the installation of the search-coil sensors under the ground.

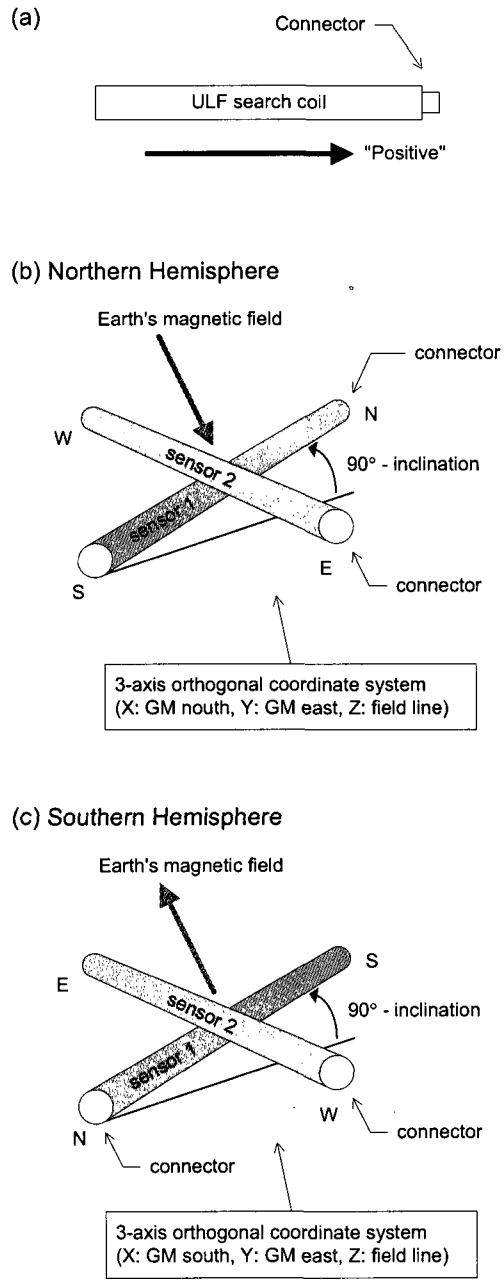

Figure 2-18: (a) Polarity setup of the ULF search-coil magnetic sensor; definition of coordinate systems applied to the sensor installation and orientation of the sensors for ground installation (b) in the northern hemisphere and (c) in the southern hemisphere.

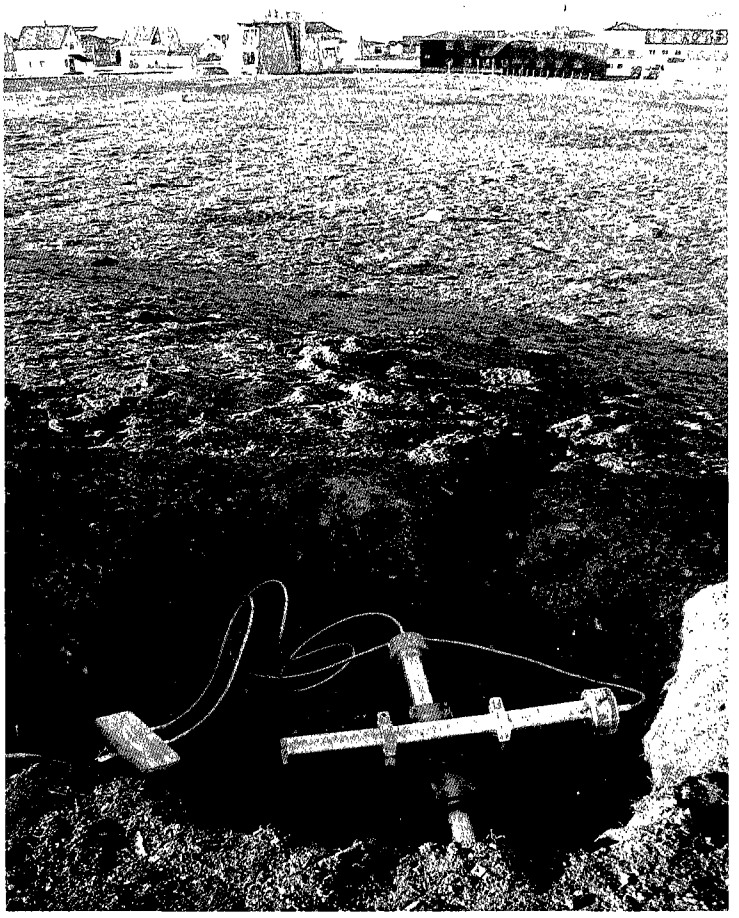

Figure 2-19: UNH ULF search-coil magnetic sensors (X and Y components) installed under the ground in Ny Ålesund, Svalbard.

Chapter 3

Ducting Characteristics of Pc 1 Waves at High Latitudes on the Ground and in Space

3.1 Introduction

ULF Pc 1 (0.2 – 5 Hz) geomagnetic pulsations include electromagnetic ion cyclotron (EMIC) waves generated by the cyclotron instability of hot, anisotropic protons in the equatorial region of the magnetosphere in the energy range of $\sim 1 - 100$ keV (Brice 1965, Cornwall 1965, Anderson et al. 1996, Kangas et al. 1998). The theoretical studies (e.g., Horne & Thorne (1993)) and the observations (e.g., Anderson et al. (1996)) suggest that Pc 1 waves are generated close to the magnetic equator. It is generally accepted that left-hand polarized (LHP) Alfvén Pc 1 pulsations propagate along the geomagnetic field lines from the magnetosphere to the ionosphere and couple to right-hand polarized (RHP) compressional (fast), isotropic waves in the ionosphere (called the "ionospheric source region" or the "wave injection region") (Fraser 1975*a*,*b*, Altman & Fijalkow 1980, Fujita & Tamao 1988). It has also been shown in theory and observations that the compressional waves are trapped in the ionospheric waveguide (or duct), centered around the Alfvén speed minimum (electron

density maximum, at an altitude of $\sim$ 400 km) near the F2 region bounded by the E region ($\sim$ 100 km) and a region where the Alfvén speed increases sharply ($\sim$ 1000 km), after mode conversion from the incident Alfvén waves to the horizontally propagating compressional waves by the anisotropic ionospheric Hall currents as shown in Figure 1-7 (Tepley & Landshoff 1966, Manchester 1966, Greifinger & Greifinger 1968, Fujita & Tamao 1988).

Tepley & Landshoff (1966) discussed a waveguide theory for ionospheric propagation of MHD waves and mode conversion through collisional processes in the ionosphere. Manchester (1966) suggested that as the walls of the duct are not perfect reflectors, the wave is attenuated as it propagates down the duct. A model result in Greifinger & Greifinger (1973) showed that duct propagation is most efficient along the magnetic meridian. The model suggested by Fujita & Tamao (1988) showed an attenuation rate of 8 dB/100 km near the injection region. They also predicted higher attenuation with increasing dip angle at high latitudes. Ground observations by Hayashi et al. (1981) at high latitudes using a search-coil magnetometer array found that ULF Pc 1 waves propagated from an injection region in a concentric pattern of equicontour lines of its intensity and observed an attenuation of 10 dB/100 km in the injection center and 2.5 dB/100 km in the region beyond 500 km from the center. Multipoint observations by Neudegg et al. (2000) estimated the average attenuation of 41 dB/1000 km and suggested that the attenuation of waves did not always occur in a consistent and linear fashion, probably due to a leaky waveguide as described in Manchester (1968).

Greifinger & Greifinger (1968) estimated that the ionospheric Alfvén speed varies approximately between 200 and 700 km/s depending on local time and sunspot conditions. Neudegg et al. (1995) found a Pc 1–2 propagation speed of 300 – 800 km/s from a ground-based magnetometer array located at high latitudes over a range of a few hundred km. A model by Lysak (2004) concludes that the wave front propagates on the order of 1000 km/s

in the ionospheric waveguide across magnetic field lines and the fast mode wave speed in the ionosphere is close to the Alfvén speed.

The polarization characteristics of geomagnetic pulsations can provide information about the source region and about the wave propagation from the source to the ground. Theoretical approaches by Baranskiy (1970), Greifinger (1972), Altman & Fijalkow (1980), and Fujita & Tamao (1988) showed transmitted LHP Alfvén waves vertically incident on the ionosphere gradually change to RHP as distance from the injection region increases as observed on the ground. Many observations using ground arrays also found the polarization sense changes from predominantly LHP around the injection region to RHP away from the injection region and the ellipticity becomes linearly polarized (LP) with the major axis aligned with the injection location (Summers & Fraser 1972, Fraser & Summers 1972, Fraser 1975*a*, Hayashi et al. 1981, Webster & Fraser 1985).

Fraser (1975*a*) estimated the general location of the injection region near the dawn terminator in the range $58°-66°$ ILAT ($L = 3.5-6$) using the polarization ellipse major axis azimuthal directions and direction of arrival triangulation method. Simultaneous multipoint ground and satellite observations by Erlandson et al. (1996) estimated the latitudinal extent of the Pc 1 source at Viking's altitude at $L = 5.1 - 5.5$ ($63.7° - 64.7°$ ILAT), which corresponds to a latitudinal width of 120 km at ionospheric altitude. The Magsat satellite observations by Iyemori & Hayashi (1989) also showed a source region of < 100 km in the ionosphere F region at $58°$ to $60°$ ILAT. The latitudinal width of the source of $\sim 0.5°$ in ILAT has been obtained by Mursula et al. (1994). The ST5 satellite observations of Pc 1–2 waves by Engebretson et al. (2008) and satellite-borne proton precipitation measurements by Yahnin & Yahnina (2007) also show very narrow regions of wave activity, with a latitudinal extent of $\sim 0.5° - 1°$ ($\sim 50 - 100$ km).

This study describes ULF Pc 1 geomagnetic pulsations observed from a ground array of

search-coil magnetometers predominantly in the morning sector of Antarctica. With extensive latitudinal coverage along the magnetic meridian, the five search-coil magnetometers show very well-defined poleward spectral power attenuation and polarization change of the waves suggesting wave propagation in the ionospheric waveguide (ducting). Halley Station, located at the lowest latitude among the stations in the array, typically observes the highest spectral wave power and well-defined band-limited signatures. The same wave event, showing less wave power, is found at the other four remote stations at higher latitudes. The conjunction of an overflight of the CHAMP satellite for the event provides a measure of the incident wave power in the ducting layer at 350 km altitude. Data from CHAMP reveal that Pc 1 waves enter the ionosphere across a lmited latitudinal range and that the waves are LP.

3.2 Instrumentation and Data

The ground data presented in this study were obtained from the five ULF search-coil magnetometers deployed at Halley Station (HBA), South Pole Station (SPA), and three automated geophysical observatories (AGOs) in Antarctica on Mar. 23, 2007. They provide three-axis vector samples of dB/dt in local geomagnetic coordinates with X northward, Y eastward, and Z upward parallel to geomagnetic field at a rate of 10 samples/sec (Engebretson et al. 1997). Table 3.1 shows the geographic and corrected geomagnetic locations of the ground stations used in this study. This Antarctic ground-based magnetometer array provides observations over an unprecedented latitudinal extent covering geomagnetic latitudes of $-62°$ to $-87°$ (over the distance of 2920 km) as shown in Figure 3-1 and has been showing very well-defined ULF wave ducting events over the entire extent of the array.

Observations of the ULF waves were also made in the ducting layer by the CHAMP satellite, which was in almost circular, near polar (inclination = 87°) orbit with an altitude

Station	Station Code	Geographic Lat.	Geographic Lon.	Geomagnetic Lat.	Geomagnetic Lon.	L	MLT MN in UT	Distance from HBA (km)
Halley	HBA	−75.50	333.40	−61.56	29.01	4.4	0243	0
AGO P2	P2	−85.67	313.62	−69.84	19.33	8.4	0329	1170
South Pole	SPA	−90.00	0.0	−74.02	18.35	13.2	0335	1610
AGO P1	P1	−83.86	129.61	−80.14	16.87	34.1	0344	2252
AGO P5	P5	−77.24	123.52	−86.74	29.46	309.2	0252	2920

Table 3.1: Geographic and geomagnetic locations of the Antarctic stations used in this study. Geomagnetic coordinates, dipole L-values, and MLT MN in UT are obtained from NASA GSFC Modelweb Website, http://modelweb.gsfc.nasa.gov /models/cgm/cgm.html, for epoch 2007, assuming an altitude of 100 km.

of approximately 350 km during the time of this study. The CHAMP satellite is equipped with a fluxgate magnetometer, which provides three axis vector background magnetic field data at a maximum rate of 50 Hz over the bandwidth (−3 dB) of 13 Hz. During the events in this study, the CHAMP satellite flew over the ground stations with a very good MLT conjunction. The satellite footprint from 0835 to 0845 UT with a ground conjunction is also shown in Figure 3-1.

CHAMP data are originally acquired in a satellite coordinate system in which the X axis is approximately along the direction of the satellite track, the Z axis points downward, and the Y axis completes a right-handed set. A coordinate transformation is carried out for this study in order to examine the wave mode in the ionospheric ducting layer after the data are detrended to obtain time-varying magnetic fields ($\mathbf{b}$) by subtracting background magnetic fields ($\mathbf{B}_0$). In this study, a smoothing of the original data from the satellite has been used as background field. One of the three components in the new coordinate system represents a compressional wave component ($b_\parallel$), which is denoted by "B_par" in the figures of the satellite data shown herein. Compressional perturbations can be obtained by projecting the detrended data onto the background magnetic fields. The other two components in the new coordinate system contain wave power perpendicular to the background magnetic

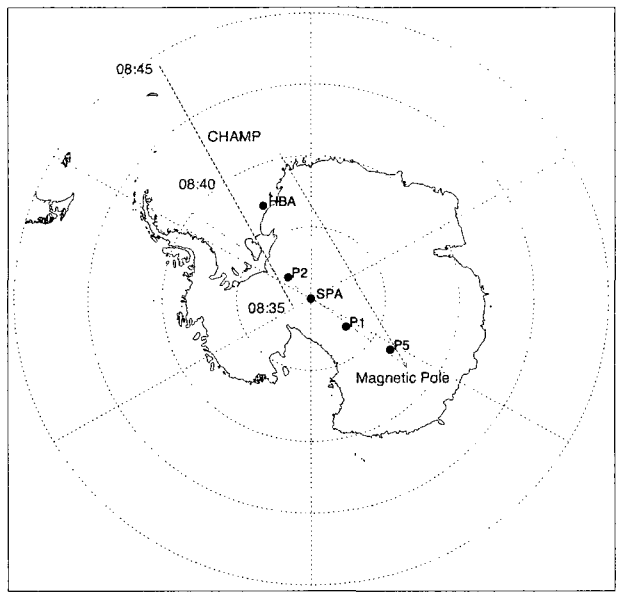

Figure 3-1: Map of Antarctica showing the ULF search-coil magnetometer array used for this study. The geomagnetically most poleward station, P5, and the other four stations, P1, P2, SPA and HBA are aligned well with the magnetic meridian. This map also shows the southern hemisphere ground track of the magnetic field lines traversed by the CHAMP satellite from 0835 to 0845 UT on March 23 2007, based on data from the Satellite Situation Center Web utility, available at http://sscweb.gsfc.nasa.gov.

fields, which is, for this study, decomposed into perpendicular perturbations in the azimuthal ($b_{\perp\varphi}$) and in the meridional direction ($b_{\perp\theta}$), which conforms to the right-hand rule. They are denoted by "B_perp_phi" and "B_perp_theta" respectively in the figures of the satellite data shown herein. The perpendicular azimuthal perturbation ($b_{\perp\varphi}$) is calculated by projecting the detrended data ($\mathbf{b}$) onto the azimuthal vector ($\hat{\varphi}$, normal of the magnetic meridian). The azimuthal vector ($\hat{\varphi}$) can be obtained by crossing the background magnetic field unit vector ($\mathbf{B}_0/B_0$) and the vertical field component from the original CHAMP data ($\mathbf{B}_z/B_z$) (i.e., $\hat{\varphi} = \mathbf{B}_0/B_0 \times \mathbf{B}_z/B_z$). The perpendicular meridional perturbation ($b_{\perp\theta}$), which completes the triad ($\hat{\theta} = \hat{\varphi} \times \mathbf{B}_0/B_0$), is then calculated by projecting the detrended data ($\mathbf{b}$) onto the meridional vector ($\hat{\theta}$). Appendix C decribes the coordinate transformation in more detail.

The new set of the three components is thus summarized as follows.

$$
\begin{aligned}
b_{\parallel} &= \mathbf{b} \cdot \mathbf{B}_0 / B_0 \\
b_{\perp\theta} &= \mathbf{b} \cdot \hat{\theta} \\
b_{\perp\varphi} &= \mathbf{b} \cdot \hat{\varphi}
\end{aligned}
$$

3.3 Observations and Interpretations

Well-defined, band-limited ULF Pc 1 waves were measured by the five ULF search-coil magnetometer systems deployed in Antarctica as shown in the stacked 0 – 1 Hz, 2048-point FFT spectrograms (with Hanning window) in Figure 3-2. Wave power as a function of frequency (0 – 1 Hz) in the X (north-south) and Y (east-west) components and time is plotted for a 5 hour interval (from 0800 to 1300 UT) on Mar. 23, 2007. The data from the X component at AGO P5 was unavailable during the observation. As shown in Figure 3-2, identical spectral patterns albeit attenuated across the network suggest that the waves were generated in a localized region within the ionosphere. Otherwise, such identical spectral signatures may not be detected over the wide range.

The distance between the station at lowest magnetic latitude (HBA) and the one at highest magnetic latitude (P5) is 2920 km. The three stations P2, SPA and P1 are aligned approximately along a magnetic meridian within 15 min MLT while HBA is somewhat off-meridian (600 km from the meridional line of the three stations). The MLT difference at P5 is not very significant as it is close to the magnetic pole. The spectral structures over the frequency ranges between 0.3 and 0.6 Hz are most clearly registered at the station located at lowest magnetic latitude, Halley Station (HBA, $L = 4.4$) from 0830 to 1230 UT. There is some period during which multiple band structures are observed.

As shown in Table 3.1, the MLT is approximately 3 hours behind UT, which indicates

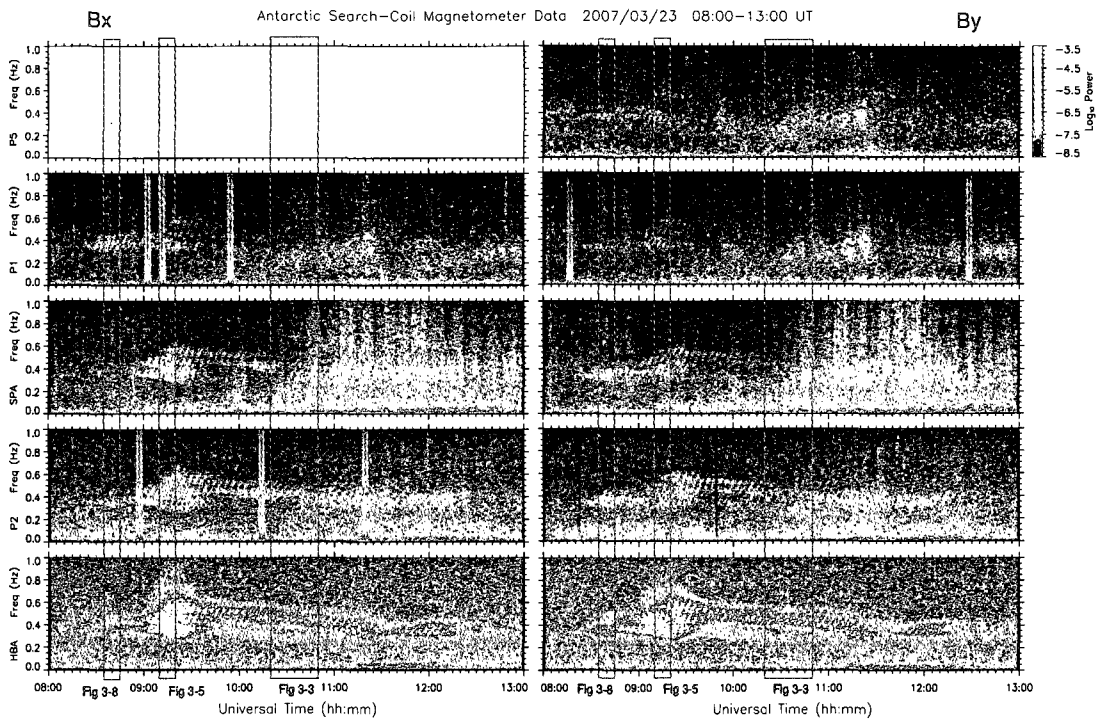

Figure 3-2: Stacked 0 – 1 Hz Fourier spectrograms in the X (north-south) (left panels) and Y (east-west) (right panels) components of the search-coil data showing the ULF Pc 1 waves recorded at the Antarctic stations, Halley (HBA), P2, South Pole (SPA), P1, and P5 from 0800 to 1300 UT on March 23, 2007. The stations are located along the magnetic meridian covering from geomagnetic latitudes of $-62°$ to $-87°$ with the lowest latitude station at the bottom of the plot. Spectral power attenuation as the waves are ducted poleward is clearly registered. X axis data from AGO P5 were unavailable during this interval. Note that the time intervals of Figure 3-3, Figure 3-5, and Figure 3-8 are indicated.

that the events occurred in the morning sector. Based on the fact that the event was most clearly shown at HBA ($L = 4.4$), in this lower L-shell, EMIC waves in the Pc 1 frequency range are likely to be generated by protons and heavy ions in the ring current (near the equator) and propagate along the field lines. The wave spectral power attenuation is displayed in Figure 3-2 as the latitude increases, which suggests that the waves propagated poleward in the ionospheric waveguide along the magnetic meridian.

Figure 3-3 shows the temporal and spectral structures of the Pc 1 waves in a shorter time scale in order for the detailed structures to be displayed (the event during this period is

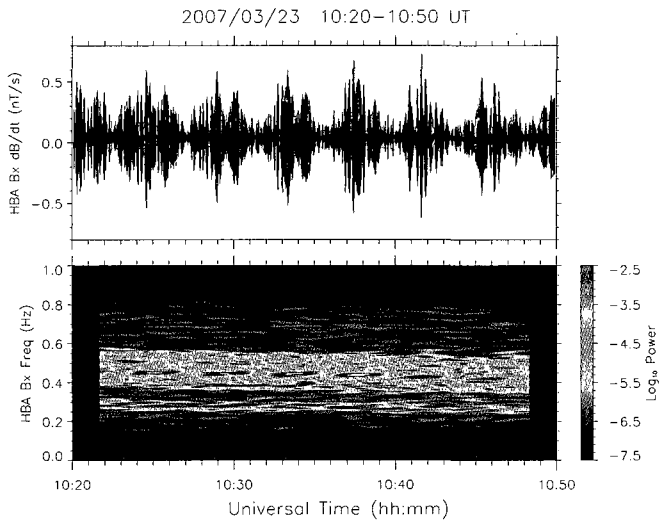

Figure 3-3: Temporal and spectral structures of the ULF Pc 1 waves (called "pearls") measured from HBA in a shorter time scale (from 1020 to 1050 UT). Wave modulation with approximately 3 min period is clearly shown. Note that the event during this period is indicated in Figure 3-2.

indicated in Figure 3-2). Wave modulations are observed at HBA during almost the entire event while the other stations at higher latitudes also detected the same signatures but with less spectral power and shorter duration. Such spectral features fall into a ULF subclass, called "pearls" or "structured Pc 1", which are characterized by periodic variations of the wave amplitude, thus appearing as pearls on a string when plotted as a time series. The repetition period is approximately 3 min. The structured Pc 1 is one of the most frequently observed Pc 1 waves and is suggested to propagate in the ducting layer (Mursula et al. 2001).

The CHAMP fluxgate magnetometer measured very similar Pc 1 waves over the frequency band ($\sim$ 0.3 to 0.5 Hz) approximately from 0840 to 0843 UT. The signature measured by CHAMP is shown over a limited extent ($-53°$ to $-61°$ ILAT) while the ground array detected the wave at higher latitudes over a wider range ($-62°$ to $-87°$ ILAT). This study focuses on the ULF waves observed in space and on the ground and their propagation

characteristics in the ionospheric ducting layer. The pearl structure is not within the scope of this study and will be left for future work.

The following four subsections describe the Pc 1 events and their ducting characteristics in the ionosphere in more detail. Wave power attenuation, wave propagation speed, and polarization are discussed in the first three subsections (3.3.1 through 3.3.3), respectively. The last subsection (3.3.4) presents the spatial extent of the Pc 1 wave injection region observed by the CHAMP satellite.

3.3.1 Spectral Power Attenuation

Spectral power attenuation is one of the features typically observed in a ducted wave event. Figure 3-4 shows the absolute power spectra ($\log_{10}$ power versus frequency) of the ULF Pc 1 events observed by the Antarctic search-coil array and the wave power attenuation (in dB) over the distance from HBA (in km) at four selected frequencies (0.3, 0.4, 0.5, and 0.6 Hz). Two different time periods are examined for this analysis in an attempt to separate wider band structure (from 0915 to 0945 UT in Figure 3-4a) and narrower band structure (from 0945 to 1015 UT in Figure 3-4b). Each graph displays the results from both X and Y components. In the power spectra depicted in Figure 3-4a, three spectral peaks are observed (predominantly in the X component), which are also seen in Figure 3-2.

The attenuation (in dB) is obtained by multiplying the $\log_{10}$ power in the power spectra by 10. The wave power values at each selected frequency ± 0.01 Hz (this bandwidth corresponds to 5 bins in the 2048-point spectrogram) during the event period are averaged and line-fitted to estimate attenuation over distance. From the results in Figure 3-4, the attenuation factors appear to be approximately between 8 dB/1000 km and 20 dB/1000 km. More specifically, there seems to be a tendency for the attenuation factor to increase with increasing frequency, which is in agreement with Greifinger & Greifinger (1968), although

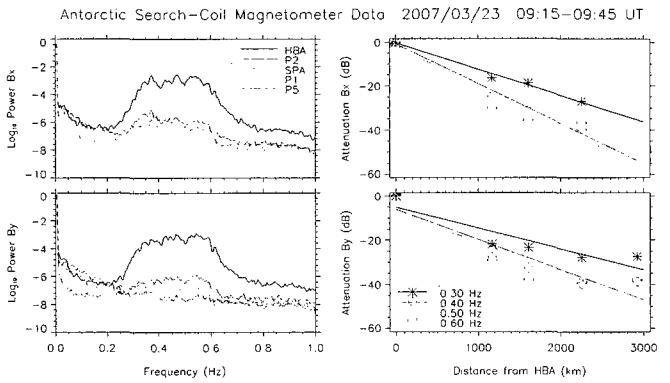

(a)

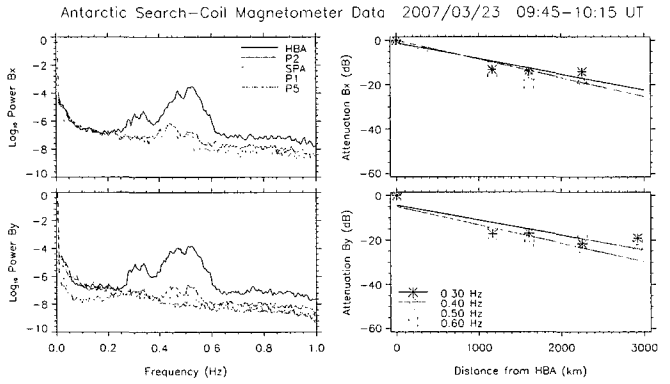

(b)

Figure 3-4: Power spectra ($\log_{10}$ power versus frequency) of the ULF Pc 1 events observed by the Antarctic search-coil array and wave power attenuations (in dB) over the distance from HBA (in km) at four selected frequencies (0.3, 0.4, 0.5, and 0.6 Hz) during the two time periods, (a) 0915 – 0945 UT and (b) 0945 – 1015 UT. The graphs for each time period display the results from both X and Y components.

the stations located far from HBA (P1 and P5, in particular) show no clear tendency of spectral power attenuation, probably due to the poor signal-to-noise ratio. It should also be noted that in general, attenuation in the waveguide may not occur in a linear fashion due to its inhomogeneous conductivity and the leaky ionospheric layer (Manchester 1968, Neudegg et al. 2000, Fraser & Nguyen 2001).

The average attenuation factor observed in this study appears to be much lower than that of many other previous studies. The model study by Fujita & Tamao (1988) reported

$\sim$ 8 dB/100 km and the ground observations by Hayashi et al. (1981) showed 10 dB/100 km near the injection center and 2.5 dB/100 km in the region beyond 500 km from the center using a network of 13 stations at high latitudes spanning 30° in longitude and 15° in latitude (from 53.7°N, 290.9°E to 75.1°N, 328.0°E, CGM). Note that these studies used "per 100 km" instead of "per 1000 km". The comparison between model and observation by Manchester (1970) reported $\sim$ 1 – 8 dB/1000 km at low/mid-latitudes. Neudegg et al. (2000) obtained $\sim$ 41 dB/1000 km using a closely-spaced ($\sim$ 150 km) triangular network near Davis, Antarctica (74.6° S, 102.3° E, CGM) and suggested that the high attenuation might be due to higher dip angle at high latitudes as predicted by Fujita & Tamao (1988). Hayashi et al. (1981) observed both poleward and equatorward attenuation and concluded that poleward propagation shows slightly less attenuation.

In general, the wide range of attenuation factors obtained from the model/observation studies seem to be related to the fact that wave propagation in the ionospheric waveguide is susceptible to the variation of ionospheric conditions. In addition, since the configurations of the arrays in these studies are different both in latitudinal and longitudinal extent and the distances between the possible injection regions and the arrays are not necessarily the same, attenuation factors can be obtained with quite a large uncertainty if the attenuation is not linear. Moreover, the more efficient poleward than equatorward ducting might be attributed to incident Poynting flux being initially poleward based on the fact that the incident waves are field-aligned Alfvén waves (field lines are angled pointing toward the Poles).

The observations in this study, showing much less attenuation compared to the other previous observations, are unique in that the ducted waves, seen over an array with unprecedented geomagnetic latitudinal range and positioning along a magnetic meridian (a condition that provides the most efficient ducting as suggested by Greifinger & Greifinger

(1973)), have rarely been measured before.

3.3.2 Propagation Speed

Propagation in the ducting layer occurs in the form of compressional waves with a speed of the order of the Alfvén speed in the region. As described earlier, similar patterns of the spectral signatures of the Pc 1 waves are observed at different ground stations. Although wave power was found to attenuate as the waves propagated poleward, the presence of the pearl structure remains clear. By taking the consistent spectral patterns over the large extent in latitude and their attenuations into account, the idea that waves are ducted in the ionospheric waveguide is suggested. In temporally extended time-series plots and spectrograms as shown in Figure 3-5, propagation time delays among the stations during the event are observed by comparing the onset time of the temporal and spectral signatures (indicated by vertical lines in Figure 3-5). Note that the event during this period is indicated in Figure 3-2. The propagation time delay between HBA and SPA, which are separated by $\sim$ 1600 km, appears to be $\sim$ 18 sec, indicating that the propagation speed is $\sim$ 89 km/s. In this study, the data from P1, P2, and P5 are not used since slight timing errors due to the issues of the data acquisition modules at those stations were known to occur.

The propagation speeds obtained by the previous theoretical estimations and observations range from $\sim$ 360 to 720 km/s (day-night, sunspot minimum) and $\sim$ 190 to 400 km/s (day-night, sunspot maximum) (Greifinger & Greifinger 1968); $\sim$ 500 to 800 km/s (Manchester 1970); $\sim$ 540 to 2500 km/s at mid latitudes (Fraser 1975*a*); and $\sim$ 1000 km/s (Lysak 2004). Neudegg et al. (1995) using a triangular network in Antarctica measured speeds of $\sim$ 150 to 750 km/s. The propagation speed estimated for the event in this study ($\sim$ 89 km/s) is lower than most of the results from the previous studies. Greifinger & Greifinger (1968) discussed that variation in propagation speed is largely dependent on ionospheric condi-

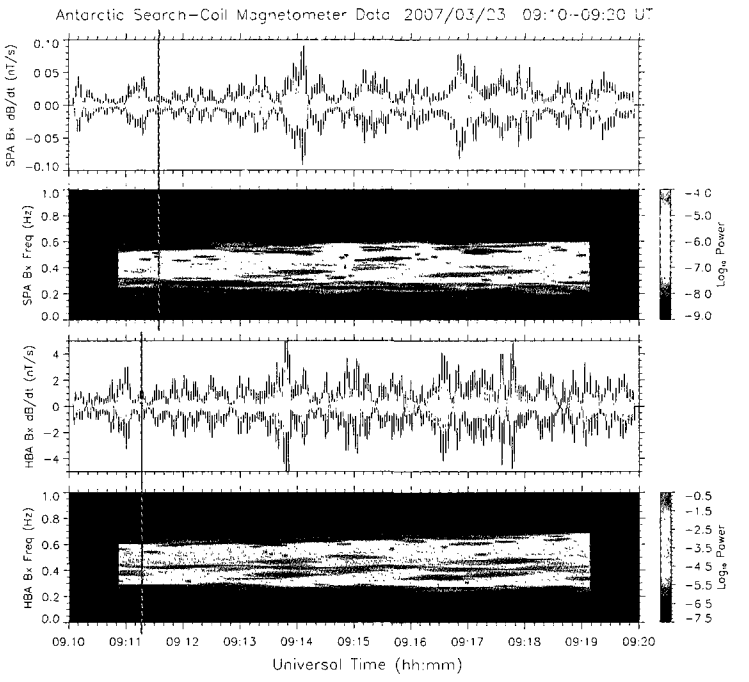

Figure 3-5: Propagation time delay in the temporal and spectral structures observed from HBA and SPA. This event period is band-pass filtered over 0.3 – 0.5 Hz for the structures to be seen more clearly. The wave arrival time is delayed by $\sim$ 18 sec between the stations, which are separated by $\sim$ 1600 km. The wave packets and the spectral patterns that are compared for the timing are indicated by vertical lines. Note that the event during this period is indicated in Figure 3-2.

tions. We do not, however, exclude a possibility of misinterpretation of the data, which can be caused by relatively big systematic error due to the difficulties in analyzing the data acquired from the stations which are separated beyond the range where autocorrelation and phase correlation analyses are reliably performed.

3.3.3 Polarization

Two polarization properties - ellipticity and polarization angle are discussed in this study. Ellipticity (ε) is defined as the ratio of the minor axis to the major axis of the ellipse of magnetic field perturbation in the plane perpendicular to the background magnetic field. Ellipticity is represented in three ranges: $\varepsilon \geq 0.2$ right-hand polarization (RHP); $\varepsilon \leq$

-0.2 left-hand (LHP); and $|\varepsilon| < 0.2$ linear (LP) as specified in Anderson et al. (1992). Polarization major axis angle (θ, polarization angle in short) is the angle between the major axis of the polarization ellipse and the magnetic meridian in the north-south direction. Changes of the polarization properties of the waves during the propagation are shown in Figure 3-6 and Figure 3-7, in which a polarization analysis technique as described in Fowler et al. (1967) and Rankin & Kurtz (1970) is used to display ellipticities and polarization angles in a plot of frequency versus time. See Appendix A for more details about the polarization analysis technique used in this study. The ellipticity as shown in Figure 3-6 is represented in a color scale with -1 being LH circular polarization (negative ellipticity) and $+1$ being RH circular polarization (positive ellipticity). LP is defined as having $|\varepsilon| < 0.2$ as mentioned earlier. Ellipticities are displayed only for frequencies which exceed a certain power threshold appropriate to the signal-to-noise ratio. Figure 3-7 shows the polarization angle change during the wave propagation. In this type of analysis, polarization angle ranges between $-90°$ and $+90°$. The sign represents the direction of angle with respect to the magnetic meridian in the north-south direction (X component in the magnetometer data) with positive angle being counterclockwise and negative angle being clockwise.

The waves observed at lower latitudes are predominantly LHP while RHP signals are more dominant at higher latitudes. The intermediate stations such as P2 and SPA detect intermediate features, i.e., LP. This overall tendency of the wave polarization sense change from LHP to RHP during propagation appears to be in good agreement with many other observations (e.g., Hayashi et al. (1981) and Inhester et al. (1984)) and models (e.g., Greifinger & Greifinger (1968), and Fujita & Tamao (1988)). To summarize, it is commonly suggested in the literature that this result implies that 1) LHP Alfvén waves, originating in low latitude regions, are transmitted into the ionosphere; 2) the waves propagate in the ionospheric waveguide; 3) the LHP waves, observed in the vicinity of the injection region,

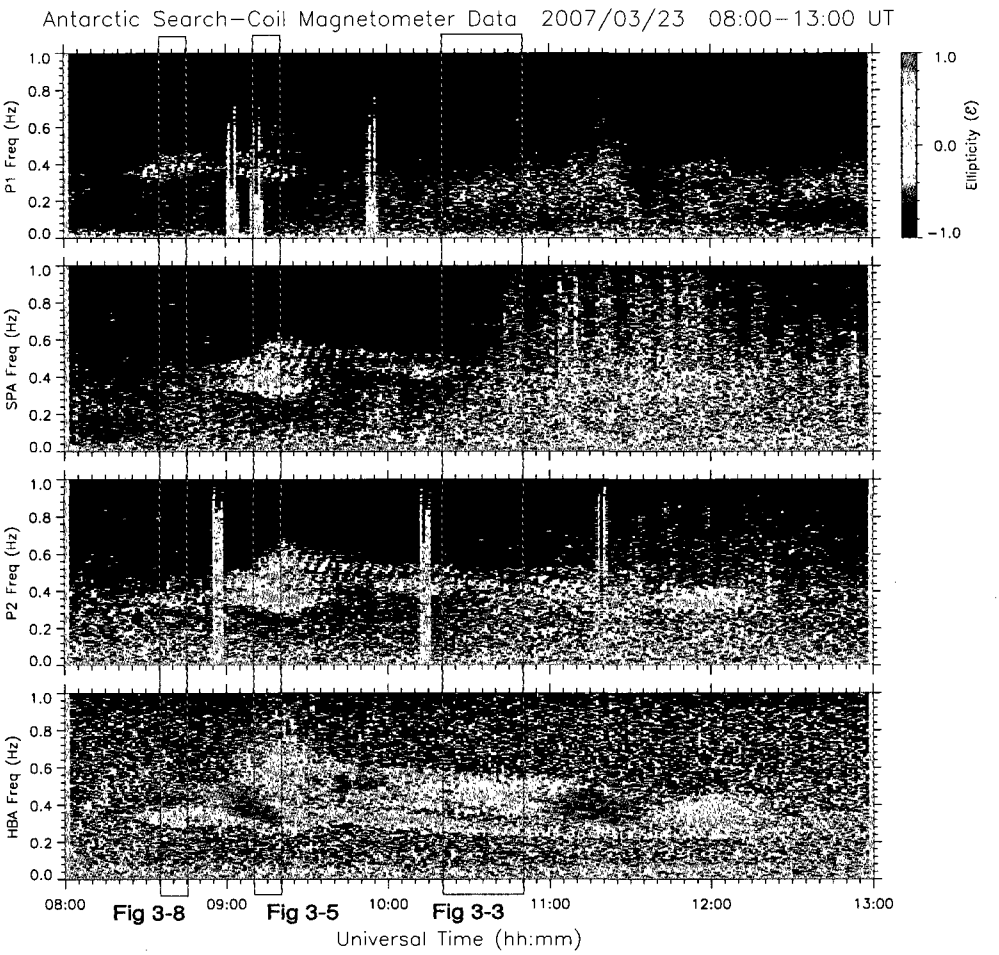

Figure 3-6: Polarization ellipticity (ε) of the ULF Pc 1 waves observed by the ground array from 0800 to 1300 UT on March 23, 2007 in a plot of frequency versus time. The ellipticity is shown in a color scale with -1 being LH circular polarization (negative ellipticity) and $+1$ being RH circular polarization (positive ellipticity). LP is defined as having $|\varepsilon| < 0.2$. Note that the time intervals of Figure 3-3, Figure 3-5, and Figure 3-8 are indicated.

gradually change to RHP (with LP observed between LHP and RHP) as distance from the injection region increases.

It should be noted, however, that there are other spectral components in which the polarization changes in a different way. For example, Figure 3-6 shows that the spectral signatures observed from 0820 to 0900 UT at HBA contain two dominant polarization senses - LP signals over the frequency range between 0.3 and 0.35 Hz ($\varepsilon =\sim -0.1$) and LHP between 0.35 and 0.5 Hz ($\varepsilon =\sim -0.25$ to -0.45). It is clearly shown that at AGO P1, the polarization sense appears to be opposite to those at HBA between the two frequency ranges (0.3 and 0.35 Hz; 0.35 and 0.5 Hz). This tendency is seen at other frequencies in other times.

The complexity of the polarization patterns as seen in Figure 3-6 might be due to the horizontal inhomogeneity of the conductivity in the ionosphere. Waves with multiple frequency components from different injection regions can also affect the pattern. Superposition effects through refraction, reflection, and transmission in the waveguide can also be considered. A model study by Belova et al. (1997) showed how the polarization pattern on the ground can change in a complicated fashion as the inhomogeneity of the ionospheric conductivity varies. Hayashi et al. (1981) reported greater variation of polarization properties at high latitudes and suggested that the lack of uniformity in the polarization pattern appeared to be related to the fact that the array is located close to the wave injection region where the combination of incident waves and ducted waves is more dominant.

Wave polarization is one of the properties that show the spatial characteristics of the wave propagation and media. EMIC waves are LHP and, within the extent of the incident wave into the ionosphere, the ground data also show LHP. It has also been suggested in theory and observations that the polarization of Pc 1 waves on the ground shows concentric patterns of polarization sense changing from LHP within the extent of the wave injection

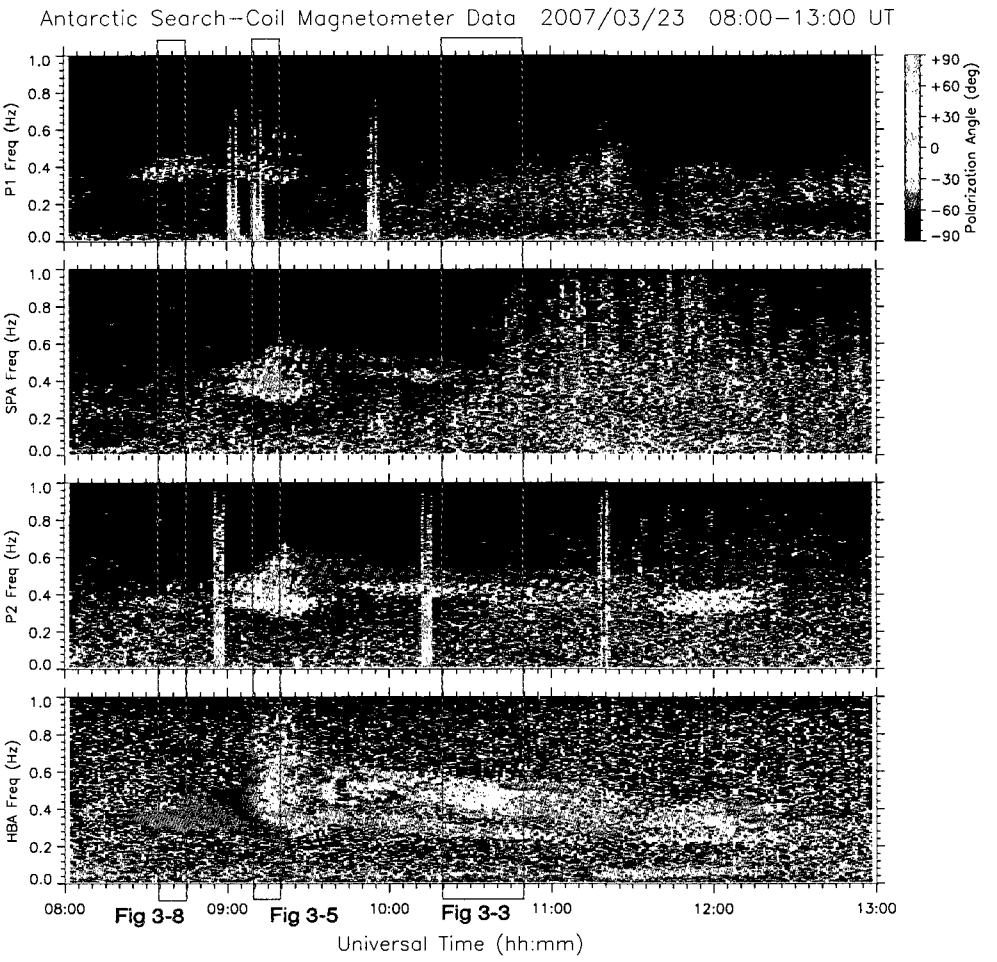

Figure 3-7: Polarization angle (θ) of the ULF Pc 1 waves observed by the ground array from 0800 to 1300 UT on March 23, 2007 in a plot of frequency versus time. The angle change ranges between $-90°$ and $+90°$. The sign represents the direction of the angle with respect to the magnetic meridian in the north-south direction (X component in the magnetometer data) with positive angle being counterclockwise and negative angle being clockwise. Note that the time intervals of Figure 3-3, Figure 3-5, and Figure 3-8 are indicated.

region to RHP outside the lateral extent of the injection region with LP shown in transition of the sense change (Greifinger 1972, Hayashi et al. 1981, Fujita & Tamao 1988). Since incident waves are attenuated rapidly with distance (Hayashi et al. 1981) and mode conversion from the incident Alfvén mode waves to the ducted compressional mode waves occurs within the extent of the injection region (Fujita & Tamao 1988), the ground signature of the ducted waves is dominant at larger horizontal distances compared to the extent of the injection region. Greifinger (1972) demonstrated that a ducted wave is nearly LP.

3.3.4 Spatial Extent of Wave Injection Region

Figure 3-1 shows the southern hemisphere ground track of the magnetic field lines traversed by the CHAMP satellite from 0835 to 0845 UT on Mar. 23, 2007 at an altitude of approximately 350 km. The orbit was lined up well with the SPA-P2-HBA line during the event. Figure 3-8 shows the spectrograms of the three components ($b_{\parallel}$, $b_{\perp\theta}$, and $b_{\perp\varphi}$) of the magnetic field data from the fluxgate magnetometer onboard the CHAMP satellite and the polarization ellipticities during the event in this study. The ground data from HBA (Y-component) is also shown in Figure 3-8 for comparison. Band-limited ULF waves over the frequency band ($\sim$ 0.4 – 0.5 Hz) are observed approximately from 0840 to 0843 UT, which have very similar spectral structures to the ULF Pc 1 waves measured on the ground array, suggesting a common localized source and ducting effect. Note that the event during the CHAMP overflight is indicated in Figure 3-2.

The time of CHAMP observation corresponds to the ILAT between $-53°$ and $-61°$ at $L = 2.9 - 4.4$. CHAMP passed HBA approximately at 0839:30 UT, the time when rather higher frequency waves ($\sim$ 0.6 – 0.7 Hz) are observed. Although the signatures are detected in both the perpendicular meridional ($b_{\perp\theta}$) and azimuthal components ($b_{\perp\varphi}$), the signals in the azimuthal component ($b_{\perp\varphi}$) are more dominant. On the other hand, no compressional

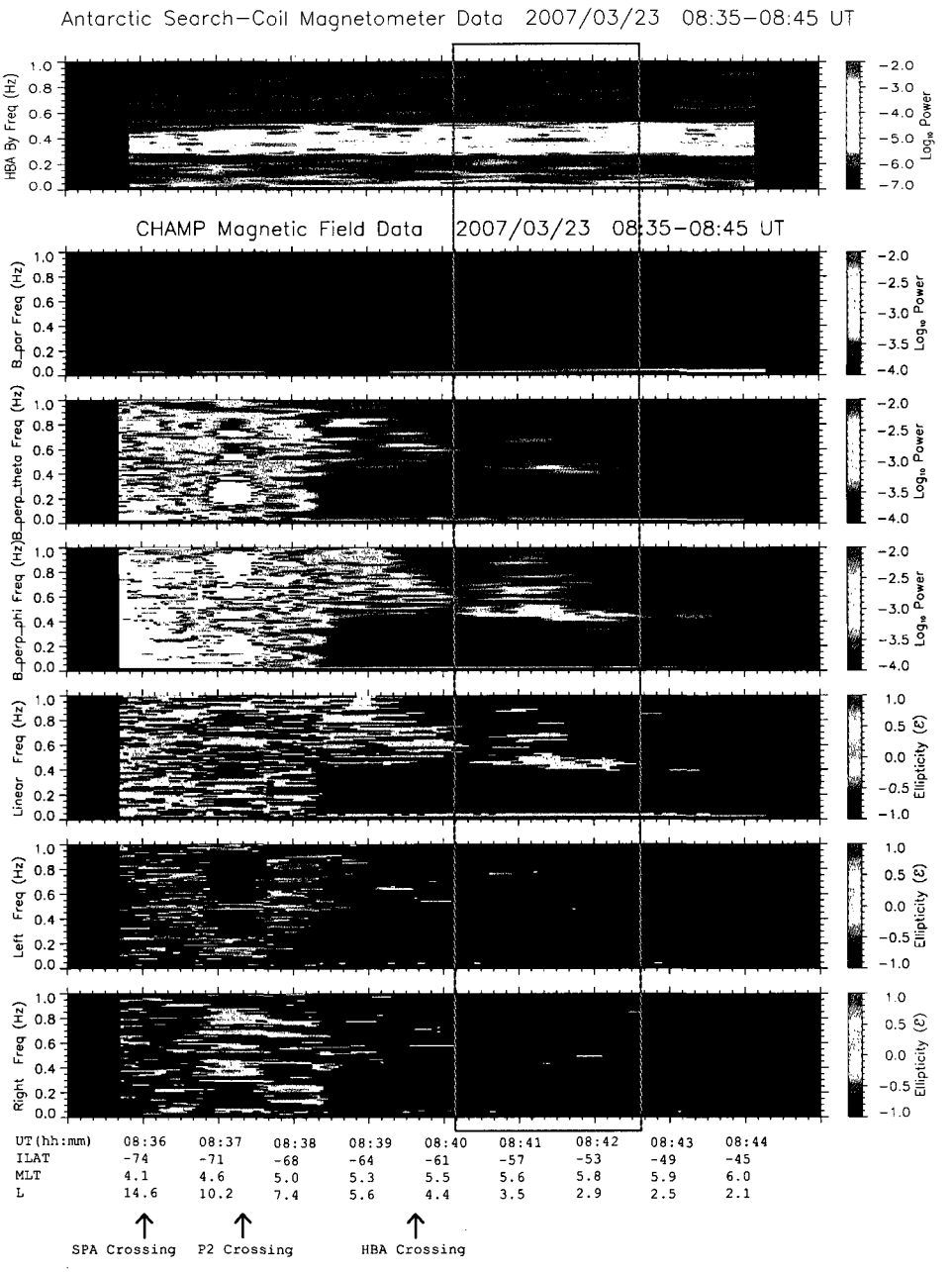

Figure 3-8: Stacked spectrograms of the Y-component of the HBA search-coil data, the three components ($b_{\parallel}$, $b_{\perp\theta}$, and $b_{\perp\varphi}$) of the magnetic field data and the polarization ellipticities (in three ranges: LP, LHP, and RHP) from the fluxgate magnetometer of the CHAMP satellite during the event in this study. Band-limited ULF waves over the frequency band ($\sim 0.4 - 0.5$ Hz) are observed approximately from 0840 to 0843 UT on Mar. 23, 2007. The satellite crossings over SPA, P2, and HBA are shown with the arrows. Note that the event during this period is indicated in Figure 3-2

power (the parallel component, $b_{\parallel}$) is detected, which indicates the waves are transverse.

The sudden disappearance of the broadband structure from the CHAMP data at 0839 UT ($L = 5.6$) is a clear indication that CHAMP passed from the plasmatrough region to the plasmasphere. The transition from broadband to narrowband signature is typically observed by CHAMP when it enters the plasmasphere. This is confirmed by using a model developed by O'Brien & Moldwin (2003) to estimate the plasmapause location at $L = 5.8$ during this event, which is close to what was seen from the CHAMP observation.

Fujita & Tamao (1988) concluded that the Alfvén wave is dominant near the wave injection region and Hall current associated with the Alfvén wave generates the ground magnetic field variations. Observations using low altitude DE-2 satellite data by Iyemori et al. (1994) showed wave injection was confined in latitude (< 100 km) and longitude and concluded that a localized region of electron temperature enhancement is caused by the direct acceleration of thermal electrons by the Alfvén ion cyclotron waves.

The ground observations by Hayashi et al. (1981) estimated the size of the injection region to be in the range 100 – 300 km in radius. Fraser et al. (1989) determined the injection region of structured Pc 1 at $L = 4.9$ just inside the plasmapause using satellite-ground observations, which is consistent with the observation results in this study. The satellite observations in the topside ionosphere by Freja (Mursula et al. 1994) showed Pc 1 activity measured in a small latitude range (60° to 63° MLAT) but a wide longitude range (03 – 14 MLT). The latitudinal extent of Pc 1–2 waves was found to be 0.3° to 1° in ILAT using ST5 satellite data (Engebretson et al. 2008). Satellite observations at high altitude by the Polar satellite showed that the EMIC wave source region at high altitudes can extend over a very large latitude range of more than 5° in ILAT although the source region of coherent EMIC waves with a constant frequency is much more limited in latitude (Mursula et al. 2001). Engebretson et al. (2008) stated that the latitudinal localization

in the magnetosphere might be attributed to the fact that EMIC waves trapped within a magnetospheric waveguide are guided along narrowly defined density gradients.

The Pc 1 signatures from the satellite and the ground station are displayed in Figure 3-9, in which time-series plots of the two perpendicular components, meridional ($b_{\perp\theta}$) and azimuthal ($b_{\perp\varphi}$) perturbations from the CHAMP magnetic field data and the three components, B_x, B_y, and B_z, of the search coil magnetometer at HBA, are shown during the Pc 1 wave event from 0840 to 0844 UT. Both satellite and ground data are band-pass filtered over 0.3 to 0.5 Hz so the ULF pulsations are shown more clearly. It appears that the time-series data from CHAMP in Figure 3-9 also display a pearl structure, which is a good comparison with the ground data. The average peak-to-peak amplitudes of the total wave activity between 0841:20 and 0842:00 UT, when the most distinct signals were detected simultaneously, are estimated at the center frequency of 0.4 Hz over the pass-band of the filter (0.3 to 0.5 Hz). CHAMP measured $b_{\perp\theta} = 0.2$ nT and $b_{\perp\varphi} = 0.4$ nT ($b_{\parallel} \approx 0$ nT), which leads to 0.45 nT in total ($= \sqrt{{b_{\perp\theta}}^2 + {b_{\perp\varphi}}^2}$), while a total of 0.08 nT in the wave activity ($= \sqrt{B_x^2 + B_y^2 + B_z^2}$) was observed from HBA. The ratio of the peak-to-peak wave amplitude at CHAMP to that at HBA is thus approximately 6. It should be noted that the ground search-coil magnetometer measures dB/dt, so the search-coil data are first converted to corresponding amplitudes of B. To be more specific, one can assume that a fluxgate magnetometer measures $B = B_0 \sin \omega t$ while a search-coil magnetometer measures $dB/dt = \omega B_0 \cos \omega t$. Therefore, the amplitude measured by the search-coil instrument is divided by ω to obtain B_0.

Iyemori & Hayashi (1989) showed that the amplitude of the Pc 1 on the ground was more than 2 orders of magnitude smaller than that observed by Magsat. Engebretson et al. (2008) found, similarly, that the amplitudes of the Pc 1 waves from the ST5 satellite observations ($\sim 5 - 100$ nT) were from 1 – 2 orders of magnitude larger than corresponding amplitudes

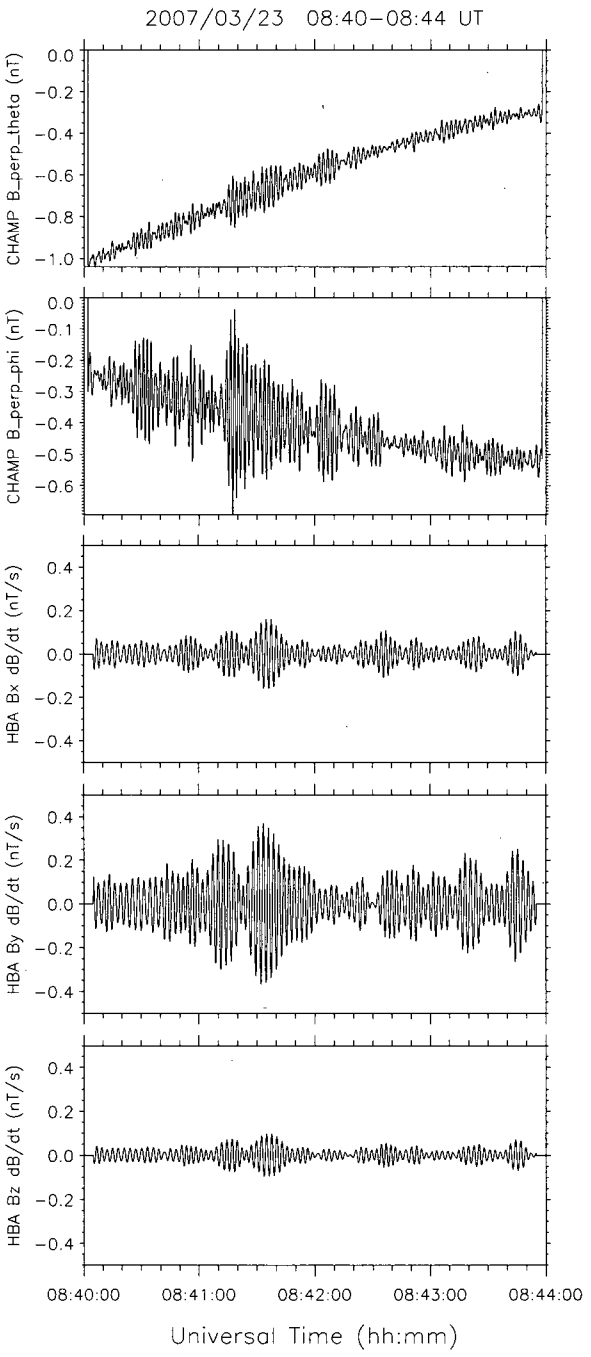

Figure 3-9: Time-series plot of the two perpendicular components, meridional ($b_{\perp\theta}$) and azimuthal ($b_{\perp\varphi}$) perturbations from the CHAMP satellite magnetic field data (first and second panels, respectively) and the three components, B_x, B_y, and B_z, of the search coil magnetometer at Halley Station, Antarctica (third, fourth, and fifth panels, respectively) during a Pc 1 wave event from 0840 to 0844 UT on Mar. 23, 2007.

observed on the ground. They pointed out that large variations in the ratio of satellite to ground amplitude may be caused by 1) variations in the spatial extent of the wave source region; 2) wave absorption and/or partial reflection by heavy ions in the magnetosphere or 3) ionospheric ducting effect of waves originating in a distant source region.

Polarization analysis of the CHAMP data as shown in Figure 3-8 indicates that the wave events are nearly LP. The wave is transverse as mentioned earlier, which is one of the characteristics of the incident wave near the wave injection region. Engebretson et al. (2008) also reported transverse Pc 1 wave activity from the ST5 satellite observation. However, whether the signal is Alfvénic cannot be determined since CHAMP has no E-field measurement. Satellite observations in the ionosphere using Magsat (Iyemori & Hayashi 1989) and ST5 (Engebretson et al. 2008) showed reversals between RHP and LHP and between elliptical and LP. Iyemori & Hayashi (1989) attributed the reversal to the coupling of the transverse and fast mode waves in the ionosphere. In theory, magnetoacoustic waves carrying the energy of Pc 1 in the ionospheric duct are LP whereas the observations have shown the waves are elliptically polarized. Baranskiy (1970) suggested the discrepancy might be due to superposition of polarized waves and thus observed signals tend to be elliptic in general and band-limited waves will show smaller ellipticity (close to LP).

Given certain assumptions, the polarization ellipse observed on the ground becomes increasingly LP with the major axis pointing toward (or away from) the wave injection region as Pc 1 emissions propagate away from the injection region in the ionospheric waveguide (Greifinger 1972, Summers & Fraser 1972, Fraser & Summers 1972, Fujita & Tamao 1988). In addition, Fujita & Tamao (1988) predicted that near the injection center the major axis of polarization is perpendicular to the radial direction from the injection region. In the surrounding region, however, the major axis points to the center. Although the polarization angle change shown in Figure 3-7 appears to be somewhat irregular, it shows a general

tendency that the angle changes consistently at a certain time period and a certain frequency range during the propagation. This might imply that the waves were injected near HBA, perhaps near the CHAMP trace between 0840 and 0843 UT (between $L = 2.5$ and 4.4), and propagated in a poleward direction in the waveguide since strongest spectral power was seen at HBA as mentioned earlier and the higher polarization angles (nearly perpendicular to the magnetic meridian) were observed at HBA as suggested by Fujita & Tamao (1988). For example, the polarization angle during the CHAMP overflight is $\sim +75°$ at HBA over the frequency range and becomes less at higher latitudes (particularly at AGO P1) as shown in Figure 3-7. However, it is not clearly known whether the LP waves observed from CHAMP was due to either that the incident Pc 1 waves were originally in the LP mode as they propagate toward the ionosphere (Horne & Thorne 1994, Hu & Denton 2009) or that CHAMP also detected ducting effect of the Pc 1 waves at lower latitudes.

Although it is quite challenging to determine the extent of the injection region with the meridional configuration of the array used in this study, the plasmapause location estimation at $L = 5.8$ in association with the CHAMP observation as discussed earlier supports the idea of the wave injection near or poleward of HBA since possible regions of wave generation and propagation are near or higher L-shells of the plasmapause locations (possibly including detached plasma regions) (e.g., Fraser & Nguyen (2001), Fraser et al. (2005)). Even though the wave injection occurred poleward of HBA, the poleward wave attenuation from HBA to AGO P5 with the signals at HBA being strongest still explains the idea as long as the injection was not far beyond the location of HBA because HBA is located off the meridional line of P2-SPA-P1-P5 and therefore, the wave power attenuated more quickly between HBA and P2 than between the other stations as shown in Figure 3-4.

3.4 Summary

Well-defined ULF Pc 1 pulsations were observed from the Antarctic magnetometer array and the CHAMP satellite, providing a very systematic coverage from the satellite overflight at lower latitude to the ground array covering a very large spatial latitudinal extent, while aligned almost along a magnetic meridian. The observation is unique in that they were acquired at stations distributed over an unprecedented range in geomagnetic latitude ($-62°$ to $-87°$, spanning $\sim$ 2920 km geographically), while positioned approximately along a magnetic meridian and that Antarctica is the only place where such a configuration is possible. The array deployed in the Antarctic terrain also has very significant advantage of minimal geoelectric inhomogeneity. As described in Fraser (1975*b*), polarization observed on the ground may not reflect the true wave properties due to the inhomogeneous ground conductivity. In addition, clearly distinguishable ionospheric sunlight conditions in Antarctica can provide more systematic change of polarization pattern on the ground.

The extent of the ducting is substantial. The spaced magnetometer array with the latitudinally extensive range along a magnetic meridian revealed very efficient wave propagation in the ionospheric waveguide ($\sim$ 8 – 20 dB/1000 km), which has rarely been reported before. Propagation speed and polarization sense and major axis change during the propagation were also shown. These features clearly suggest poleward wave propagation in the ionospheric waveguide.

The Pc 1 pulsations measured by the CHAMP satellite appear to be transverse and nearly LP, which might imply that the wave activity was observed in the wave injection region in the ionosphere. The injection region is also found to have a limited latitudinal extent ($-53°$ to $-61°$ ILAT). The pattern of the polarization sense change was observed on the ground. LHP was dominant at lower latitude and changed to RHP (or LP) during propagation.

The polarization angle pattern change observed from the ground array (e.g., $\sim +75°$ at HBA, being less at higher latitudes) during the CHAMP overflight and the plasmapause location estimation using a model and the CHAMP observations of the wave activity might imply that the waves were injected near HBA, perhaps near the CHAMP trace (between $L = 2.5$ and 4.4), and propagated in a poleward direction in the waveguide. However, a complex polarization pattern (i.e., change in ellipticity and polarization angle) was found on the ground during propagation, which might be attributed to the array being close to the wave injection region where the superposed effect of incident waves and ducted waves is dominant.

Chapter 4

Statistical Study of Pc 1–2 Wave Propagation Characteristics in the High-Latitude Ionospheric Waveguide

4.1 Introduction

Electromagnetic ion cyclotron (EMIC) waves are generally thought to be excited by the cyclotron instability of hot, anisotropic ($T_\perp > T_\parallel$) distribution of medium energy ring current ions in the equatorial region of the magnetosphere in the energy range of $\sim$ 1–100 keV during geomagnetic storms and substorms (Anderson et al. 1996, Kozyra et al. 1997, Jordanova et al. 2001, Thorne et al. 2006). Because EMIC waves induce cyclotron resonance of ring current particles, EMIC waves play an important role in causing rapid particle heating, pitch angle scattering and thus precipitation loss from radiation belts, which are disturbed by geomagnetic storms or substorms, to the ionosphere.

The waves in the ULF range propagate from the magnetosphere toward the Earth in the Alfvén ion cyclotron mode (left-hand polarized, LHP or sometimes linearly polarized, LP)

through field-aligned injection and are reflected back along the lines at the ionosphere (Brice 1965, Cornwall 1965, Kennel & Petschek 1966, Liemohn 1967, Kangas et al. 1998). Some energy of the field-guided signals is transmitted to the ionosphere near or in the auroral zone and couples to right-hand polarized (RHP) compressional (fast), isotropic waves in the ionosphere (Fraser 1975*a*,*b*, Fujita & Tamao 1988). The EMIC waves generated inside the magnetosphere are typically observed as Pc 1 (0.2 – 5.0 Hz) or Pc 2 (0.1 – 0.2 Hz) type pulsations on the ground.

It has long been discussed that there exists the ionospheric waveguide (duct) centered around the Alfvén speed minimum (or electron density maximum) at an altitude of $\sim$ 400 km near the F2 region bounded by the E region ($\sim$ 100 km) and a region where the Alfvén speed increases sharply ($\sim$ 1000 km) to form a resonance cavity for Alfvén waves (see Figure 1-7). Compressional waves, not guided by the magnetic field, propagate horizontally in the waveguide after mode conversion from the incident Alfvén wave to the compressional wave (Manchester 1966, Tepley & Landshoff 1966, Greifinger & Greifinger 1968, Fujita & Tamao 1988). ULF Pc 1–2 waves are the one of the most efficiently propagated MHD waves in the waveguide. Manchester (1966) suggested as the walls of the duct are not perfect reflectors, the the wave is attenuated as it propagates down the duct.

Ground observations by Hayashi et al. (1981) at high latitudes using a search-coil magnetometer array found that ULF Pc 1 waves propagated from an injection region in a concentric pattern of equicontour lines of its intensity and observed an attenuation of 10 dB/100 km near the injection center and 2.5 dB/100 km in the region beyond 500 km from the center using a network of 13 stations spanning 30° in longitude and 15° in latitude (from 53.7°N, 290.9°E to 75.1°N, 328.0°E, CGM). Neudegg et al. (2000) obtained $\sim$ 41 dB/1000 km using a closely-spaced ($\sim$ 150 km) triangular network near Davis, Antarctica (74.6°S, 102.3°E, CGM). The theoterical study by Fujita & Tamao (1988) reported $\sim$ 8 dB/100 km and

the comparison between model and observation by Manchester (1970) estimated $\sim$ 1 – 8 dB/1000 km at low/mid latitudes (note that some studies use "per 100 km" instead of "per 1000 km"). In addition, it has been predicted in theoretical studies that more efficient waveguide propagation occurs at nighttime than daytime as the nighttime boundary provides good reflection (Tepley & Landshoff 1966, Manchester 1966, Greifinger & Greifinger 1968).

Wave polarization is one of the properties that can provide the information about the wave source location and spatial characteristics of wave propagation and media. It has been predicted theoretically that transmitted LHP Alfvén waves, vertically incident on the ionosphere, gradually change to RHP as the wave propagates from the injection region to the surrounding regions in the ionosphere (Baranskiy 1970, Greifinger 1972, Altman & Fijalkow 1980, Fujita & Tamao 1988). Theoretical approaches (e.g., Baranskiy (1970), Greifinger (1972), Summers (1974), Fujita & Tamao (1988)) and ground observations (e.g., Fraser & Summers (1972), Summers & Fraser (1972), Fraser (1975*a*), Fraser (1975*b*), Hayashi et al. (1981),Webster & Fraser (1985)) showed that for horizontally ducted transmissions, ellipticity becomes LP with the major axis of the polarization ellipse pointing toward (or away from) the injection location as well as that the polarization sense changes from predominantly LHP around the injection region to RHP as the distance from the injection region increases, assuming a homogeneous ionosphere and vertical magnetic field lines. Hayashi et al. (1981) reported greater variation of the polarization pattern at high latitudes, suggesting it might be attributed to the array being located close to the wave injection region where the combination of incident waves and ducted waves is more dominant. A theoretical approach by Belova et al. (1997) showed how the polarization pattern on the ground can change in a complex fashion as the inhomogeneity of the ionospheric conductivity varies.

This study describes a statistical analysis of ULF Pc 1–2 wave propagation in the iono-

spheric waveguide observed from a ground-based search-coil magnetometer array in Antarctica, consisting of five stations along the magnetic meridian. Halley Station, located at the lowest latitude among the stations, typically observes well-defined Pc 1–2 wave events with strongest spectral power. The events, showing the identical spectral structure but less wave power, are detected at the other four stations located at higher latitudes. Section 4.2 introduces the ground search-coil magnetometer array instrumentation and data survey for statistical study. Three examples of the Pc 1–2 wave ducting events are presented in Section 4.3 and the statistical study using the ground data obtained in the year 2007 is shown in Section 4.4.

4.2 Data Analysis

4.2.1 Instrumentation

The ground data presented in this study were obtained from the five ULF search-coil magnetometers deployed at Halley Station (HBA), South Pole Station (SPA), and three automated geophysical observatories (AGOs) in Antarctica. They provide three-axis time-varying magnetic field (dB/dt) in local geomagnetic coordinates with X northward, Y eastward, and Z upward parallel to geomagnetic field at a rate of 10 samples/sec (Engebretson et al. 1997). Data from the Z axis are not used in this study since the data from X and Y axis provide sufficient information about the wave power attenuation and polarization during propagation.

The geographic and corrected geomagnetic locations of the ground stations used in this study are presented in Table 3.1. The MLT near the stations is approximately 3 hours behind UT. The Halley Station is at the lowest magnetic latitude and AGO P5 is at the highest magnetic latitude among the stations. This Antarctic ground-based magnetometer array provides observations over an unprecedented latitudinal extent covering geomagnetic

latitudes of $-61.56°$ to $-86.74°$ (over the distance of 2920 km) as shown in Figure 3-1. The three stations P2, SPA and P1 are aligned approximately along a magnetic meridian within 15 min MLT while HBA is somewhat off-meridian (600 km from the meridional line of the three stations). The MLT difference at P5 is not very significant as it is close to the magnetic pole. The latitudes encompass the regions from the subauroral latitude (near HBA) to the cusp (near SPA) and polar cap latitudes (near AGO P5).

4.2.2 Data Survey

This study utilized the data set obtained in the year 2007 from the Antarctic search-coil magnetometer array. Stacked 0 – 1 Hz, 2048-point FFT spectrograms (with Hanning window) of the X (geomagnetic north-south) and Y (geomagnetic east-west) components for all of the stations and for each day in 2007 have been produced and surveyed to identify ULF Pc 1–2 wave activities. Once surveyed, the events are categorized as the "ducting events" if and only if the events occurred at more than 3 stations (out of the five Antarctic stations) with the same duration, frequency bandwidth, and spectral signatures, and with the spectral power attenuating over the latitudinal distance across the network. The attenuation was poleward in most cases.

The time period (start and end time) and frequency bandwidth of each event, which are found simultaneously from the available stations, are specified based on the values obtained from the spectrogram. If the duration of an event is longer than approximately 30 min, the event is split into sub-events, of which the duration exceeds no more than 20 min only for analysis (calculations of attenuation and polarization) purpose. Four frequencies of interest within the frequency bandwidth of each event in both the X and the Y components are also selected to examine whether there is frequency dependence in attenuation and polarization characteristics. Each frequency of interest is defined in this study as a very narrow spectral

signature, of which the bandwidth is center frequency (the selected frequency of interest) ± 0.01 Hz. This corresponds to 5 bins in the 2048-point spectrogram. With the event time periods and frequencies specified, attenuation and polarization parameters for each event period are estimated.

The wave power (in dB) is obtained by multiplying the $\log_{10}$ power in the spectrogram by 10. The wave powers at four selected frequencies during each event period are averaged and line-fitted in a plot of attenuation (dB) versus distance from HBA (km) to estimate attenuation factor (dB/1000 km). The wave powers at each selected frequency are compared to investigate the relationship between wave frequency and attenuation.

In a similar way for the attenuation factor calculation, the polarization parameters (ellipticity and polarization major axis angle) are obtained at four selected frequencies and each station for each event using a polarization analysis technique as described in Fowler et al. (1967) and Rankin & Kurtz (1970) to display ellipticities and polarization major axis angles in terms of frequency versus time. See Appendix A for more details about the polarization analysis technique used in this study. AGO P5 data are not used for the polarization analysis because X-axis data were unavailable during most of the time in 2007.

Ellipticity (ε) is defined as the ratio of the minor axis to the major axis of the ellipse of magnetic field perturbation in the plane perpendicular to background magnetic field. Ellipticity is represented in three ranges: $\varepsilon \geq 0.2$ RHP; $\varepsilon \leq -0.2$ LHP; and $|\varepsilon| < 0.2$ LP as defined in Anderson et al. (1992). Polarization major axis angle (θ, polarization angle in short) is the angle between the major axis of the polarization ellipse and the magnetic meridian in the north-south direction. In the analysis tool used in this study, the polarization angle ranges between $-90°$ and $+90°$. The sign represents the direction of angle with respect to the magnetic meridian in the north-south direction (X component) with positive angle being counterclockwise and negative angle being clockwise.

The dates in the dataset are categorized into three conditions based on the sunlight condition in the ionosphere. The information on the sunlight condition at the low-altitude bound of the E region was obtained via use of an algorithm developed by Muneer (2004) (called *Prog1-7* in the text). It is first necessary to calculate the angle of elevation of the Sun above the horizon, as well as the azimuthal angle that the projection of the Sun's ray makes with north. These values are determined for an altitude of 100 km and allow for identification of the (local) time at which sunrise and sunset occurred for each location. An event was classified as "Sunlit" if its start time was after sunrise and its end time was before sunset for all of the stations. An event was classified as "Dark" if either its start time and end time were earlier than sunrise or if both start and end times were later than sunset for all of the stations. All events that did not fall into one of these three cases were called "Mixed". There are 67 sunlit events, 8 dark events, and 63 mixed events. The insufficient number of the events during dark times is partly (or perhaps completely) due to limited power at the unmanned stations (AGOs) during the winter time.

4.3 Example Events

The data from the Antarctic magnetometer array has been showing very well-defined ULF wave ducting events over the entire extent of the array. This section presents three example events showing Pc 1–2 wave propagation in the ionospheric waveguide. Each example is presented with four figures, which include spectrograms, power spectra and attenuation plots, polarization ellipticity patterns, and polarization angle patterns. In the 0 – 1 Hz Fourier spectrograms, the five stations are shown in the order of latitude, the station at the highest latitude being on the top (P5) and the station at the lowest latitude being on the bottom (HBA). The power spectra display $\log_{10}$ power as a function of frequency. The attenuation plots show the wave power attenuation (in dB) over the distance from HBA (in

km) at four selected frequencies.

The two polarization parameters (ellipticity and polarization angle) are also displayed for each example event. The figures for the polarization ellipticity (ε) patterns show the ellipticities in a color scale over the course of the event duration in terms of frequency for each station, containing 12 panels: 3 polarization modes (LP, LHP, and RHP) for each station. The top 3 panels represent the data from P1 and the bottom 3 panels the lowest latitude station, HBA (P5 data are not used for polarization analysis due to the unavailable X component data). The color scale represents LH circular polarization as -1 (negative ellipticity) and RH circular polarization as $+1$ (positive ellipticity). LP is defined as having $|\varepsilon| < 0.2$ as mentioned earlier.

The figures for the polarization angle (θ) patterns show the polarization angles in a color scale over the course of the event duration in terms of frequency for each station, containing 8 panels: positive ($\theta \geq 0$) and negative ($\theta < 0$) angles for each station, P1 being on the top 2 panels and HBA being on the bottom 2 panels. Ellipticities/angles are displayed only for those frequencies which exceed a certain power threshold appropriate to the digitization level of the instrument range. Each horizontal pixel corresponds to an average of 2048-point Fourier power spectra.

4.3.1 Example 1: Mar. 5, 2007

The event occurred on Mar. 5, 2007 approximately from 0200 to 0600 UT over the broad-band frequency range 0.4 to 0.8 Hz (Pc 1 range) as shown in the stacked spectrograms of the Y components in Figure 4-1. The poleward propagation across the entire network (from HBA to P5) is apparent and both overall and detailed (pearls) spectral structures remain constant during the propagation. The identical spectral patterns, albeit attenuated across the network, suggest that the waves were generated in a localized region within the

ionosphere. Otherwise, such identical spectral signatures may not be detected over the wide range. During this event, the ionosphere at an altitude of 100 km over all of the stations was sunlit.

Figure 4-2 shows the power spectra ($\log_{10}$ power versus frequency) of the ULF Pc 1 events and the wave power attenuation (in dB) over the distance from HBA (in km) at four selected frequencies (0.55, 0.62, 0.69, and 0.76 Hz). Two different time periods are examined for this analysis in an attempt to separate such a long event duration (0220 to 0240 UT and 0240 to 0300 UT). Each time period displays the results from both X and Y components. The power spectra also clearly reveal that the spectral structures remain almost identical during the propagation. From the results in Figure 4-2, the attenuation factors appear to be approximately between 10 and 16 dB/1000 km ($\sim$ 14 dB/1000 km on average) depending on the wave frequency. Although not very significant, the attenuation appears to increase as the wave frequency increases, as predicted by Greifinger & Greifinger (1968).

Polarization ellipticity patterns shown in Figure 4-3 suggest that both LHP and RHP modes are predominantly shown at HBA although the modes appear during different times and over different frequency ranges. The event from 0315 to 0530 UT over the frequency range 0.4 to 0.7 Hz is in LHP mode but the event during the same period over the upper frequency range (0.7 to 0.8 Hz) is in RHP mode. The event occurring from 0215 to 0315 UT over the frequency range 0.5 to 0.8 Hz is also in RHP mode. The polarization sense change is somewhat clear during the poleward propagation. For example, the LHP mode event at HBA changes to an event in either LP or RHP mode at the higher latitudes while the RHP mode event at HBA changes to the LP or LHP mode events. Although the pattern of the polarization ellipticity appears to be complex over the temporal and spatial extent, one thing that seems to be shown clearly is that the ratio between the modes varies over

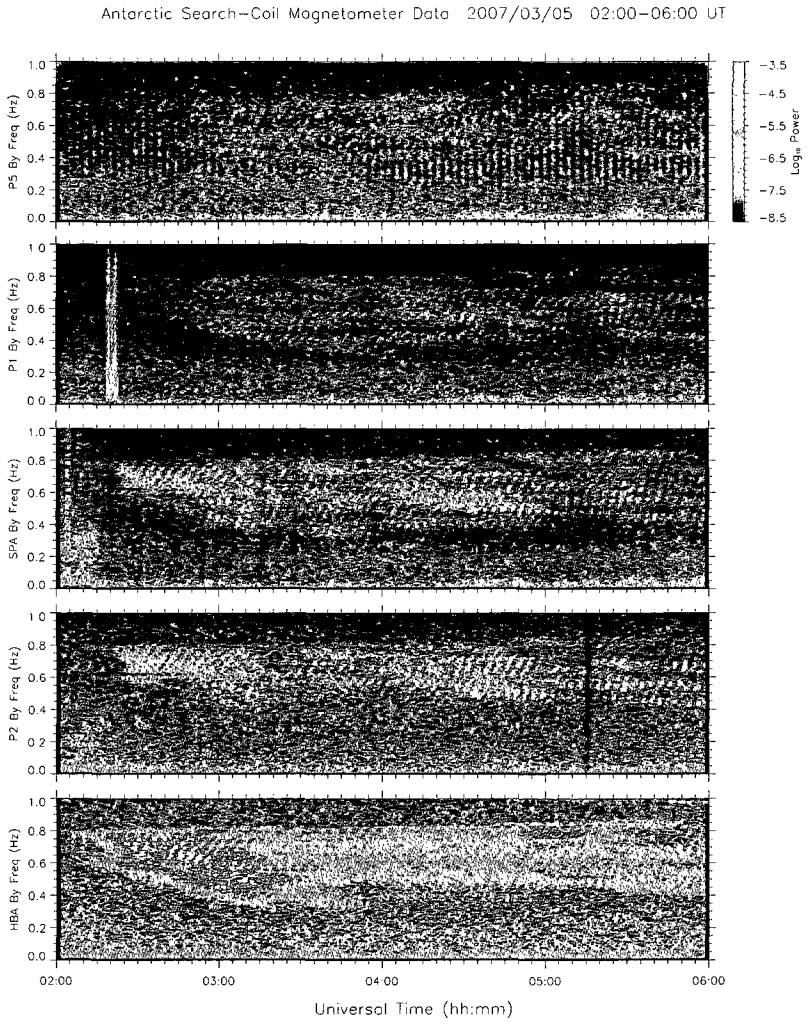

Figure 4-1: Stacked 0 – 1 Hz Fourier spectrograms in the Y (east-west) components of the search-coil data showing the ULF Pc 1 waves recorded at the Antarctic stations, Halley (HBA), AGO P2, South Pole (SPA), P1 and P5 from 0200 to 0600 UT on Mar. 5, 2007 (Example 1).

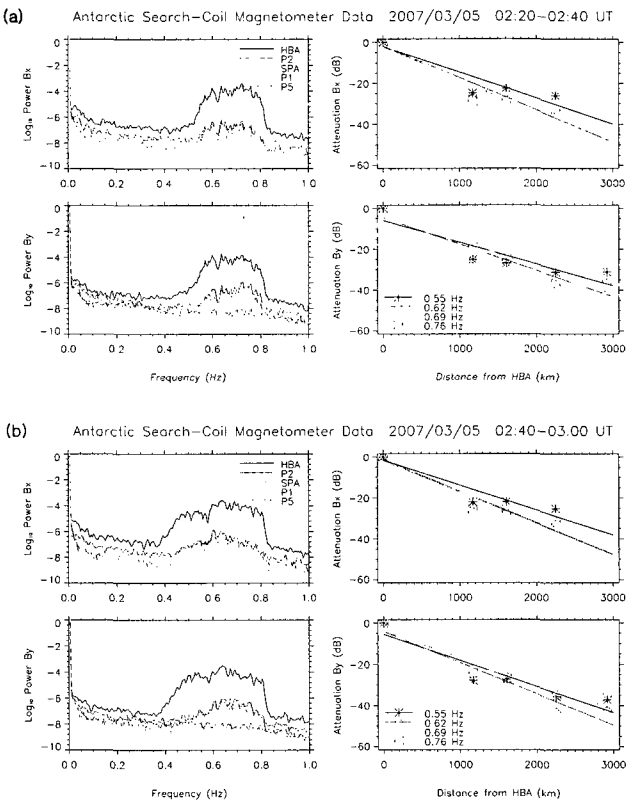

Figure 4-2: Power spectra ($\log_{10}$ power versus frequency) of the ULF Pc 1 events observed by the Antarctic search-coil array and the wave power attenuation (in dB) over the distance from HBA (in km) at four selected frequencies (0.55, 0.62, 0.69, and 0.76 Hz) during the two time periods, (a) 0220 – 0240 UT and (b) 0240 – 0300 UT on Mar. 5, 2007. The graphs for each time period display the results from both X and Y components.

distance. As mentioned earlier, the waves seen from HBA are predominantly in LHP and RHP modes but LP mode shows up more dominantly at P1.

The polarization angle patterns in Figure 4-4 appear to show similar temporal structures, as shown in the ellipticity pattern in Figure 4-3, at least at HBA. In other words, the temporal distribution of the positive angles at HBA shows a similar pattern to that of the ellipticities at HBA, which might indicate that the wave events in each polarization mode are propagated from each different localized injection region. This scenario is supported by Greifinger (1972), Summers & Fraser (1972), Fraser & Summers (1972), and Fujita & Tamao

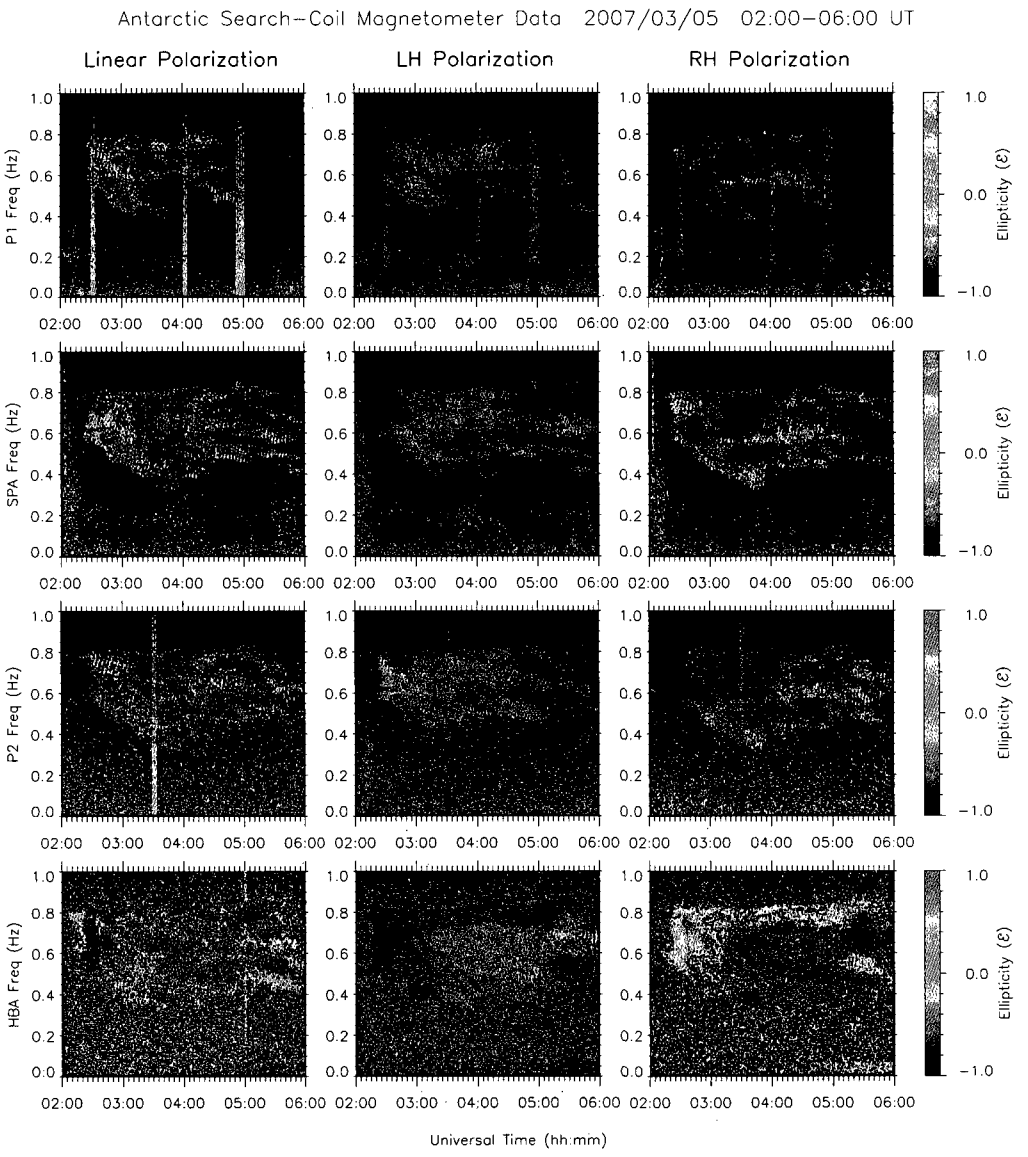

Figure 4-3: Polarization ellipticity (ε) of the ULF Pc 1 waves observed by the Antarctic search-coil array on Mar. 5, 2007 in a plot of frequency versus time. Each panel is represented in a color scale with -1 being LH circular polarization (negative ellipticity) and $+1$ being RH circular polarization (positive ellipticity). LP is defined as having $|\varepsilon| < 0.2$.

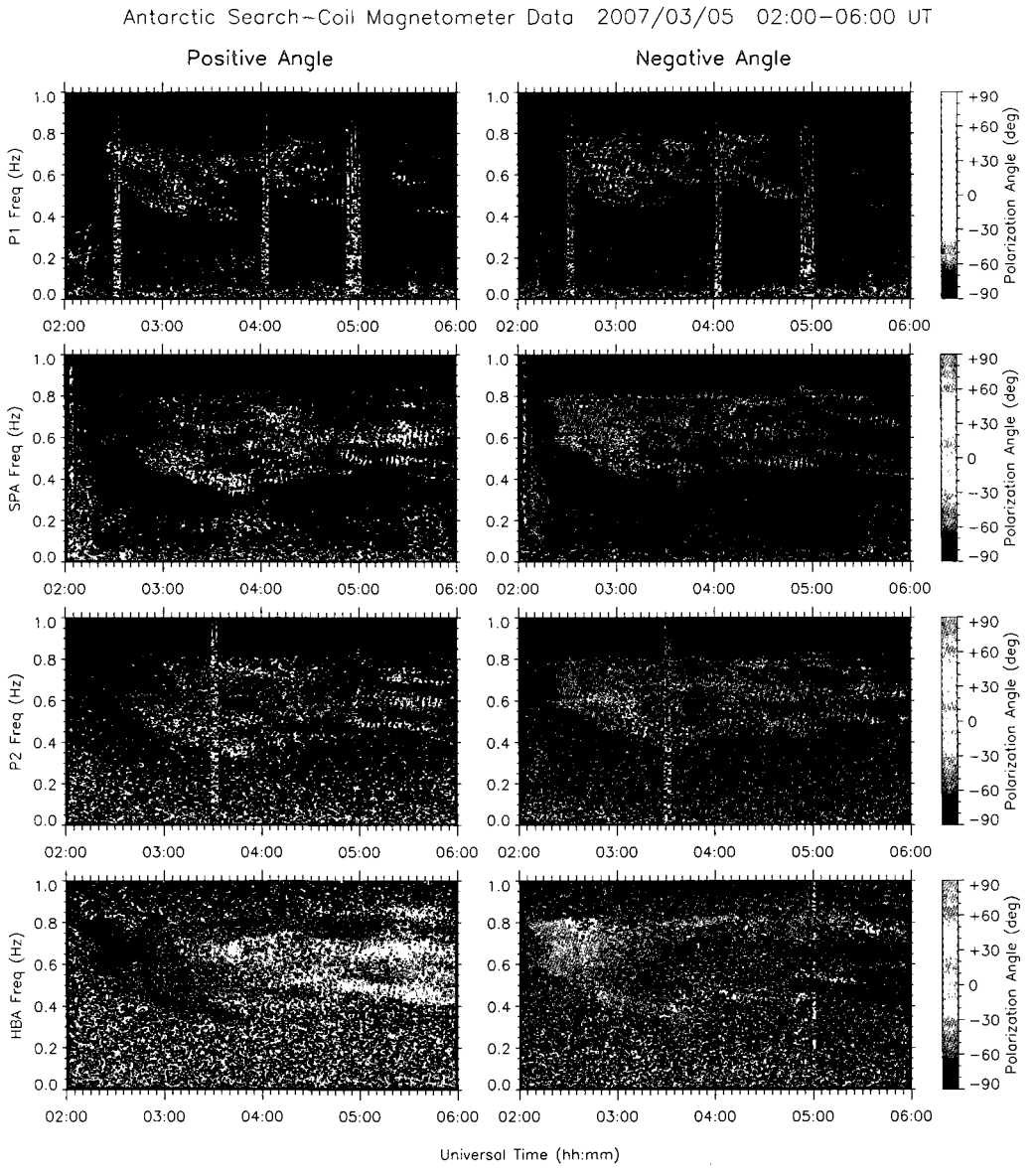

Figure 4-4: Polarization angle (θ) of the ULF Pc 1 waves observed by the Antarctic search-coil array on Mar. 5, 2007 in a plot of frequency versus time. The angle ranges between $-90°$ and $+90°$. The sign represents the direction of angle with respect to the magnetic meridian in north-south direction (X component) with positive angle being counterclockwise and negative angle being clockwise. The panels on the left and right present positive ($\theta \geq 0$) and negative ($\theta < 0$) angles, respectively.

(1988), who suggested, given certain assumptions, that the polarization ellipse observed on the ground becomes increasingly LP with the major axis pointing toward (or away from) the wave injection region as Pc 1 emissions propagate away from the injection region in the ionospheric waveguide.

4.3.2 Example 2: Mar. 24, 2007

The Pc 1 wave event was observed from 1900 to 2130 UT on Mar. 24, 2007 as shown in the stacked spectrograms of the X components in Figure 4-5. Although the overall wave activity occurred over a broad bandwidth ($\sim$ 0.25 to 0.4 Hz), the detailed structure displays narrowband events (at around 0.3 and 0.4 Hz). Data from P5 were unavailable. Pearl structure is also shown in the spectrograms. During this event, the ionosphere at an altitude of 100 km over all of the stations was sunlit.

The power spectra and the wave power attenuation (in dB) over the distance from HBA (in km) at four selected frequencies (0.27, 0.31, 0.35, and 0.39 Hz) are shown in Figure 4-6. Two different time periods are examined for this analysis in an attempt to separate such a long event duration (2010 to 2030 UT and 2100 to 2120 UT). Each time period displays the results from both X and Y components. Surprisingly identical spectral signatures are found in the power spectra in both components for each time period. From the results in Figure 4-6, the attenuation factors appear to be approximately between 7 and 14 dB/1000 km ($\sim$ 10 dB/1000 km on average) depending on the wave frequency. No clear tendency in the relationship between the attenuation and the frequency is found from the results in Figure 4-6.

Unlike the patterns as shown in Figure 4-3, the polarization ellipticity patterns in Figure 4-7 show very consistent ellipticity over a certain frequency range over the course of the event duration at all of the stations. In other words, the events occurred over the higher

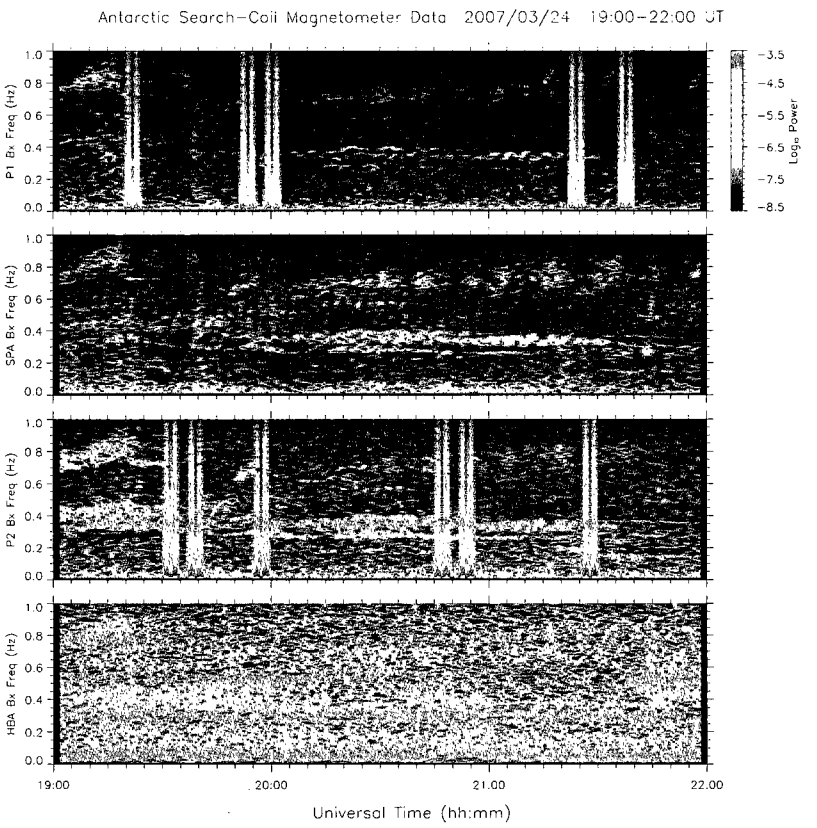

Figure 4-5: Stacked 0 – 1 Hz Fourier spectrograms in the X (north-south) components of the search-coil data showing the ULF Pc 1 waves recorded at the Antarctic stations, Halley (HBA), AGO P2, South Pole (SPA), and P1 from 1900 to 2130 UT on Mar. 24, 2007 (Example 2).

($\sim$ 0.35 to 0.40 Hz), mid ($\sim$ 0.30 to 0.35 Hz), and lower ($\sim$ 0.25 to 0.30 Hz) frequency range consistently show LP, RHP, and LHP, respectively. While LP and RHP modes lose their power during the poleward propagation, the LHP mode events intensify at mid latitudes. The polarization angle patterns in Figure 4-8 show that the positive angles are more dominant than the negative angles at HBA and this tendency appears to remain the same at the higher latitudes. Again, the polarization patterns in this example might indicate that the wave events in each polarization mode are propagated from each different localized injection region.

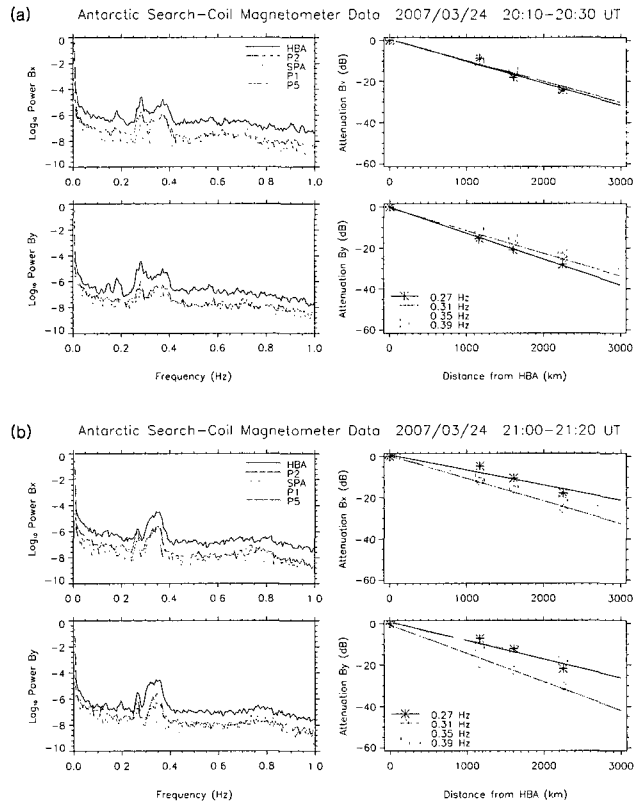

Figure 4-6: Power spectra ($\log_{10}$ power versus frequency) of the ULF Pc 1 events observed by the Antarctic search-coil array and the wave power attenuation (in dB) over the distance from HBA (in km) at four selected frequencies (0.27, 0.31, 0.35, and 0.39 Hz) during the two time periods, (a) 2010 – 2030 UT and (b) 2100 – 2120 UT on Mar. 24, 2007. The graphs for each time period display the results from both X and Y components.

4.3.3 Example 3: Oct. 7, 2007

This example displays very well-defined pearl structure in the Pc 1 range ($\sim$ 0.30 to 0.50 Hz) from 0420 to 0640 UT on Oct. 7, 2007. The stacked spectrograms in Figure 4-9 show the X component of this event. Data from P5 were unavailable. During this event, the ionosphere at an altitude of 100 km over all of the stations was sunlit.

As shown in the previous examples, very similar spectral signatures are found in the power spectra in both components for each time period: 0440 to 0500 UT and 0600 to 0620 UT (Figure 4-10). The wave power attenuation (in dB) over the distance (in

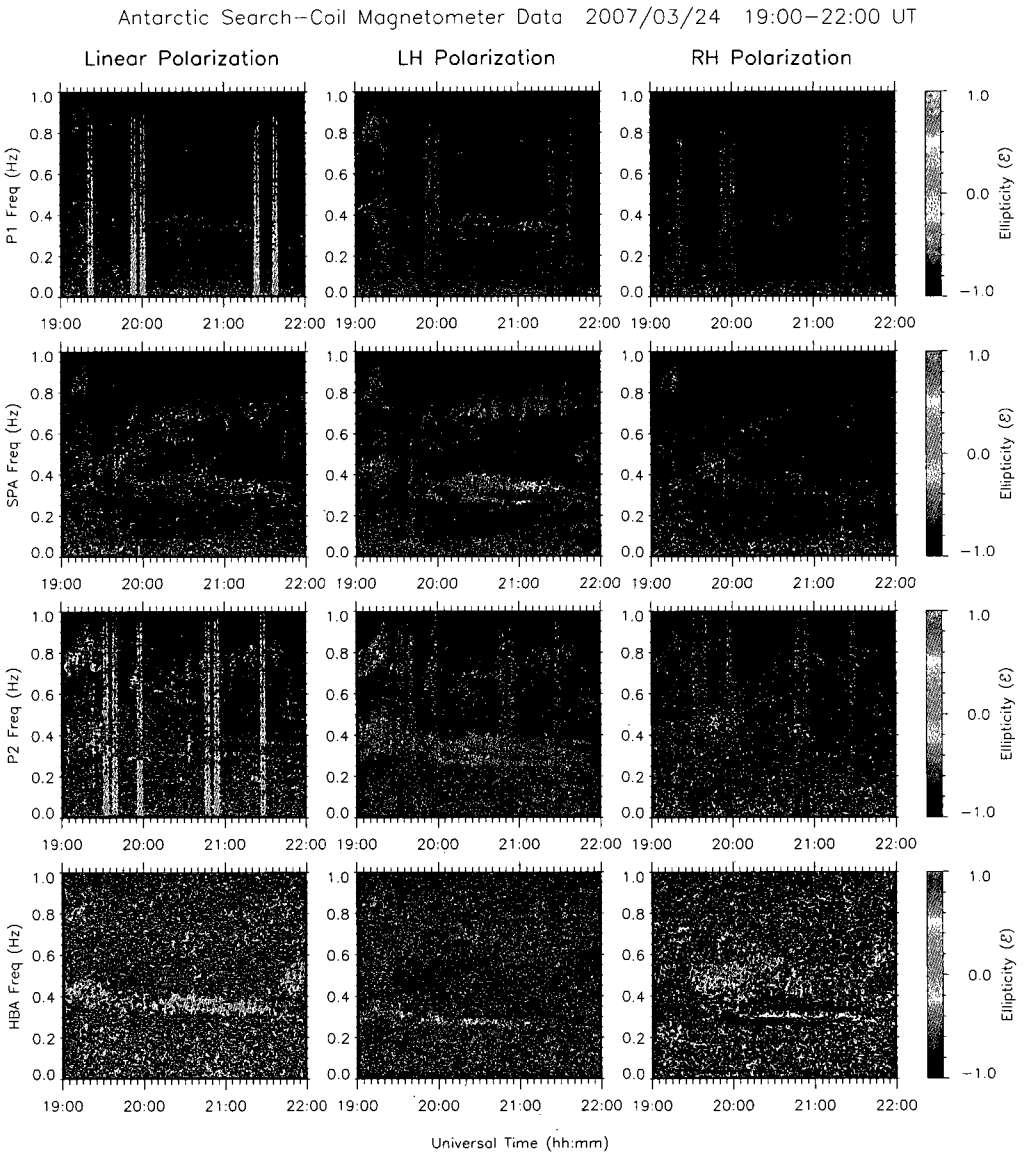

Figure 4-7: Polarization ellipticity (ε) of the ULF Pc 1 waves observed by the Antarctic search-coil array on Mar. 24, 2007 in a plot of frequency versus time. Each panel is represented in a color scale with -1 being LH circular polarization (negative ellipticity) and $+1$ being RH circular polarization (positive ellipticity). LP is defined as having $|\varepsilon| < 0.2$.

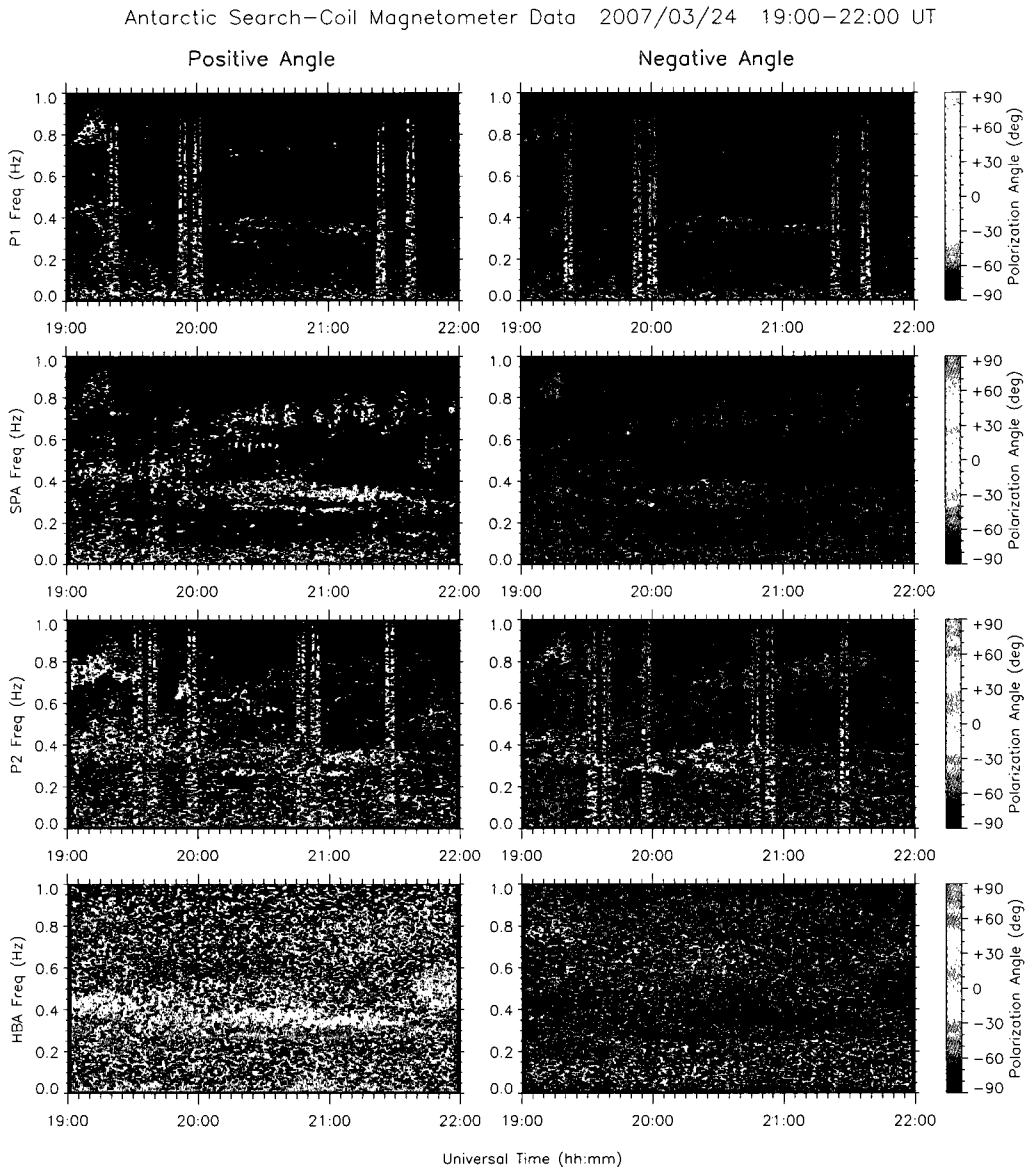

Figure 4-8: Polarization angle (θ) of the ULF Pc 1 waves observed by the Antarctic search-coil array on Mar. 24, 2007 in a plot of frequency versus time. The angle ranges between $-90°$ and $+90°$. The sign represents the direction of angle with respect to the magnetic meridian in north-south direction (X component) with positive angle being counterclockwise and negative angle being clockwise. The panels on the left and right present positive ($\theta \geq 0$) and negative ($\theta < 0$) angles, respectively.

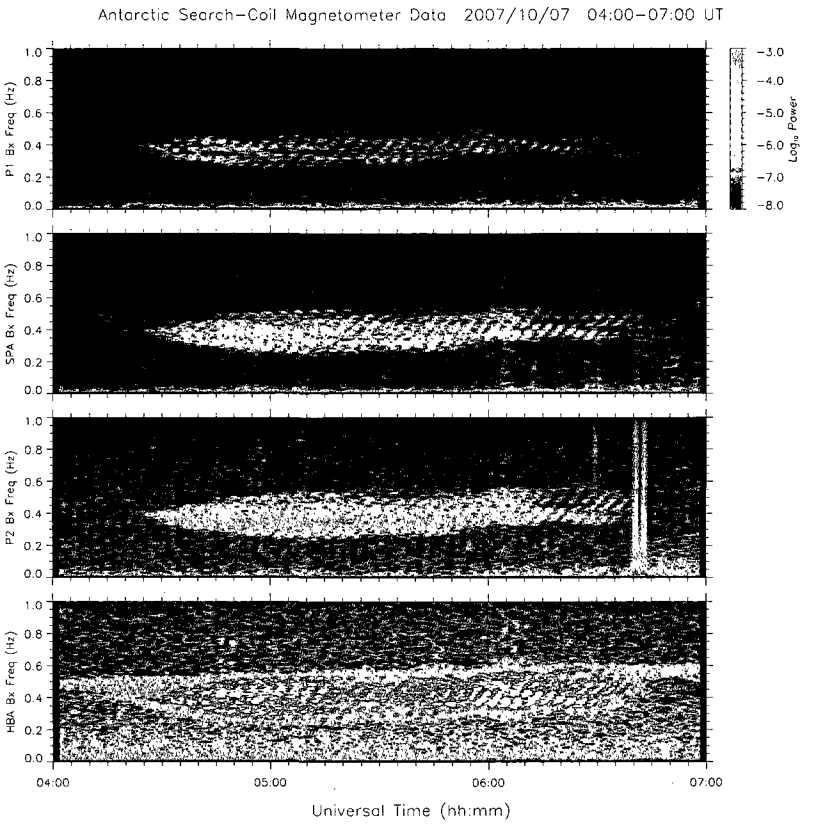

Figure 4-9: Stacked 0 - 1 Hz Fourier spectrograms in the X (north-south) components of the search-coil data showing the ULF Pc 1 waves recorded at the Antarctic stations, Halley (HBA), AGO P2, South Pole (SPA), and P1 from 0420 to 0640 UT on Oct. 7, 2007 (Example 3).

km) at four selected frequencies (0.30, 0.38, 0.46, and 0.54 Hz) as shown in Figure 4-10 reveal that the attenuation factors are approximately between 11 and 29 dB/1000 km ($\sim$ 20 dB/1000 km on average) depending on the wave frequency. As also previously shown, the attenuation factor tends to increase with frequency except for the highest frequency of 0.54 Hz, at which the spectral power is too attenuated even at P2 to be included in the analysis.

The ellipticity patterns in Figure 4-11 show that the event is in a complex mode at HBA but at the higher latitudes, LP and RHP modes are predominantly displayed in a clear

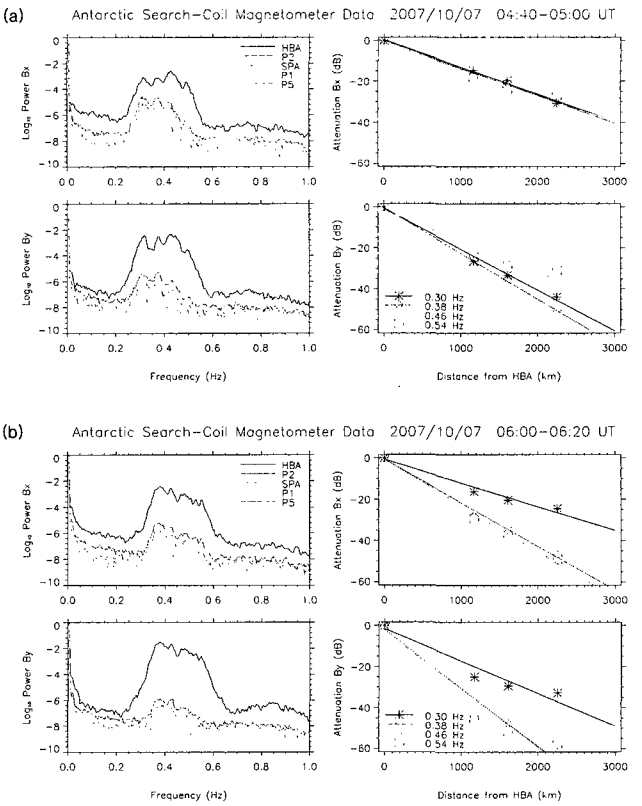

Figure 4-10: Power spectra ($\log_{10}$ power versus frequency) of the ULF Pc 1 events observed by the Antarctic search-coil array and the wave power attenuation (in dB) over the distance from HBA (in km) at four selected frequencies (0.30, 0.38, 0.46, and 0.54 Hz) during the two time periods, (a) 0440 – 0500 UT and (b) 0600 – 0620 UT on Oct. 7, 2007. The graphs for each time period display the results from both X and Y components.

fashion during the event period and over the event bandwidth. This tendency is similarly shown in all of the three examples, which might imply that the events observed at HBA are dominated by both incident and ducted waves while the events at the higher latitudes are mostly ducted. The polarization angle patterns in Figure 4-12 show a similar tendency to the ellipticity patterns of this event, displaying somewhat complex angle patterns at HBA but less complexity at the higher latitudes. Both positive and negative angles are shown almost equally in the events at the higher latitudes.

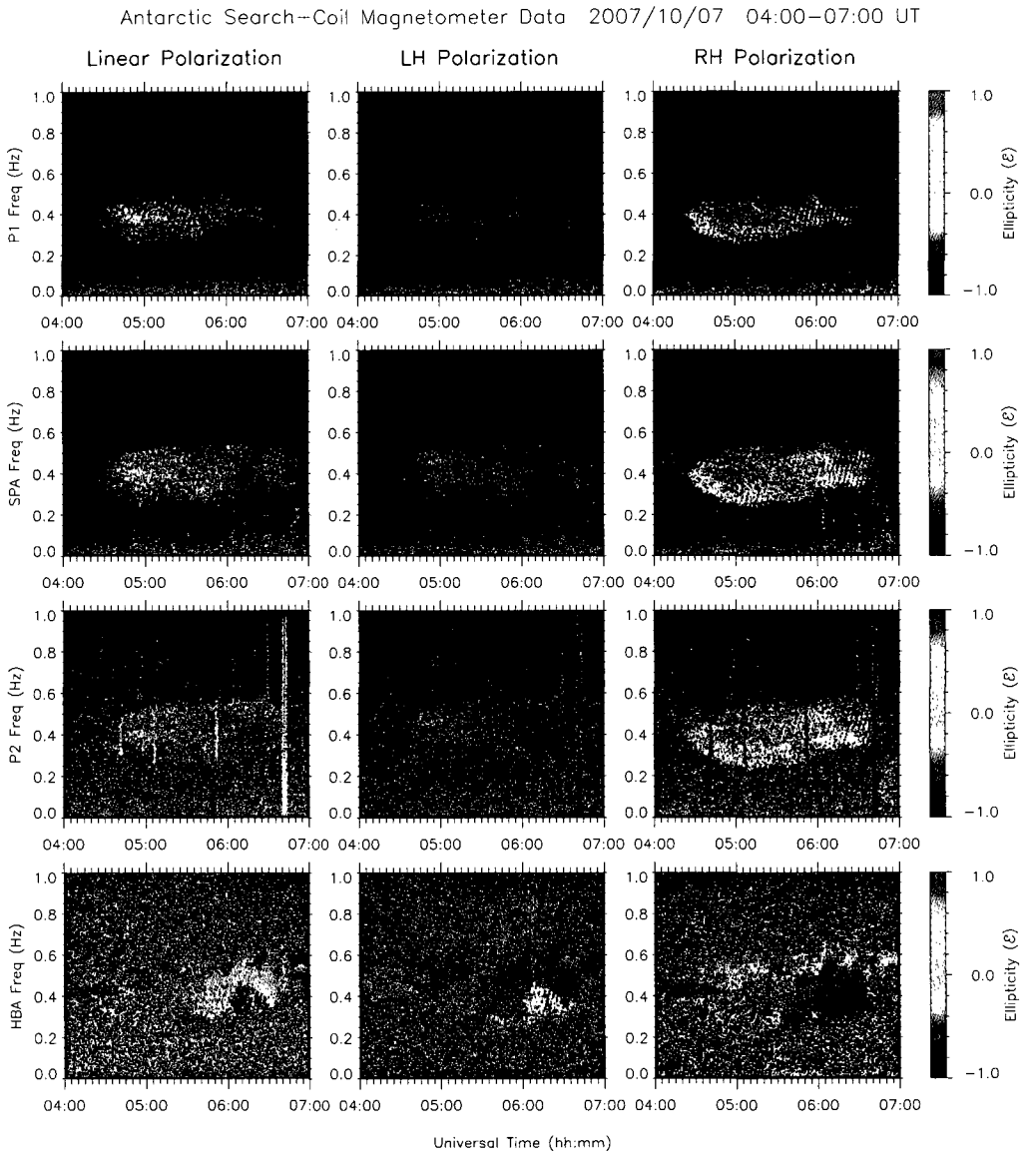

Figure 4-11: Polarization ellipticity (ε) of the ULF Pc 1 waves observed by the Antarctic search-coil array on Oct. 7, 2007 in a plot of frequency versus time. Each panel is represented in a color scale with -1 being LH circular polarization (negative ellipticity) and $+1$ being RH circular polarization (positive ellipticity). LP is defined as having $|\varepsilon| < 0.2$.

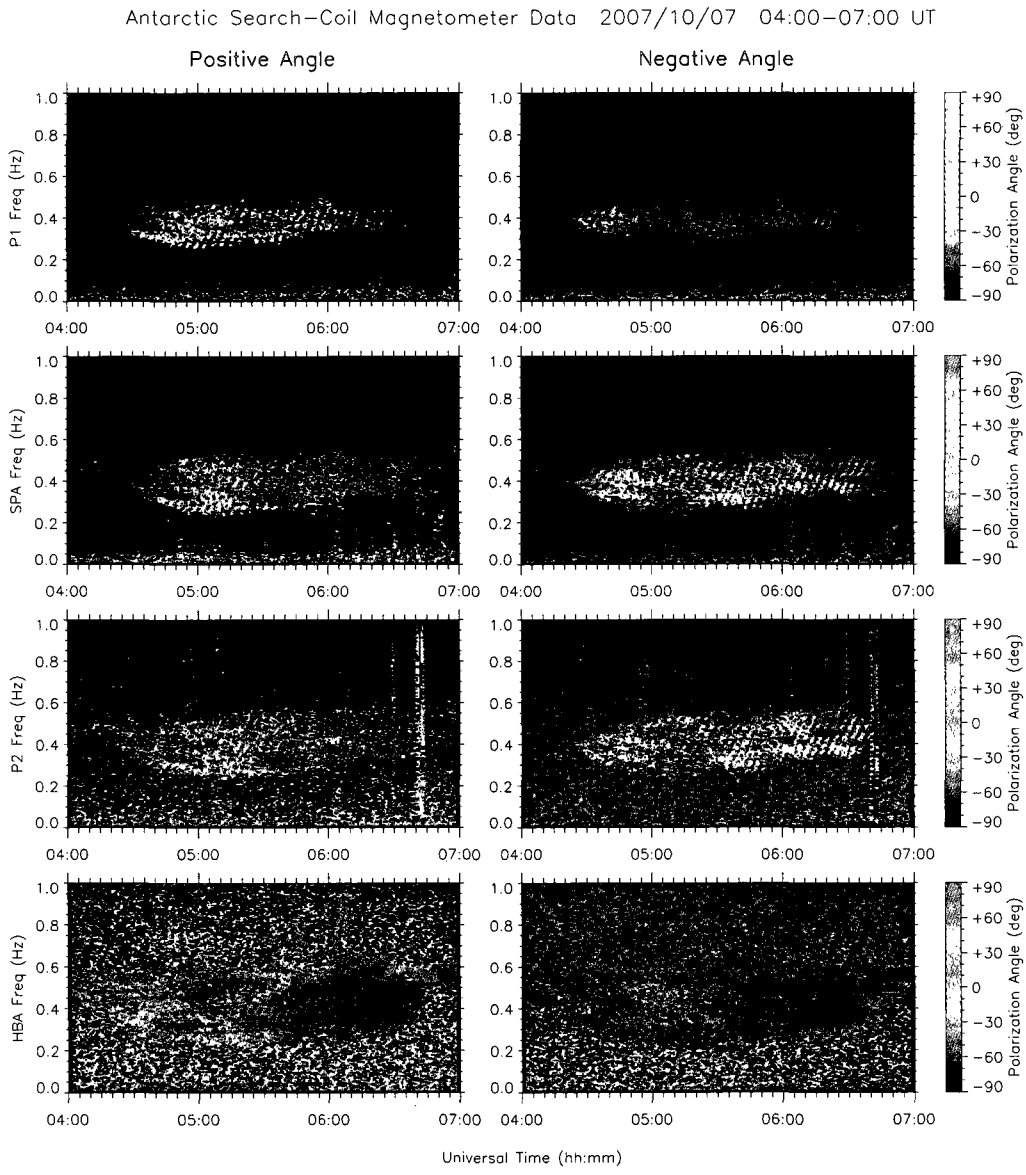

Figure 4-12: Polarization angle (θ) of the ULF Pc 1 waves observed by the Antarctic search-coil array on Oct. 7, 2007 in a plot of frequency versus time. The angle ranges between $-90°$ and $+90°$. The sign represents the direction of angle with respect to the magnetic meridian in north-south direction (X component) with positive angle being counterclockwise and negative angle being clockwise. The panels on the left and right present positive ($\theta \geq 0$) and negative ($\theta < 0$) angles, respectively.

4.4 Statistical Results

A total of 138 ULF Pc 1–2 wave events showing poleward propagation in the ionospheric waveguide are found from the Antarctic search-coil magnetometer array data in 2007. Out of the 138 events, 95 events are structured pulsations (pearls). Bandwidths of the events in this study are classified as "broadband" and "narrowband". Although there is no generally accepted definition for the classification used in other studies, this study classifies the bandwidth as narrowband if the bandwidth is < 0.1 Hz, otherwise, broadband. Out of the total events, 37 events are classified as narrowband waves.

There are 20 events that are not clearly propagating poleward, meaning the most dominant spectral power shows up somewhere other than the lowest latitude (HBA). Instead, either SPA or P2 displays the most dominant spectral power. This type of irregular propagation occurred mostly under sunlit conditions.

4.4.1 MLT Occurrences

MLT occurrences of Pc 1–2 wave ducting events are shown for the entire set of events in 2007 (Figure 4-13) and for the events classified according to the their propagation types (Figure 4-14). Figure 4-13 shows that the Pc 1–2 ducting occurred at all local times, but was more common during daytime hours and showed peaks near 0700 MLT and 1400 MLT.

While a Pc 1–2 wave occurrence peak was found in the early afternoon sector using a ground network (Popecki et al. 1993) and satellite measurements (Fraser & McPherron 1982), some studies observed two occurrence peaks. Satellite observations of Pc 1–2 waves by Anderson et al. (1992) found that an occurrence peak was found at 1100 to 1500 MLT at $L = 3.5$ to 9, indicating that plasma sheet protons in the partial ring current as well as protons on closed drift paths are important for generating EMIC waves. They also found a secondary peak in the dawn sector (0300 to 0900 MLT) at $L > 7$. Bolshakova et al.

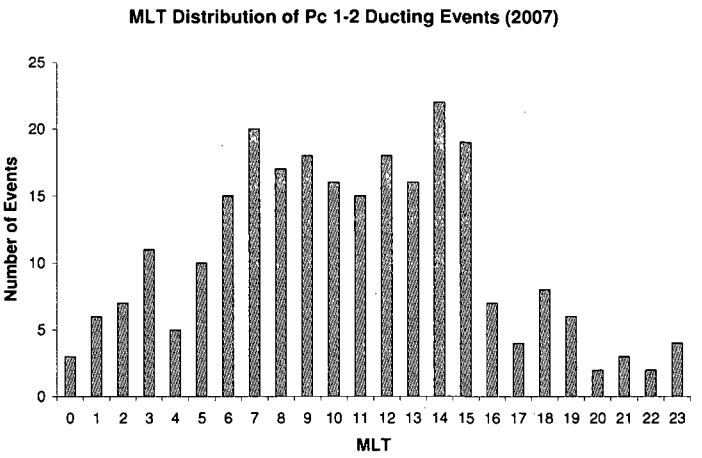

Figure 4-13: MLT distribution of ULF Pc 1–2 ducting events in the year 2007.

(1980) used 7 ground magnetometers to suggest that occurrence depends significantly on geomagnetic latitude. According to their study, one maximum has been found around noon from two stations at higher latitudes (77° and 85°). Two maxima appeared at mid latitudes (74° and 75°): one approximately at 0800-0900 MLT and the other at around 1500 MLT. Stations located in the auroral zone (63° and 64°) also show two maxima but at significantly different times: a peak at 1600–1700 MLT and a secondary peak in the early morning sector. Bolshakova et al. (1980) suggest the existence of the two occurrence peaks is attributed to the position of the stations with respect to the dayside polar cusp since the stations approach the cusp twice in the course of their diurnal rotation. The MLT occurrences observed by Plyasova-Bakounina et al. (1996) using a ground network of six stations at latitudes 65° to 76° appear to be similar to those in the Bolshakova et al. (1980) study. Although the MLT occurrences in Figure 4-13 appear to agree with the previous results, the implication might be somewhat different because the result in Figure 4-13 contains all the MLT occurrences of the ducting events over the entire latitudinal extent while the previous studies show occurrences from each station.

As mentioned earlier, there are 20 events that are categorized as "irregular propagation", in which the most dominant spectral power shows up somewhere other than the lowest latitude (HBA). This might imply a higher-latitude or off-meridional (from the meridional line of P2-SPA-P1-P5) wave injection. Figure 4-14 displays the MLT occurrence difference between the regular poleward propagation and the irregular propagation. It is noted that the irregular propagation events are rather clustered in the prenoon and the postnoon sectors and occurred mostly under sunlit condition. Figure 4-15 shows the normalized occurrences of the frequency components of the two different propagation types - "Clear Poleward", and "Irregular Propagation", in which the propagation types - or perhaps, where the injection region is relatively located - are related with the wave frequency components in the waveguide. A similar tendency is also demonstrated in Figure 4-17 in Section 4.4.2, which reveals that the frequency components in the waveguide are dependent on the ionospheric conductivity and the occurrences of the frequency range under sunlit conditions show a similar pattern to what is shown in Figure 4-15. This relationship might indicate that wave injection is affected by geomagnetic activity (or at least the geometry of the field lines along which waves are injected) because the wave frequency components appear to be related with the ionospheric conductivity which also varies with the geomagnetic activity. Another possible explanation as to the irregular propagation might be that the waveguide lower boundary has varying transmission coefficients, so the wave does not necessarily have less amplitude on the ground at successive stations along the direction of propagation (Neudegg et al. 2000).

4.4.2 Spectral Power Attenuation and Ionospheric Conductivity

The average spectral power attenuation factors under the three different sunlight conditions are estimated by averaging the attenuation factors of the X and Y components

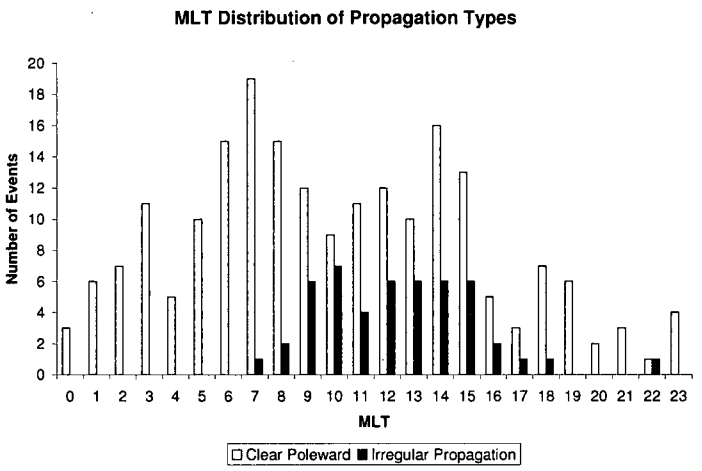

Figure 4-14: MLT distribution of ULF Pc 1–2 ducting events - clear poleward propagation versus irregular propagation.

over the bandwidth (at four selected frequencies) of each event. The survey estimated $\sim$ 9.85 dB/1000 km (standard deviation, $\sigma = 6.55$) under sunlit conditions, $\sim$ 12.33 dB/1000 km ($\sigma = 4.61$) under mixed conditions, and $\sim$ 13.81 dB/1000 km ($\sigma = 7.08$) under dark conditions, giving an total average (over the entire year) of $\sim$ 11.10 dB/1000 km ($\sigma = 5.93$). The attenuation shows a seasonal effect, sunlit-time attenuation being lower, dark-time attenuation being higher, and mixed-time being in the middle.

The attenuation results from the model/observation studies including the ones in this study reveal a wide range of the attenuation factors. Moreover, the attenuation factors obtained in this study appear to be much lower than those in many other previous studies as listed in Section 4.1. The wide range of the results seem to be attributed to ionospheric conductivity in the waveguide, which varies with sunlight. In addition, attenuation in the waveguide may not occur in a linear fashion due to its inhomogeneous conductivity and the leaky ionospheric layer (Manchester 1968, Neudegg et al. 2000, Fraser & Nguyen 2001). It can also be attributed to the different configuration of the arrays in latitudinal and longitudinal extent in other studies since ducting can occur most efficiently along the

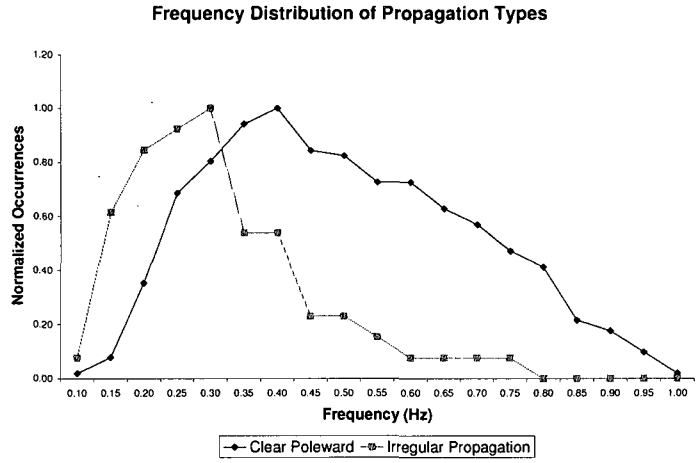

Figure 4-15: Frequency distribution of two different Pc 1–2 wave propagation types - clear poleward propagation versus irregular propagation. Note that the occurrences of each propagation type are normalized.

magnetic meridian (Greifinger & Greifinger 1973, Fraser 1975*a*). Fraser & Nguyen (2001) suggests that signals may not fall off monotonically with distance in the presence of spatial variations in density in the E region in the ionosphere. In addition, Hayashi et al. (1981) observed both poleward and equatorward attenuation and concluded that poleward propagation shows slightly less attenuation. The more efficient poleward than equatorward ducting might be attributed to incident Poynting flux being initially poleward based on the fact that the incident waves are field-aligned Alfvén waves (field lines are angled pointing toward the Poles). The observations in this statistical study, showing much less attenuation compared to the other previous observations, are unique in that the ducted waves, seen over an array with unprecedented geomagnetic latitudinal range and positioning along a magnetic meridian (a condition that provides the most efficient ducting), have rarely been measured before.

The result in this study that sunlit-time propagation is more efficient than dark-time (or mixed-time) propagation is opposite to the ones in the model studies (e.g., Tepley

& Landshoff (1966), Manchester (1966), Greifinger & Greifinger (1968), Lysak (2004)) in which less attenuation was found in dark-time propagation than sunlit-time propagation. It has been suggested that the less attenuation under dark conditions is attributed to higher reflection coefficients at both the upper and lower boundaries of the waveguide (e.g., Manchester (1966)) and less collisions in plasma, equivalently, longer plasma skin depth ($\propto 1/\omega_{pe}$) (e.g., Greifinger & Greifinger (1968)). Lysak (2004) concluded that since ducted signals are responsive to the vertical magnetic field caused by the curl of the horizontal electric fields (Faraday's law), implying that in the weak electric fields (at high conductivity) the magnetic fields seen on the ground are weak accordingly. Manchester & Fraser (1970) showed the difference of Pc 1 wave occurrences between two mid-latitude stations and found that more simultaneous events are observed near 0500 MLT than in midday-afternoon hours when the ionospheric electron density was higher. However, no observational statistical study of the variation of attenuation factors under different sunlight conditions has been completed before.

The contrasting results in this study might suggest that the wave attenuation in the ionospheric waveguide is governed by the Hall current induced by the incident Alfvén wave more than by collisional processes in the ionospheric plasma. Sunlit conditions cause higher Hall conductivity (equivalently, lower electric field intensity) in the ionosphere. Unlike the model predictions by the previous studies commented above, in which the higher conductivity leads to higher attenuation due to either higher collision plasma frequency or lower induced magnetic field, the results in this study might suggest that the increased Hall current due to increased conductivity under sunlit conditions results in lower attenuation assuming ducted waves propagating in the waveguide are induced by the Hall currents as predicted by Fujita & Tamao (1988).

Fujita & Tamao (1988) commented that the Pedersen and Hall currents are generated

in the E region by the incident Alfvén waves, which contribute to the generation of the fast mode waves. The Hall currents induce ducted fast waves propagating horizontally in the waveguide. Since the electrostatic electric field of the incident Alfvén waves is dominant in power, the Hall current generates ground magnetic fields, which are detected by ground search-coil magnetometers, near the region where the Alfvén waves are injected. They also mentioned that, on the other hand, in the region surrounding the injection region both the fast waves trapped in the duct and the fields induced by Pedersen currents perturb the magnetic field on the ground since the signal intensity of the fast waves is larger than that of the incident Alfvén waves. Fujita (1988) suggested ionospheric Joule loss is the most effective mechanism of wave attenuation in the waveguide and energy loss of the fast wave by Pedersen current is dominant.

The spectral power attenuation of the ducting events as a function of frequency under the three ionospheric sunlight conditions is shown in Figure 4-16, indicating wave power attenuation appears to increase with increasing frequency. This result is supported by a model predicted by Greifinger & Greifinger (1968), who suggest that attenuation in any band generally increases with frequency, being smallest at the cutoff frequency since signals are attenuated due to collisional process (signals with higher frequencies undergo more collisions). Fujita (1988) explained that the attenuation decreases at the lower frequency because the ducted wave with a lower frequency has a longer vertical wavelength. Fujita (1988) also mentioned that at a lower frequency, because of the longer vertical wavelength and wave reflection at the surface of the Earth, the electric field disturbance of the ducted wave has its maximum value at the higher altitude where the conductivity is smaller.

The statistical survey of the frequency components of the Pc 1–2 ducting events is shown in Figure 4-17. This result clearly shows the frequency of the ducting events decreases with the increasing ionospheric conductivity. In other words, the frequency cutoff defined by

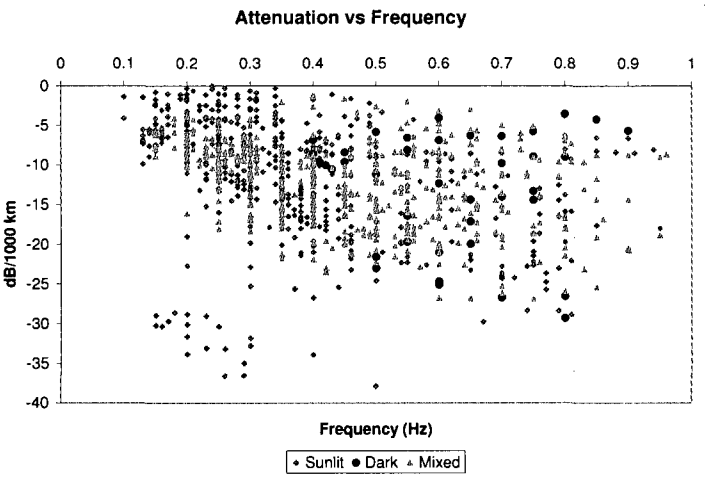

Figure 4-16: Spectral power attenuation versus frequency under three ionospheric sunlight conditions.

the waveguide is strongly dependent on the conductivity. Note that the occurrences in each sunlight condition are normalized. The cutoff feature in the waveguide is not the property of the medium but of the boundary conditions. At the lower frequency cutoff, the wavelength is longer than the physical extent of the ionosphere in altitude so that the ionospheric waveguide has little effect on the wave since most of the wave (in wavelength) is not confined in the waveguide. At higher frequencies, on the contrary, the wavelength becomes small enough to be confined in the waveguide and thus the wave propagation becomes more sensitive to the physical size of the waveguide, which is affected by the ionospheric sunlight condition. Therefore, dark-time cutoff frequencies are higher than the sunlit-time cutoffs (Greifinger & Greifinger 1968), which is confirmed in this study.

4.4.3 Polarization Characteristics

Polarization ellipticity observations at each station under the three sunlight conditions are presented in percentiles as shown in Figure 4-18, showing that both LHP and RHP modes are dominant at HBA and the occurrence of LP mode at HBA is about 10%. On the

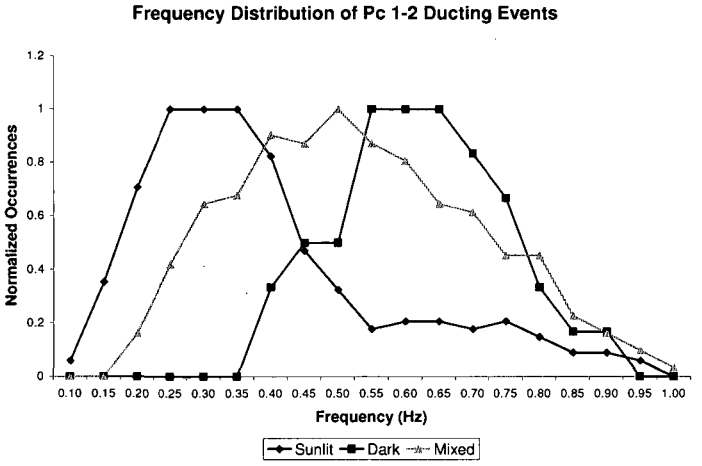

Figure 4-17: Frequency distribution of Pc 1–2 ducting events under three ionospheric sunlight conditions. Note that the occurrences in each sunlight condition are normalized.

other hand, both LHP and RHP modes decrease and the LP mode increases at the higher latitudes. EMIC waves are typically in the LHP Alfvén mode (or LP mode as the waves propagate toward the ionosphere) and, within the extent of the incident wave into the ionosphere, the ground data show LHP mode predominantly while LP and RHP modes are also found. Mode conversion from the incident Alfvén waves to the ducted compressional mode waves occurs within the extent of the injection region (Fujita & Tamao 1988) and at larger lateral distance compared with the wave incident region, signals found on the ground should be identified as ducted waves in LP mode since the incident waves are attenuated rapidly with distance (Hayashi et al. 1981). Greifinger (1972) predicted that the ducted waves are nearly LP. However, a somewhat more complicated polarization pattern has been reported by a number of observation studies (e.g., Fraser (1975*b*), Hayashi et al. (1981), Inhester et al. (1984)), which is discussed below.

As commented earlier, it is predicted that meridional propagation is most efficient. Greifinger & Greifinger (1973) explained that off-meridian propagation involves the appear-

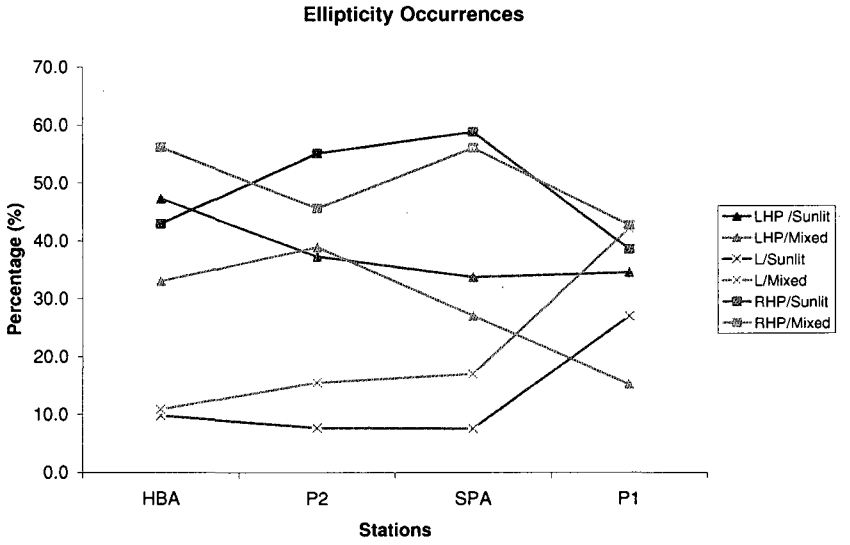

Figure 4-18: Ellipticity occurrence percentiles over distance using the data from the Antarctic array. Note that the events under dark ionospheric condition are not included due to insufficient number of events.

ance of resonant absorption peaks at certain frequencies. Fujita (1988) predicted in his model that Poynting loss appears when the ducted wave propagates out of the meridian plane. Figure 4-19 demonstrates a relationship between polarization angle at HBA and attenuation to examine how much initial horizontal propagation direction near the injection region (i.e., at HBA) affects attenuation during propagation in the waveguide. Since meridional propagation is thought to be most efficient, it can be observed that if the initial propagation direction is along the magnetic meridian (i.e., $\theta = 90°$ as predicted by Fujita & Tamao (1988) assuming that HBA is close to the injection region), attenuation should be small. On the other hand, if the initial horizontal propagation direction is off-meridian, attenuation should increase.

Figure 4-20, presented by Fujita & Tamao (1988), sketches horizontal spatial distributions of polarization patterns for the incident wave in the magnetosphere and the transmitted wave on the ground, suggesting that the magnetic vector rotates by 90° but the

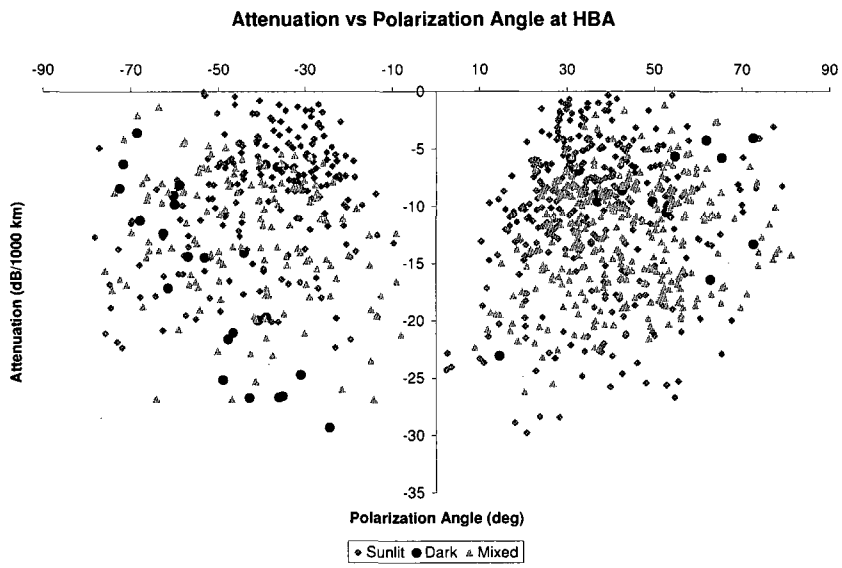

Figure 4-19: Plots showing the relationship between spectral power attenuation and polarization ellipse major axis angle at HBA using the data from the Antactic array.

polarization sense keeps its direction in transmission through the E layer. Fujita & Tamao (1988) also suggest that the polarization pattern on the ground shows that, near the wave injection region, the major axis of polarization is perpendicular to the radial direction from the region whereas, in the surrounding region, the major axis points to the region. The result in Figure 4-19 appears to support this scenario since the attenuation appears to be lower at higher angles (i.e., for meridional propagation near the wave injection region). It is also shown in Figure 4-19 that the events under the dark-time and mixed-time conditions tend to display the tendency in a more well-defined manner than those under the sunlit condition. This might be due to less inhomogeneity in the ionosphere during dark (or mixed) conditions.

It should be noted that the results in Figure 4-18 and Figure 4-19 do not always show polarization patterns as predicted in previous studies rather displaying a somewhat complex pattern in the polarization change and in the relationship between polarization angle and

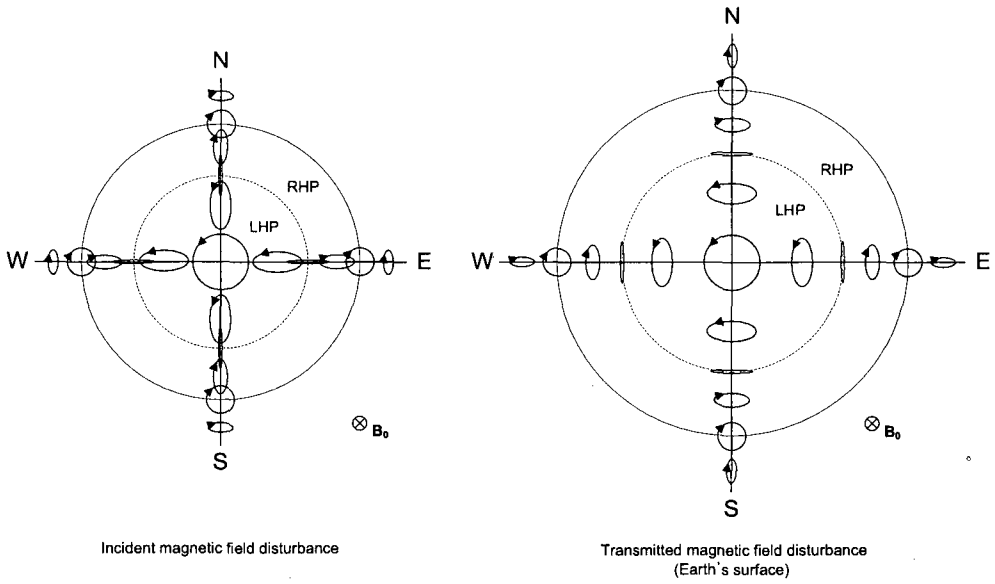

Figure 4-20: Horizontal spatial distributions of polarization patterns for incident wave (left) and transmitted wave on the ground (right). Circles drawn with a broken line and a solid line are demarcations of the polarization sense and the major axis direction, respectively (after Fujita & Tamao (1988)).

attenuation. In general, propagation properties change in a very complicated way as waves propagate through inhomogeneous media. As an example, through reflection, refraction and transmission in different media, waves may change their amplitudes and phases and hence affect the polarization characteristics of the waves.Baranskiy (1970) predicted that polarization is complicated by the presense of a thin, strongly absorbing ionospheric layer and thus ellipticity tends to become smaller (LP) in nighttime than in daytime. This agrees well with the observations by Fraser & Summers (1972) suggesting that well-defined LP events relating to a high latitude wave injection region are most likely to occur when the ionosphere is most uniform whereas LP events observed during sunrise and in the daytime are not generally correlated with the direction of an injection region. Hayashi et al. (1981) also observed that the polarization major axes at several stations in high latitudes do not necessarily direct to one point, which might be due to the ionospheric inhomogeneities.

To summarize, the complexity in polarization pattern might be due to 1) the horizontal inhomogeneity of the ionospheric conductivity (Hayashi et al. 1981, Belova et al. 1997) or the ground conductivity (Fraser 1975*b*); 2) waves with multiple frequency components from different injection regions; 3) superposition effects through refraction, reflection, and transmission in the waveguide (Altman & Fijalkow 1980); 4) at high latitudes, the array is located close to the wave injection region where the superposed effect of incident waves and ducted waves is more dominant (Hayashi et al. 1981); and 5) polarization change of EMIC waves during propagation in the magnetosphere (Young et al. 1981, Horne & Thorne 1993, Meredith et al. 2003, Hu & Denton 2009).

4.5 Summary

Simultaneous observations of ULF Pc 1–2 waves have been made from the Antarctic search-coil magnetometer array, consisting of five stations, covering an unprecedented range in geomagnetic latitude ($-62°$ to $-87°$, spanning geographically $\sim$ 2920 km) along a magnetic meridian and with uniform ionospheric condition. The meridional alignment of the array can provide useful information about wave propagation in the waveguide since it is known that ducting can occur most efficiently along the magnetic meridian. Using the data set obtained from the Antarctic search-coil magnetometer array in the year 2007, this study presents a statistical approach to understanding the Pc 1–2 wave propagation characteristics (attenuation and polarization) in the ionospheric waveguide centered around the F2 region altitude of maximum ionospheric electron density, in which a resonance cavity for Alfvén waves is formed and compressional waves propagate horizontally after mode conversion from the incident Alfvén waves to the compressional waves. Halley Station, located at the lowest latitude among the stations in the array, typically observed well-defined Pc 1–2 wave events with the strongest spectral power of any of the stations. The events, showing identical

spectral structure but less wave power, were detected at the other four stations located at higher latitudes.

The statistical study includes a total of 138 ULF Pc 1–2 wave events showing poleward propagation in the ionospheric waveguide. The Pc 1–2 ionospheric ducting occurred at all local times, but was more common during daytime hours, and showed peaks near 0700 MLT and 1400 MLT. The dates in the dataset are categorized into three conditions based on the sunlight condition in the ionosphere - "Sunlit" if an event occurred during sunlit ionopshere for all of the stations; "Dark" if an event occurred during dark ionosphere for all of the stations; "Mixed" if all of the stations during an event were under neither sunlit nor dark conditions. There are 67 sunlit events, 8 dark events, and 63 mixed events.

The followings are the major conclusions from the statistical study:

(1) Spectral power attenuation appears to be dependent on the ionospheric conductivity. Average attenuation is $\sim$ 11.10 dB/1000 km; $\sim$ 9.85 dB/1000 km (σ = 6.55) under sunlit conditions; $\sim$ 12.33 dB/1000 km (σ = 4.61) under mixed conditions; $\sim$ 13.81 dB/1000 km (σ = 7.08) under dark conditions. The wave propagation observed in this study appears to be more efficient than what is shown in previous studies perhaps because the ground array is effectively positioned along the magnetic meridian spanning $\sim$ 2920 km, ideal for measuring such wave ducting events since ducting can occur most efficiently along the magnetic meridian. The more efficient propagation during sunlit times found in this study might suggest that the ionospheric waveguide is governed by the Alfvén wave-induced Hall current, which increases under sunlit conditions.

(2) The statistical survey of the frequency components of the Pc 1–2 ducting events reveals that the frequency cutoff is strongly dependent on the ionospheric conductivity. In addition, the wave power attenuation increases with increasing frequency.

(3) Polarization analysis demonstrates that both LHP and RHP modes are dominant over

the LP mode at lower latitude (i.e., at HBA) and the occurrences of the LP mode at HBA are about 10%. It is also shown that the occurrences of both LHP and RHP modes decrease during propagation whereas the LP mode occurrences increase.

(4) It appears that the initial propagation direction (polarization angle at HBA in this case) is related to attenuation; at higher polarization angles at HBA, the attenuation appears to be smaller, which supports the idea that meridional propagation is most efficient.

(5) Although the overall patterns appear as predicted, the polarization results (as shown in Summary (3) and (4)) show somewhat complex patterns, which might be due to an inhomogeneity of the ionospheric conductivity; multiple injections of EMIC waves; superposition effects through refraction, reflection, and transmission in the waveguide; combined effects of incident waves and ducted waves; or polarization change of EMIC waves during propagation in the magnetosphere.

Chapter 5

Summary and Conclusions

This thesis encompasses a wide range of topics from hardware development to data analysis for space science research. The hardware development includes the system design of a set of ULF search-coil magnetometers which have been installed in the polar regions. The instruments are located to form an array so that simultaneous observations of geomagnetic pulsations in the ULF range can be made over a large region extending from the auroral zone to the polar cap region. This configuration is to perform large-scale systematic observations of the ULF wave propagation in the ionosphere. The data from one of the arrays installed in the polar regions, the Antarctic search-coil magnetometers located along a magnetic meridian, are analyzed to study wave propagation in the ionospheric waveguide.

A search-coil magnetometer can detect time-varying magnetic fields and is used to observe low-level magnetic field variations providing important information about the magnetosphere and its coupling to the ionosphere. Single-point ground observations of geomagnetic pulsations have a limited measurement range to investigate the temporal and spatial distribution of the wave events. In addition, the existence of the ionospheric waveguide, in which the waves can propagate isotropically near the Alfvén speed, complicates the ground observations. Thus, an array of ground-based stations can provide spatially and temporally extended observations which can lead to a better understanding of wave propagation characteristics. If the ground stations are located over a large extent to form an array (especially

along a magnetic meridian), time delays, determined by the group velocity of the waves, and phase differences can be observed. Chapter 2 describes the design, construction, and tests of ULF search-coil magnetometers.

Waves generated in space plasma by electron and ion dynamics associated with the geomagnetic field play an important role in establishing the interaction between the magnetosphere and the ionosphere by accelerating radiation belt particles and transporting magnetospheric energy to the ionosphere. Some of the energy of the magnetospheric waves is transmitted to the ionosphere while the waves propagate in the ionospheric waveguide, which is formed around the ionospheric F2 region altitude of the electron density maximum (at $\sim$ 400 km). The density structure forms a resonance cavity in which waves can propagate very efficiently in horizontal directions across field lines. Especially, the waves in the ULF Pc 1–2 range (0.1 – 5 Hz) are known to propagate most efficiently in this waveguide. The Pc 1–2 waves are typically associated with EMIC waves, which are excited by the ion cyclotron instability of a hot, anisotropic distribution of medium energy ring current ions in the equatorial region of the magnetosphere during geomagnetic storms and substorms.

Chapter 3 and Chapter 4 present simultaneous observations of ULF Pc 1–2 wave events from widely-spaced Antarctic ULF search-coil magnetometers with an unprecedented geomagnetic latitudinal range ($-62°$ to $-87°$, spanning $\sim$ 2920 km geographically) and positioning along a magnetic meridian. The observations of the Pc 1–2 waves show very well-defined propagation in the ionospheric waveguide. Chapter 3 focuses on a case study of Pc 1–2 wave activity propagating in the waveguide observed simultaneously from the ground array and the CHAMP satellite. In Chapter 4, the ground array data obtained in the year 2007 are analyzed to perform a statistical study of the MLT occurrences, wave power attenuation, and polarization characteristics of Pc 1–2 wave propagation in the ionospheric waveguide. For polarization analysis, a software tool has also been developed as

shown in Appendix A. The summary and conclusions of each chapter are as follows.

5.1 Development of Search-Coil Magnetometers

The magnetic field frequencies of interest in space physics include the ultra low frequency (ULF) range (a few mHz to a few Hz, as typically defined in space studies), which can be detected by a search-coil magnetometer. A search-coil magnetometer is especially suitable for space-borne instrumentation and unmanned ground-based configurations because of its low-power consumption (~tens of mW), simple structure, and reliability. It is also relatively easy to build mostly from off-the-shelf components and materials.

The search-coil magnetometers used in this study consist of two orthogonally mounted search-coil magnetic sensors to measure geomagnetic north-south and east-west wave activity. This setup identifies the polarization characteristics of magnetic field waves. The instruments can detect time-varying magnetic fields at a rate of 10 samples/sec with a sensitivity of 4.43 $V \cdot nT^{-1} \cdot Hz^{-1}$ and a resolution of $\sim$ 8 pT over a frequency range 0 – 2.5 Hz. GPS is used to synchronize the data acquisition process for time reference with 100 μsec accuracy.

In order to provide accurate simultaneous observations and to minimize output signal errors among the magnetometers in the array, a system design approach is essential, focusing on the standardization and consistency of the manufacturing/testing of the instruments. Various test methods have been applied for the characterization of the magnetometer systems, which include frequency response, resolution, and sensor/system deviation tests. Equivalent circuit models have also been used to compare with the test results as shown in Appendix B.

5.2 Pc 1–2 Wave Propagation Characteristics in the High-Latitude Ionospheric Waveguide

This thesis also presents analysis of the data from the magnetometer systems, mainly focusing on ULF wave propagation in the ionospheric waveguide (duct) centered around the electron density maximum near the F2 ionization peak. The Antarctic magnetometer array observes well-defined, band-limited ULF Pc 1–2 waves with poleward spectral power attenuation over a very extensive latitudinal coverage from geomagnetic latitudes of $-62°$ to $-87°$ (over the distance of 2920 km). Halley Station, located at the lowest latitude among the stations in the array, typically observed Pc 1–2 wave events with the strongest spectral power of any of the stations. The events, showing identical spectral structure but less wave power, were detected at the other four stations located at higher latitudes. This is a clear indication of the propagation of the electromagnetic ion cyclotron (EMIC) waves in the ionospheric waveguide. The study in this thesis focuses mainly on the ducting events by comparing spectral power attenuation factors and polarization patterns.

The statistical study includes a total of 138 ULF Pc 1–2 wave events showing poleward propagation in the ionospheric waveguide. The Pc 1–2 ionospheric ducting occurred at all local times but was more common during daytime hours, and showed peaks near 0700 MLT and 1400 MLT. The dates in the data set are categorized into three conditions based on the sunlight condition in the ionosphere - "Sunlit" if an event occurred during sunlit ionopshere for all of the stations; "Dark" if an event occurred during dark ionosphere for all of the stations; "Mixed" if all of the stations during an event were under neither sunlit nor dark conditions. There are 67 sunlit events, 8 dark events, and 63 mixed events.

The followings are the major conclusions from the statistical study:

(1) Spectral power attenuation appears to be dependent on the ionospheric conductivity. Average attenuation is $\sim$ 11.10 dB/1000 km; $\sim$ 9.85 dB/1000 km (σ = 6.55) under sunlit

conditions; $\sim$ 12.33 dB/1000 km (σ = 4.61) under mixed conditions; $\sim$ 13.81 dB/1000 km (σ = 7.08) under dark conditions. The wave propagation observed in this study appears to be more efficient than what is shown in previous studies perhaps because the ground array is effectively positioned along the magnetic meridian spanning $\sim$ 2920 km, ideal for measuring such wave ducting events since ducting can occur most efficiently along the magnetic meridian. The more efficient propagation during sunlit times found in this study might suggest that the ionospheric waveguide is governed by the Alfvén wave-induced Hall current, which increases under sunlit conditions.

(2) The statistical survey of the frequency components of the Pc 1–2 ducting events reveals that the frequency cutoff is strongly dependent on the ionospheric conductivity. In addition, the wave power attenuation increases with increasing frequency.

(3) Polarization analysis demonstrates that both LHP and RHP modes are dominant over the LP mode at lower latitude (i.e., at HBA) and the occurrences of the LP mode at HBA are about 10%. It is also shown that the occurrences of both LHP and RHP modes decrease during propagation whereas the LP mode occurrences increase.

(4) It appears that the initial propagation direction (polarization angle at HBA in this case) is related to attenuation; at higher polarization angles at HBA, the attenuation appears to be smaller, which supports the idea that meridional propagation is most efficient.

(5) Although the overall patterns appear as predicted, the polarization results (as shown in Summary (3) and (4)) show somewhat complex patterns, which might be due to an inhomogeneity of the ionospheric conductivity; multiple injections of EMIC waves; superposition effects through refraction, reflection, and transmission in the waveguide; combined effects of incident waves and ducted waves; or polarization change of EMIC waves during propagation in the magnetosphere.

One satellite-ground conjunction study is also presented. During the CHAMP overflight,

a transverse and linearly polarized ULF Pc 1 wave was found over a limited latitudinal extent ($-53°$ to $-61°$ ILAT), which supports the idea that EMIC waves are injected at low latitudes and ducted in the ionosphere. Given certain assumptions, the polarization ellipse observed on the ground becomes increasingly LP with the major axis pointing toward (or away from) the wave injection region as Pc 1 emissions propagate away from the injection region in the ionospheric waveguide. In addition, according to a model prediction, near the injection center, the major axis of polarization is perpendicular to the radial direction from the injection region. In the surrounding region, however, the major axis points to the center. The polarization angle pattern change observed from the ground array (e.g., $\sim +75°$ at HBA, being less at higher latitudes) during the CHAMP overflight and the plasmapause location estimation using a model and the CHAMP observations of the wave activity might imply that the waves were injected near HBA, perhaps near the CHAMP trace (between $L = 2.5$ and 4.4), and propagated in a poleward direction in the waveguide. However, it is quite challenging to determine the extent of the injection region with the meridional configuration of the array used in this study. Moreover, a complex polarization pattern (i.e., change in ellipticity and polarization angle) was found on the ground during propagation, which might be attributed to the array being close to the wave injection region where the superposed effect of incident waves and ducted waves is dominant.

5.3 Concluding Remarks

The observations of Pc 1–2 wave propagation in the ionospheric waveguide, showing much less attenuation compared to the other previous observations, are unique in that the ducted waves, seen over an array with an unprecedented geomagnetic latitudinal range and positioning along a magnetic meridian (a condition that provides the most efficient waveguide propagation), have rarely been measured before over such a latitudinally extended region.

The array deployed in the Antarctic terrain also has the very significant advantage of minimal geoelectric inhomogeneity since polarization observed on the ground may not reflect the true wave properties due to the inhomogeneous ground conductivity. In addition, clearly distinguishable ionospheric sunlight conditions in Antarctica can provide a more systematic change of the polarization pattern on the ground. Simultaneous observations of the Pc 1 wave event from the CHAMP satellite provide very useful information as to where wave events that are incident to the ionospheric waveguide can occur.

Appendices

Appendix A

Polarization Analysis Technique

A.1 Polarization of Plane Waves

Polarization is a property of waves that describes the orientation of their oscillations. According to the IEEE Standard Definitions for Antennas, the polarization of a radiated wave is defined as "that property of a radiated electromagnetic wave describing the time-varying direction and relative magnitude of the electric (or magnetic) field vector; specifically, the figure traced as a function of time by the extremity of the vector at a fixed location in space and the sense in which it is traced, as observed along the direction of propagation" (Balanis 1989). Polarization is the curve traced by the field vectors at a certain space or time and is observed along the direction of propagation.

A monochromatic wave can be expressed in the form

$$\mathbf{E}(x, y, z, t) = E_x \hat{\mathbf{x}} + E_y \hat{\mathbf{y}}$$

where

$$E_x(x, y, z, t) = A_x \cos(\omega t - kz + \phi_x)$$

$$E_y(x, y, z, t) = A_y \cos(\omega t - kz + \phi_y)$$

with positive real amplitudes A_x and A_y, wave number $k = 2\pi/\lambda$, and phase angles ϕ_x

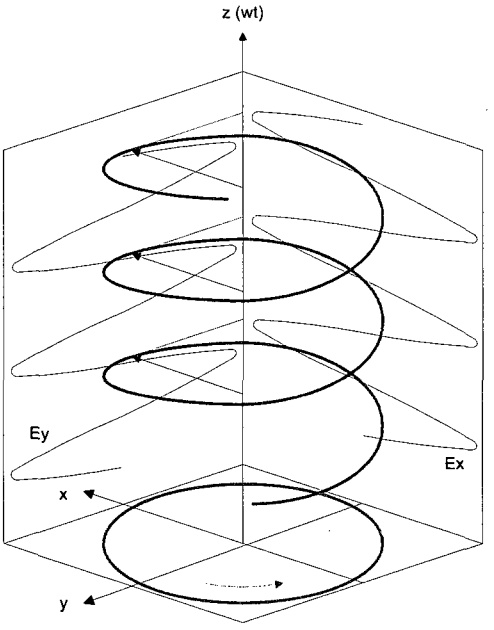

Figure A-1: An example of rotation of a plane wave at z = 0 as a function of time: right-hand circular polarization as seen in a plane perpendicular to the direction of propagation.

and ϕ_y. Polarization can be classified into three types - linear, circular, and elliptical - depending on the phase difference

$$\phi = \phi_y - \phi_x$$

and on the relative size of the wave amplitudes A_x and A_y. A three-axis coordinate system is typically used for the representation of polarization, in which the x-axis is in the vertical direction, the y-axis horizontal, and the z-axis along the direction of propagation. Figure A-1 is one of the typical field traces at $z = 0$ as a function of time.

If the field propagation is toward the reader (with the z-axis out of the page), the figure of the field is traced in a clockwise (CW) or counterclockwise (CCW) sense, which are also designated as left-hand polarization (LHP) and right-hand polarization (RHP), respectively in electromagnetics as shown in Figure A-2. This type of representation is called a *hodogram.* It should be noted, however, that the convention in optics is the opposite: CW sense is RHP

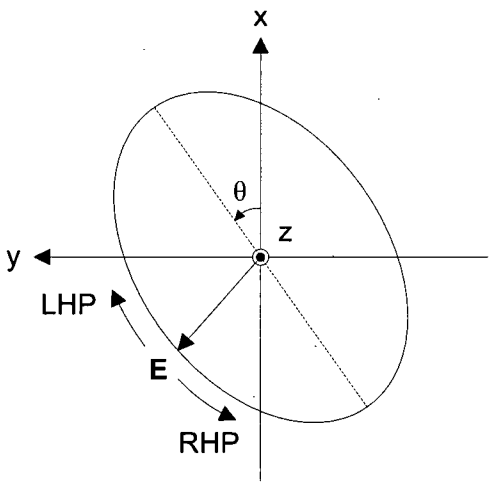

Figure A-2: An example of representation of a polarized field by the convention in electromagnetics. This type of representation is called a hodogram. Clockwise (CW) sense and counterclockwise (CCW) sense of the field trace are designated as left-hand polarization (LHP) and right-hand polarization (RHP), respectively. Note that the convention in optics applies in the opposite way - CW is RHP and CCW is LHP.

and CCW is LHP (Klein & Furtak 1986). In this article, the convention in electromagnetics is used. In general, the axes of the ellipse are not in the x and y direction. As shown in Figure A-2, the angle between the x-axis and the major axis of the ellipse is denoted as the angle θ, which will be called the polarization angle hereinafter.

A monochromatic wave is always polarized, which means with increasing time the polarization trace in space is an ellipse with periodicity. This shape may reduce in special cases to a circle (circular polarization) or a straight line (linear polarization). In the case of an unpolarized wave, the trace of the wave vector shown in a plane perpendicular to the direction of propagation becomes very irregular and therefore the wave shows no preferential directional properties. These two cases represent complete coherence and complete incoherence, respectively. In reality, a wave is partially polarized; i.e., the variation of the field vectors is neither completely regular nor completely irregular. In general, a partial polarization is usually due to reflection or scattering (Born & Wolf 1999). This type of po-

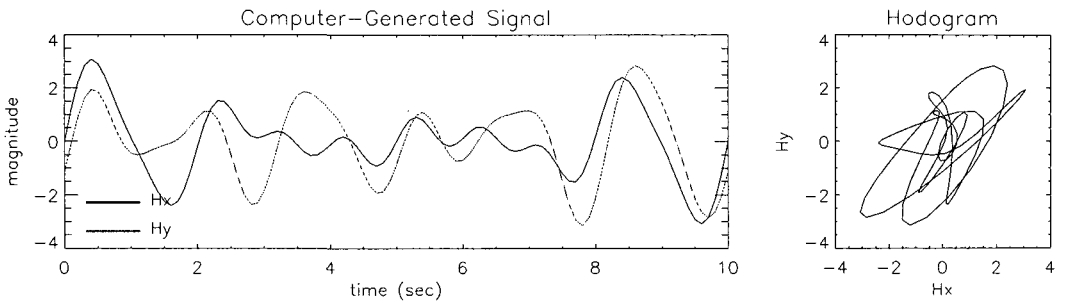

Figure A-3: An example of a hodogram from a computer-generated signal of multiple frequencies, amplitudes, and phase angles, which mimics a natural signal.

larization characteristic contributes to the complexity of the polarization analysis of natural signals. Whereas the hodogram technique as shown in Figure A-2 can provide a snapshot of the wave polarization in a monochromatic case, this technique may not allow one to infer quantitatively the polarization parameters due to the mixed nature of the regularity and irregularity of the wave vector variation. Figure A-3 demonstrates an example of a hodogram from a computer-generated signal of multiple frequencies, amplitudes, and phase angles, which mimics a natural signal. As seen in this figure, the hodogram technique may not be applied as an appropriate polarization analysis tool. The next section will describe a more efficient polarization analysis technique to study geomagnetic pulsations.

A.2 Polarization Analysis for Geomagnetic Pulsations

A.2.1 Theory

The interpretation of geomagnetic micropulsations in terms of physical and mathematical models requires certain knowledge of the polarization of these signals. The hodogram technique is based on simple, physically nonrealizable monochromatic theory and is generally not applicable to many types of geomagnetic signals due to the nature of their complexity. This section describes a polarization analysis technique based on the methods introduced by

Fowler et al. (1967), Rankin & Kurtz (1970), and Means (1972). These studies commonly use the theory studied by Born & Wolf (1999).

A monochromatic or quasi-monochromatic signal of frequency ω, propagating in the positive z direction can be represented by a time sequence of analytic signals:

$$h_x(t) = A_x \sin(\omega t + \phi_x) + U_x(t) \tag{A.1}$$

$$h_y(t) = A_y \sin(\omega t + \phi_y) + U_y(t) \tag{A.2}$$

where A_x and A_y are the amplitudes of each component and ϕ_x and ϕ_y are the phase delays. $U_x(t)$ and $U_y(t)$ are unpolarized signals. If the signal is monochromatic (i.e., totally polarized), A_x, A_y, ϕ_x, and ϕ_y are constants and U_x, $U_y = 0$. For a quasi-monochromatic signal, these quantities depend also on time, t, but their temporal changes are small enough to be negligible in any time interval compared to the coherence time.

The power matrix, **J**, (see Born & Wolf (1999), Fowler et al. (1967), and Rankin & Kurtz (1970) for more detail) can be expressed as the sum of a totally polarized signal and a completely unpolarized signal which is as follows:

$$\mathbf{J} = \mathbf{P} + \mathbf{U} \tag{A.3}$$

where **P** and **U** are the matrix for the polarized and unpolarized component, respectively. The matrix can thus be given

$$\mathbf{J} = \begin{bmatrix} A_x^2 + |U_x|^2 & A_x A_y e^{i\delta} \\ A_x A_y e^{-i\delta} & A_y^2 + |U_y|^2 \end{bmatrix} \tag{A.4}$$

where A_x, A_y, δ are chosen to represent the appropriate time averages and $\delta = \phi_y - \phi_x$. If $\delta > 0$, the polarization sense is CCW (RHP in electromagnetics). Rewriting the matrix

form,

$$\mathbf{J} = \begin{bmatrix} J_{xx} & J_{xy} \\ J_{yx} & J_{yy} \end{bmatrix} = \begin{bmatrix} P_{xx} & P_{xy} \\ P_{yx} & P_{yy} \end{bmatrix} + \begin{bmatrix} U_{xx} & U_{xy} \\ U_{yx} & U_{yy} \end{bmatrix} \tag{A.5}$$

As indicated in Equation A.4,

$$U_{xy} = U_{yx} = 0 \tag{A.6}$$

Assuming that the unpolarized components are similarly contributed,

$$U_{xx} = U_{yy} \tag{A.7}$$

Therefore, the matrix form in Equation A.5 can be rewritten as

$$\mathbf{J} = \begin{bmatrix} J_{xx} & J_{xy} \\ J_{yx} & J_{yy} \end{bmatrix} = \begin{bmatrix} P_{xx} + U & P_{xy} \\ P_{yx} & P_{yy} + U \end{bmatrix} \tag{A.8}$$

Using determinant $|\mathbf{J}|$

$$|\mathbf{J}| = P_{xx}P_{yy} + U^2 + (P_{xx} + P_{yy})U - P_{xy}P_{yx} \tag{A.9}$$

the unpolarized component U is obtained from

$$U = \frac{-(P_{xx} + P_{yy})}{2} \pm \frac{((P_{xx} + P_{yy})^2 + 4|\mathbf{J}|)^{1/2}}{2} \tag{A.10}$$

where only the positive sign is used since U is positive. Therefore, the components in $\mathbf{J}$ can be represented as

$$J_{xx} = P_{xx} + U = \frac{P_{xx} - P_{yy}}{2} + \frac{((P_{xx} + P_{yy})^2 + 4|\mathbf{J}|)^{1/2}}{2} \tag{A.11}$$

$$J_{yy} = P_{yy} + U = \frac{P_{yy} - P_{xx}}{2} + \frac{((P_{xx} + P_{yy})^2 + 4|\mathbf{J}|)^{1/2}}{2} \tag{A.12}$$

$$J_{xy} = P_{xy} \tag{A.13}$$

$$J_{yx} = P_{yx} \tag{A.14}$$

The *degree of polarization* (R) is defined as the ratio of the polarized signal to the total signal intensity or

$$R = \frac{P_{xx} + P_{yy}}{J_{xx} + J_{yy}} = \left(1 - \frac{4|\mathbf{J}|}{(J_{xx} + J_{yy})^2}\right)^{1/2} \tag{A.15}$$

The *coherency* (C) is defined as

$$C = \frac{J_{xy}}{\sqrt{J_{xx}J_{yy}}} = \left(\frac{J_{xy}J_{yx}}{J_{xx}J_{yy}}\right)^{1/2} \tag{A.16}$$

If $C = 1$, the signal is completely polarized and if $C = 0$, completely unpolarized.

The *ellipticity* (ε) is defined as the ratio of the minor axis to the major axis of the ellipse or

$$\varepsilon = \tan\beta \tag{A.17}$$

where

$$\sin 2\beta = \frac{2\mathrm{Im}(J_{xy})}{((J_{xx} + J_{yy})^2 - 4|\mathbf{J}|)^{1/2}} \tag{A.18}$$

The polarization sense is defined by the sign of β: if $\beta > 0$, the polarization is RHP (CCW); if $\beta < 0$, LHP (CW).

The *polarization angle* (θ) is the angle that the principal axis of polarization makes with the X axis or the orientation of the polarization ellipse as described in Figure A-2, which is represented as

$$\tan 2\theta = \frac{2\mathrm{Re}(J_{xy})}{J_{xx} - J_{yy}} \tag{A.19}$$

In the case of a geomagnetic pulsation, the ellipticity is defined as the ratio of the minor axis to the major axis of the ellipse of the magnetic field perturbation in the plane perpendicular to the background magnetic field and the polarization angle implies the angle between the major axis of the polarization ellipse and the magnetic meridian in the north-south direction.

A.2.2 Implementation

For a numerical approach to implement the polarization analysis technique, each element of the power matrix is treated in the frequency domain instead of the time domain in order to obtain the parameters shown above: i.e., signal amplitude and phase delay. The power matrix components J_{ij} can be expressed as

$$J_{ij} = \int_{\Delta\omega} H_{ij}(\omega) d\omega \tag{A.20}$$

where $\Delta\omega$ is the effective bandwidth of the signal and H_{ij} is the real power spectral function when $i = j$ and H_{ij} is the complex cross-correlation function when $i \neq j$. In practice, the power spectrum and the cross spectrum of signals $h_x(t)$ and $h_y(t)$ are calculated: H_{xx}, power spectrum of $h_x(t)$; H_{yy}, power spectrum of $h_y(t)$; H_{xy}, cross spectrum of $h_x(t)$ on $h_y(t)$; H_{yx}, cross spectrum of $h_y(t)$ on $h_x(t)$, that is,

$$H_{xx} \equiv H_x(\omega) = \mathsf{F}(h_x(t)) \tag{A.21}$$

$$H_{yy} \equiv H_y(\omega) = \mathsf{F}(h_y(t)) \tag{A.22}$$

$$H_{xy} \equiv \mathsf{F}(h_y(t) \star h_x(t)) \tag{A.23}$$

$$H_{yx} \equiv \mathsf{F}(h_x(t) \star h_y(t)) \tag{A.24}$$

where F denotes Fourier Transform and $\star$ a cross-correlation. Since the cross-correlation is defined by

$$f \star g = \bar{f} * g \tag{A.25}$$

where $\bar{f}$ is the complex conjugate of f and $*$ denotes convolution and

$$\mathsf{F}(f \star g) = \bar{\mathsf{F}}(f) \cdot \mathsf{F}(g) \tag{A.26}$$

the cross spectra, H_{xy} and H_{yx} can be rewritten as

$$H_{xy} = \bar{H}_y(\omega) \cdot H_x(\omega) \tag{A.27}$$

$$H_{yx} = \bar{H}_x(\omega) \cdot H_y(\omega) \tag{A.28}$$

and the phases of the cross spectra, comparing the components given in Equation A.4, can be represented as

$$\delta_{xy} = \tan^{-1}\left(\frac{\mathrm{Im}(H_{xy})}{\mathrm{Re}(H_{xy})}\right) \tag{A.29}$$

$$\delta_{yx} = \tan^{-1}\left(\frac{\mathrm{Im}(H_{yx})}{\mathrm{Re}(H_{yx})}\right) \tag{A.30}$$

Therefore, the power matrix components can be given as

$$J_{xx} = |H_{xx}|^2 \tag{A.31}$$

$$J_{yy} = |H_{yy}|^2 \tag{A.32}$$

$$J_{xy} = |H_{xx}||H_{yy}|e^{i\delta_{xy}} \tag{A.33}$$

$$J_{yx} = |H_{xx}||H_{yy}|e^{i\delta_{yx}} \tag{A.34}$$

and now they can be used for the polarization parameters associated with the signal: degree of polarization (Equation A.15), coherency (Equation A.16), ellipticity (Equation A.17 and Equation A.18), and polarization angle (Equation A.19).

The ULF search-coil sensors used in this study are aligned with the X axis geomagnetically north-south and the Y axis east-west. Some of them are equipped with the Z axis which is aligned along the geomagnetic field **B**. The orientation of the sensors when installed on the ground is determined by using Cartesian coordinate systems - X (geomagnetic north), Y (geomagnetic east) and Z (down, along the field line) in the northern hemisphere; X (geomagnetic south), Y (geomagnetic east), and Z (up, along the field line) in the southern hemisphere. The positive direction of each axis is defined as a magnetic perturbation along the sensor axis in the direction toward which the sensor produces a positive signal when magnetic flux increases. For the polarization analysis using the Antarctic search-coil magnetometer array data used in this study, the signs of the X axis data are changed since the polarization ellipse should be presented on the plane where the X axis is directed toward north, Y axis west, and Z axis up (in other words, out of page; see Arnoldy et al. (1982)) to conform to the right-hand rule.

Appendix B

UNH ULF Search-Coil Magnetometer Technical Details

B.1 Search-Coil Magnetic Sensor Spool and Wiring Diagram

The search-coil sensor consists of 16 spools of enamel wire (36 AWG), each of which has 10,000 turns of wire. The spool winding diagram is presented in Figure B-1 showing how the wire starts and ends on the spool and in what direction the wire is wound. The spools have to be connected as shown in Figure B-2 so that each sensor provides identical polarity of signal output.

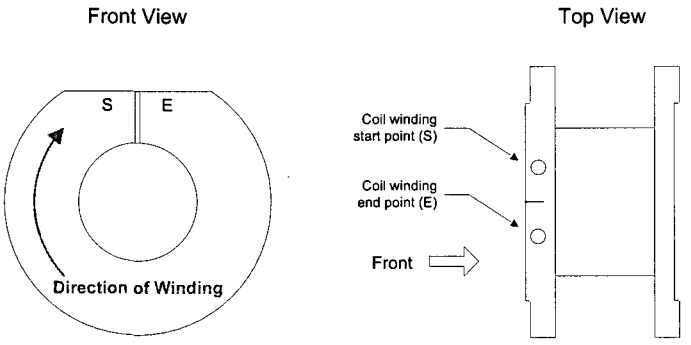

Figure B-1: Spool winding diagram showing how the wire is wound around the spool.

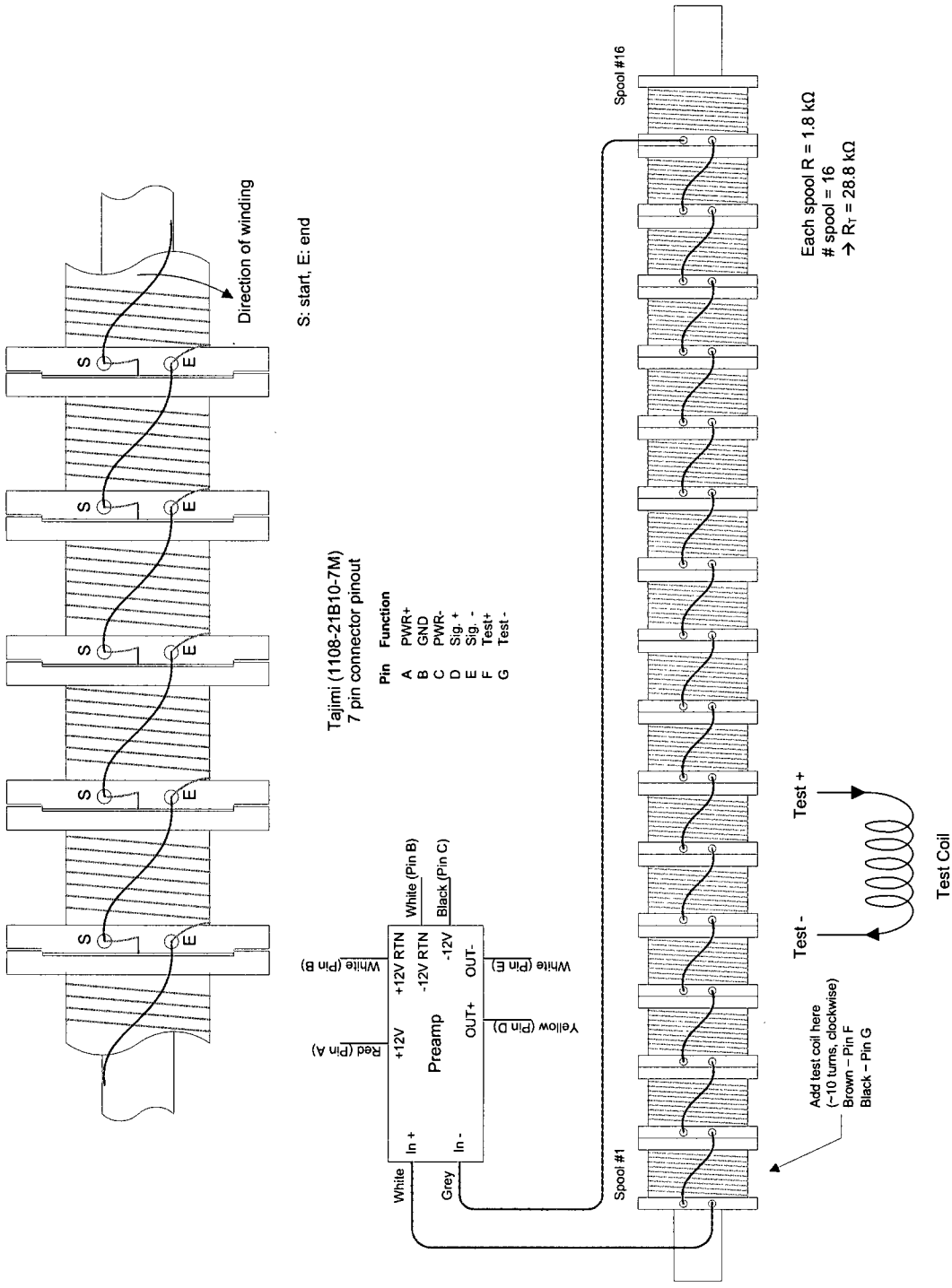

Figure B-2: UNH ULF search-coil magnetic sensor wiring diagram.

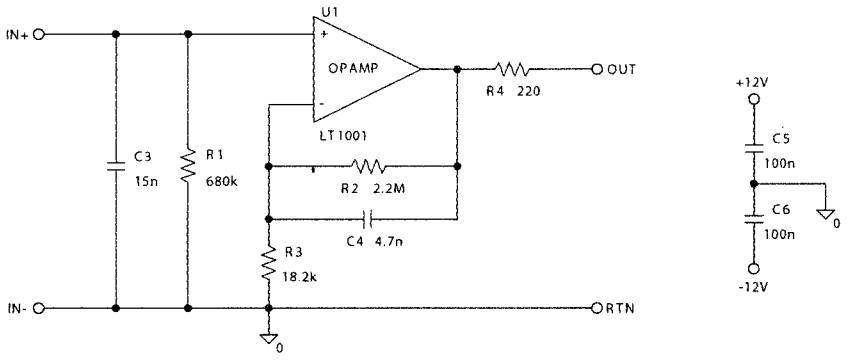

Figure B-3: Electrical schematic of the preamp circuit for the search-coil magnetic sensor.

B.2 Electrical schematic of Preamp

Figure B-3 shows the electrical schematic of the preamp circuit of the search-coil magnetic sensor. A first-order active low-pass filter (0 – 15 Hz, −3 dB corner frequencies) is used for the preamp circuit. Frequency response of the preamp circuit using an equivalent circuit model is described in Section B.5.

B.3 Electrical schematic of Main Analog Electronics

Figure B-4 shows the electrical schematic of the main analog circuit of the search-coil magnetometer system. A two-stage first-order passive low-pass filter and a two-stage first-order active low-pass filter are employed for the main analog circuit. The overall frequency response of the main analog electonics is 0 – 5 Hz (−3 dB corner frequencies). Frequency response of the main analog circuit using an equivalent circuit model is described in Section B.5.

B.4 Magnetometer System Cable Connection Diagram

The ULF search-coil magnetometer system cable connection diagram is shown in Figure B-5.

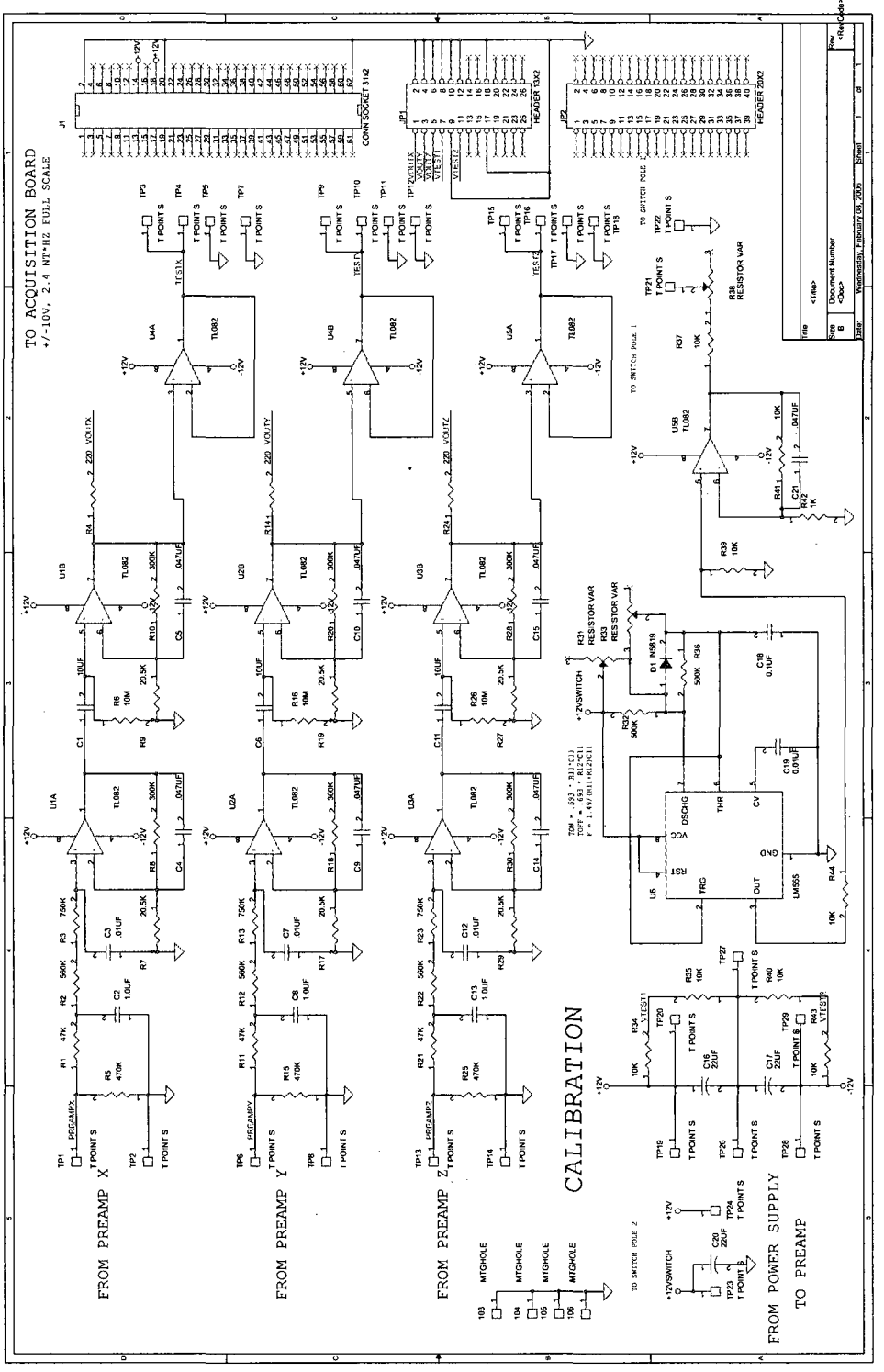

Figure B-4: Electrical schematic of the main analog circuit of the search-coil magnetometer system.

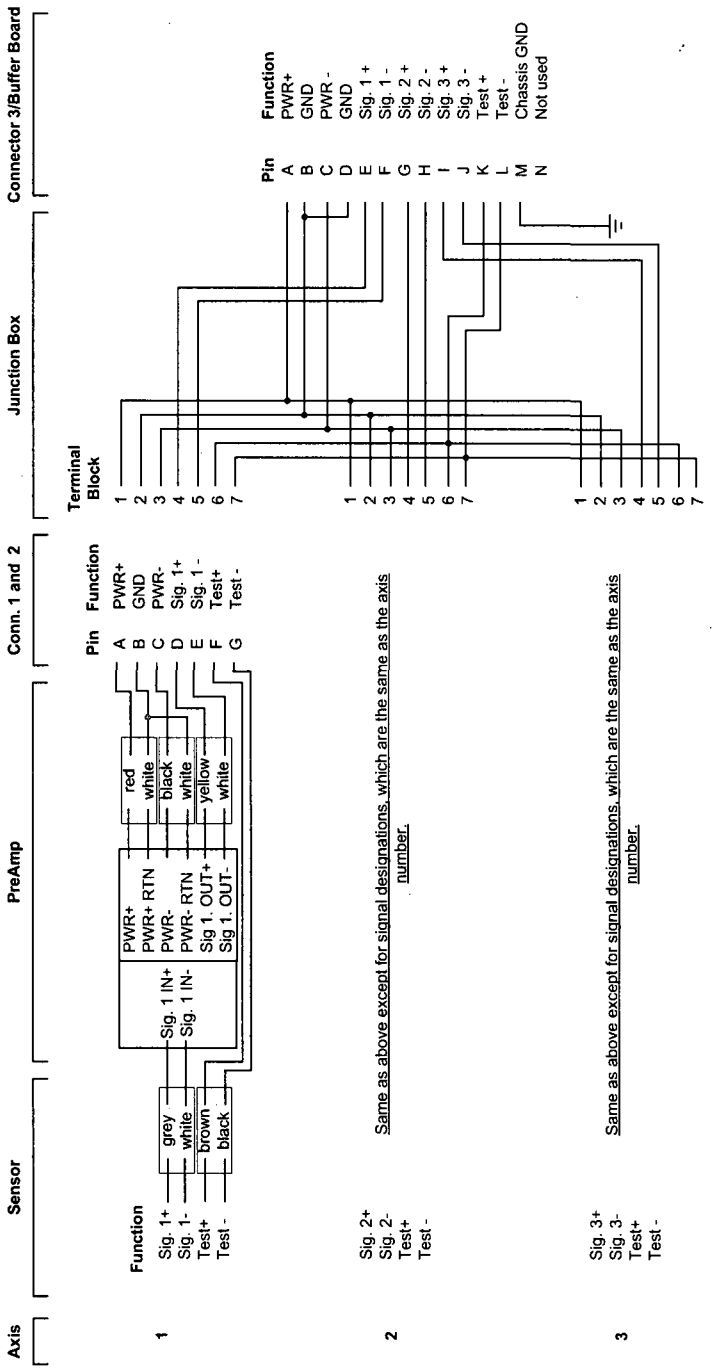

Figure B-5: ULF search-coil magnetometer system cable connection diagram.

B.5 Frequency Response Characterization of Search-Coil Magnetometer System Using Equivalent Circuit Model

B.5.1 Search-Coil Magnetic Sensor Model

A search-coil magnetic sensor can be modeled as a resistor ($R\_coil = 30\ k\Omega$) and an inductor ($L\_coil = 9.4$ kH). Figure B-6 shows the search-coil model used in this study. The inductance of the coil is calculated based on the coil geometry and winding. Since the magnetic flux, Φ, through the coil is a constant called the self inductance, L, times a current, I ($\Phi = LI$), the inductance, L, is represented as

$$L = \Phi/I = \mu_0 n^2 Al$$

where $\mu_0 = 4\pi \times 10^{-7}$ (H/m), n is number of turns per unit length (= total number of turns/coil length) and A is the cross-sectional area.

The coil model does not include capacitance because the C1 in the preamp circuit, as shown in Figure B-6, is much larger than the capacitance of the coil. In the calculation for the search-coil, C1 and R1 are also included, which forms an RLC circuit. The impedance of the entire coil block (Z_coil_block) is the parallel connection of the impedance of the coil (Z_coil) and the impedance of the coil components, C1 and R1 (Z_coil_term), that is

$$\text{Z\_coil\_block} = (\text{Z\_coil} \times \text{Z\_coil\_term})/(\text{Z\_coil} + \text{Z\_coil\_term})$$

where

$$\text{Z\_coil} = j\omega \text{L\_coil} + \text{R\_coil}$$

$$\text{Z\_coil\_term} = (R1/(j\omega C1))/(R1 + 1/(j\omega C1))$$

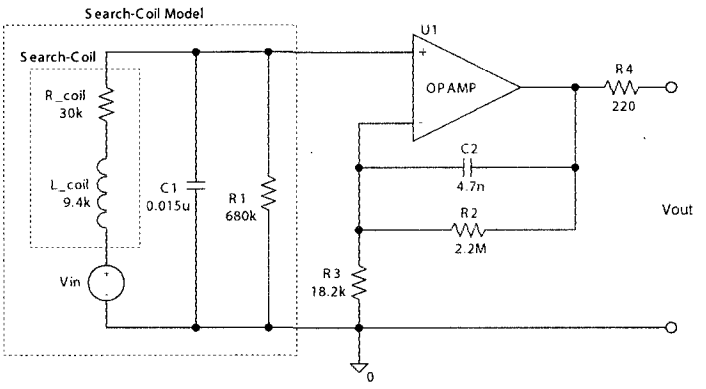

Figure B-6: Search-coil magnetic sensor model used in this study.

The transfer function, $T(j\omega)$ is

$$T(j\omega) = V_o/V_i = \text{Z\_coil\_term}/(\text{Z\_coil} + \text{Z\_coil\_term})$$

The magnitude frequency response is $|T(j\omega)|$ and the phase frequency response is $\angle T(j\omega)$ (Figure B-7).

B.5.2 Passive Low-Pass Filter Model

The main analog circuit of the ULF search-coil magnetometer is equipped with a two-stage first-order passive low-pass filter. Figure B-8 shows a first-order passive low-pass filter design. The cutoff frequency, ω_c, is represented as

$$\omega_c = 1/RC$$

or equivalently,

$$f_c = 1/(2\pi RC)$$

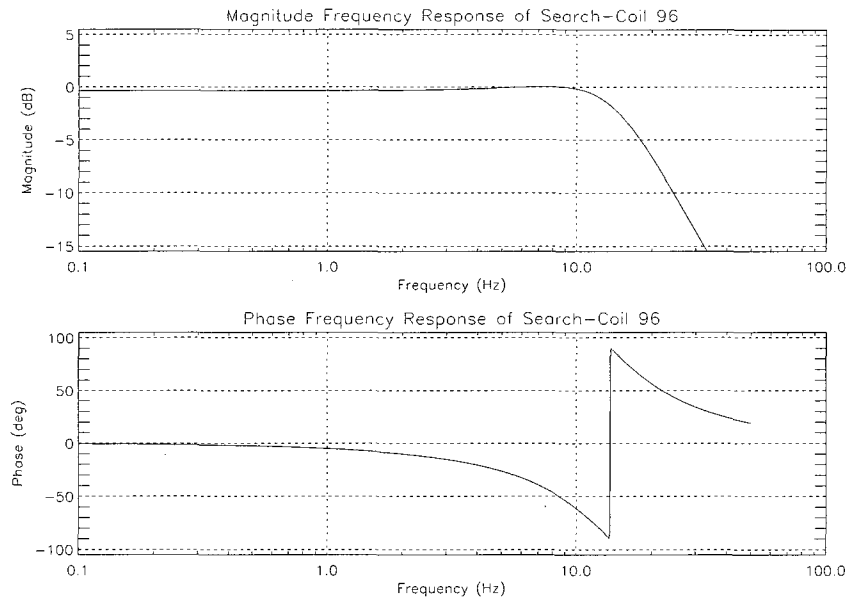

Figure B-7: Magnitude and phase frequency response of the search-coil magnetic sensor model.

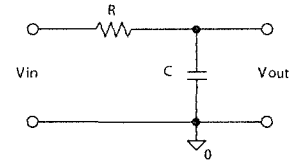

Figure B-8: First order passive low-pass filter model used in this study.

The transfer function of the passive low-pass filter is

$$T(j\omega) = V_o/V_i = (1/j\omega C)/(R + 1/j\omega C) = 1/(1 + j\omega RC)$$

B.5.3 Active Low-Pass Filter Model

In the ULF search-coil magnetometer circuit, a first-order active low-pass filter is used for the coil preamp and a two-stage first-order active low-pass filter is used for the main analog

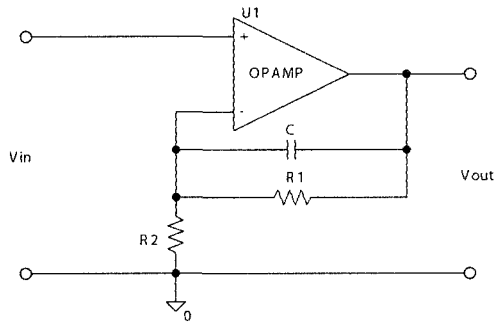

Figure B-9: First order active low-pass filter model used in this study.

circuit. A first-order active low-pass filter design is shown in Figure B-9. This design employs a non-inverting op-amp circuit. The cutoff frequency, ω_c, is represented as

$$\omega_c = 1/R1C$$

or equivalently,

$$f_c = 1/(2\pi R1C)$$

The impedance (Z_F) of the parallel components, R1 and C is

$$Z\_F = (R1(1/j\omega C))/(R1 + (1/j\omega C)) = R1/(1 + j\omega R1C) = R1/(1 + j(\omega/\omega_c))$$

The transfer function of the active low-pass filter is

$$T(j\omega) = V_o/V_i = 1 + Z\_F/R2 = 1 + (R1/R2)(1/(1 + j(\omega/\omega_c)))$$

The gain of the preamp can be obtained using the transfer function. Since R1 = 2.2 MΩ and R2 = 18.2 kΩ, the gain is 121 and 3 dB gain is 86 (= 121 × 0.707) when f = 0 Hz.

B.5.4 Modeling of the Overall Magnetometer System

The preamp consists of one first-order active low-pass filter (gain=121, see Figure B-3) and the main circuit has a total of four low pass filters as shown in Figure B-4. For example, the Channel X in Figure B-4 includes Block 1 (R1 and C2), Block 2 (R2, R3, and C3), Block 3 (U1A, R7, R8, and C4), and Block 4 (U1B, R9, R10, and C5). The total gain of the main circuit is obtained by combining the gain of each filter; i.e., the total gain of the main analog circuit is

$$|T_{total}(j\omega)| = |T_1(j\omega)| \times |T_2(j\omega)| \times |T_3(j\omega)| \times |T_4(j\omega)|$$

In addition, the total phase response is

$$\angle T_{total}(j\omega) = \angle T_1(j\omega) + \angle T_2(j\omega) + \angle T_3(j\omega) + \angle T_4(j\omega)|$$

The magnitude and phase frequency response of the preamp model is shown in Figure B-10. The magnitude and phase frequency responses of the main analog circuit models for each block (1 through 4) are presented in Figure B-11 through Figure B-14. Figure B-15 shows the model result for the entire main analog circuit. The overall magnetometer circuit model results without and with the search-coil magnetic sensor are presented in Figure B-16 and Figure B-17, respectively.

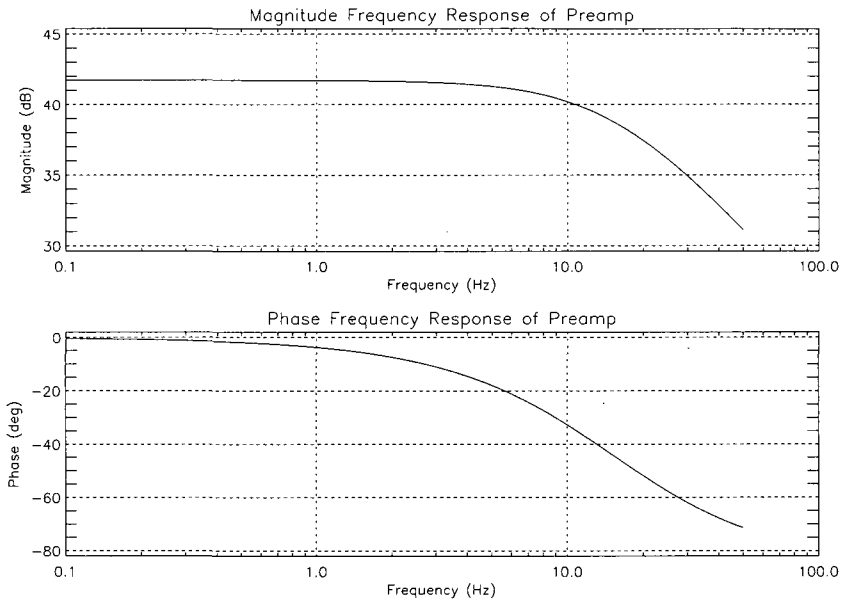

Figure B-10: Magnitude and phase frequency response of the preamp model.

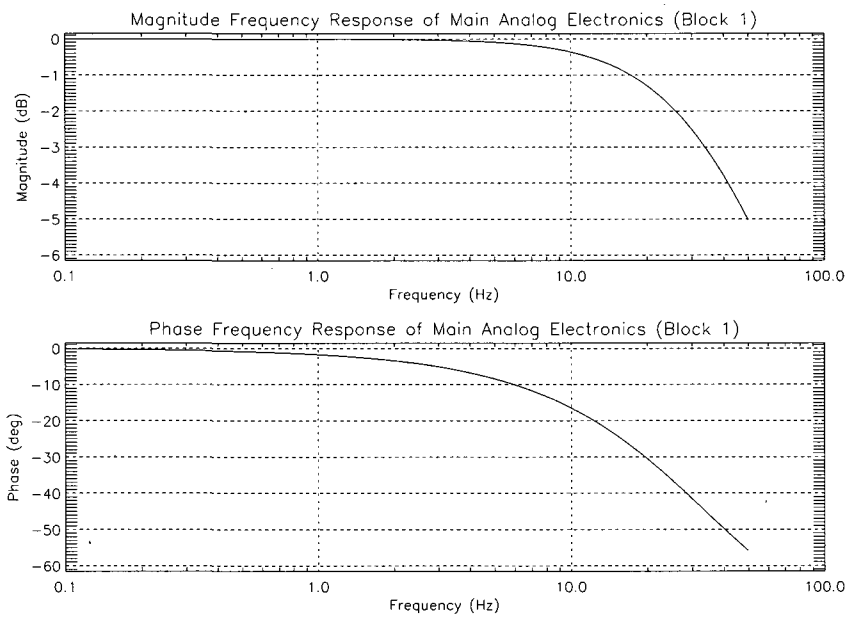

Figure B-11: Magnitude and phase frequency response of the main analog circuit model (Block 1).

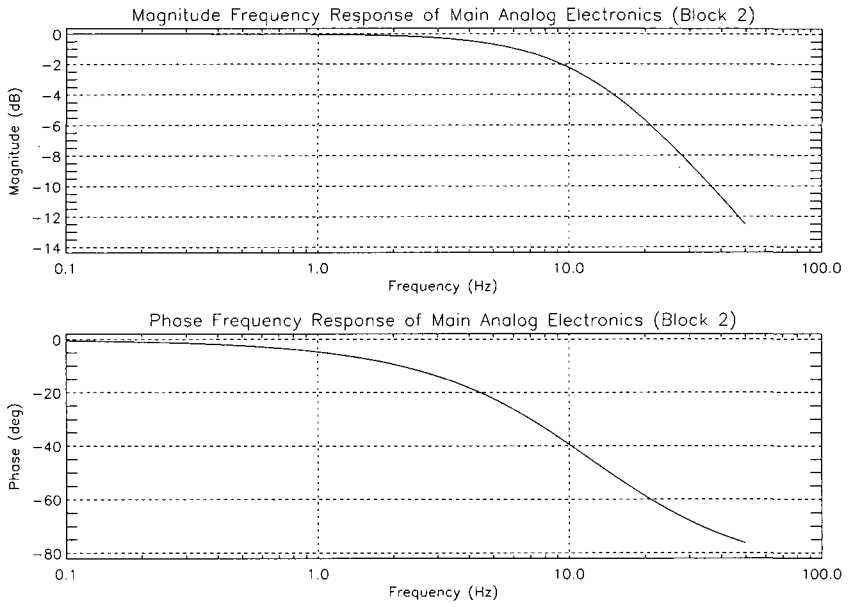

Figure B-12: Magnitude and phase frequency response of the main analog circuit model (Block 2).

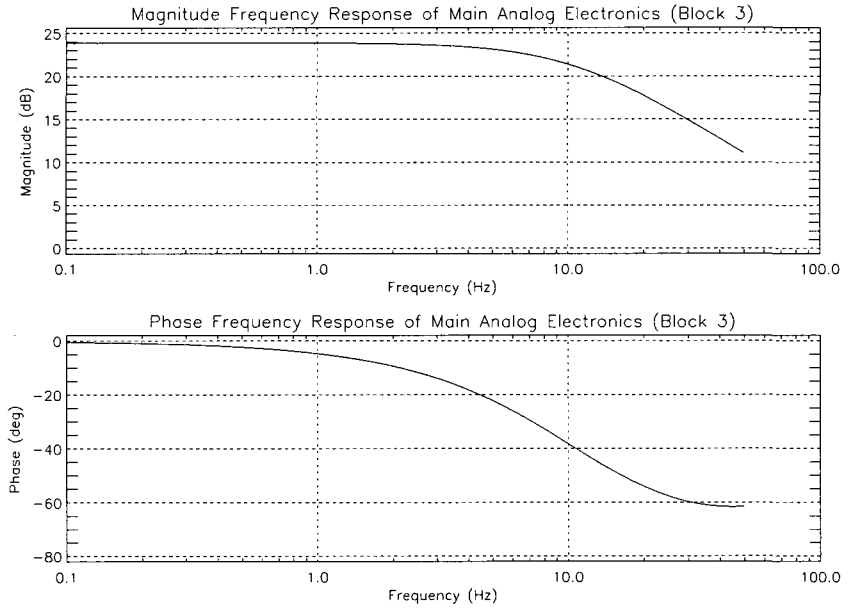

Figure B-13: Magnitude and phase frequency response of the main analog circuit model (Block 3).

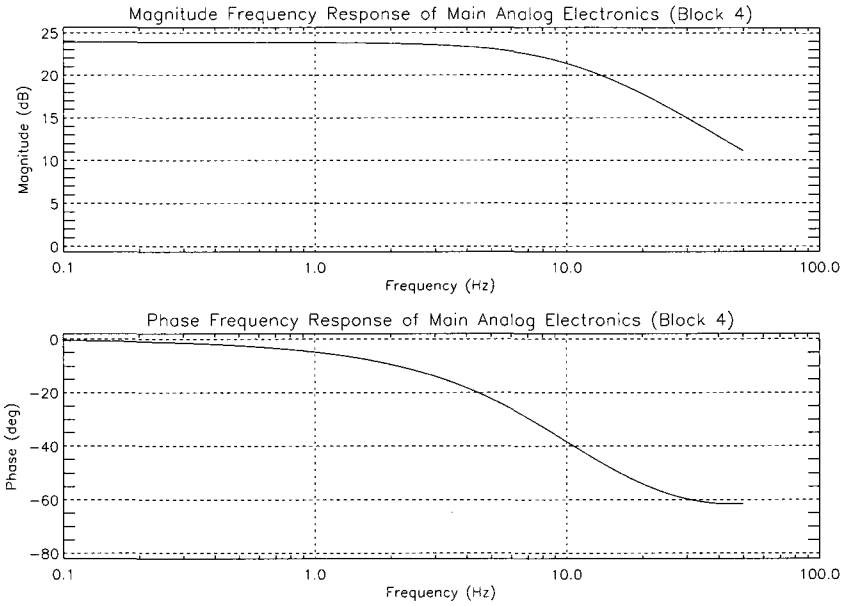

Figure B-14: Magnitude and phase frequency response of the main analog circuit model (Block 4).

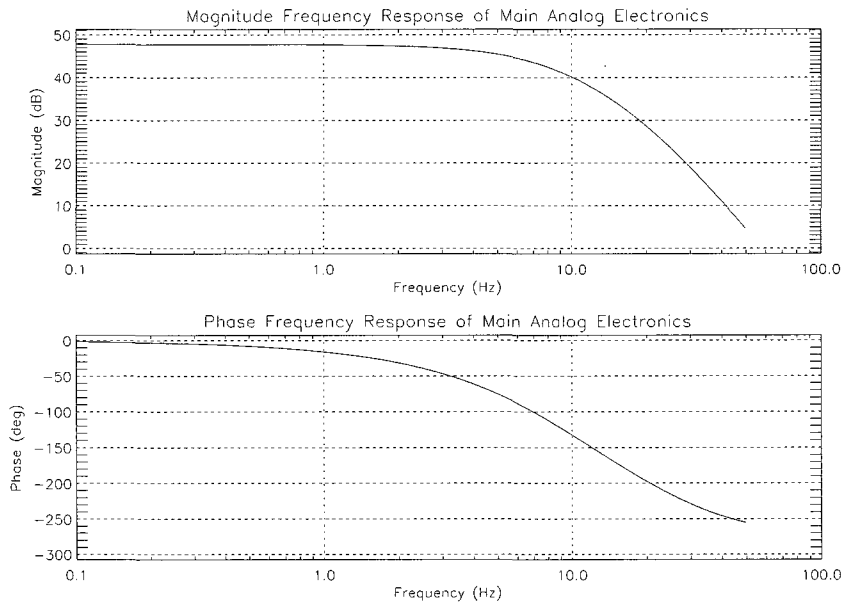

Figure B-15: Magnitude and phase frequency response of the main analog circuit model (Blocks 1 to 4).

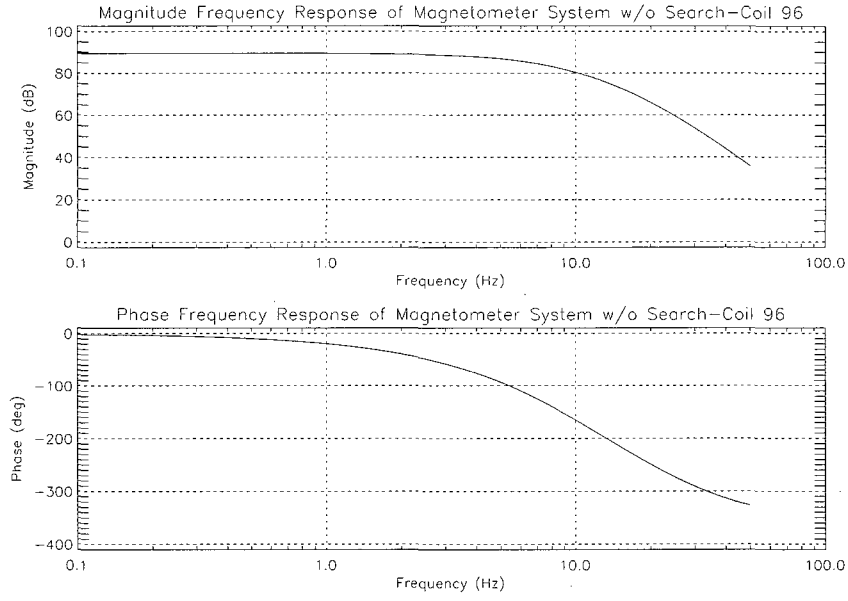

Figure B-16: Magnitude and phase frequency response of the overall magnetometer system model without the search-coil magnetic sensor.

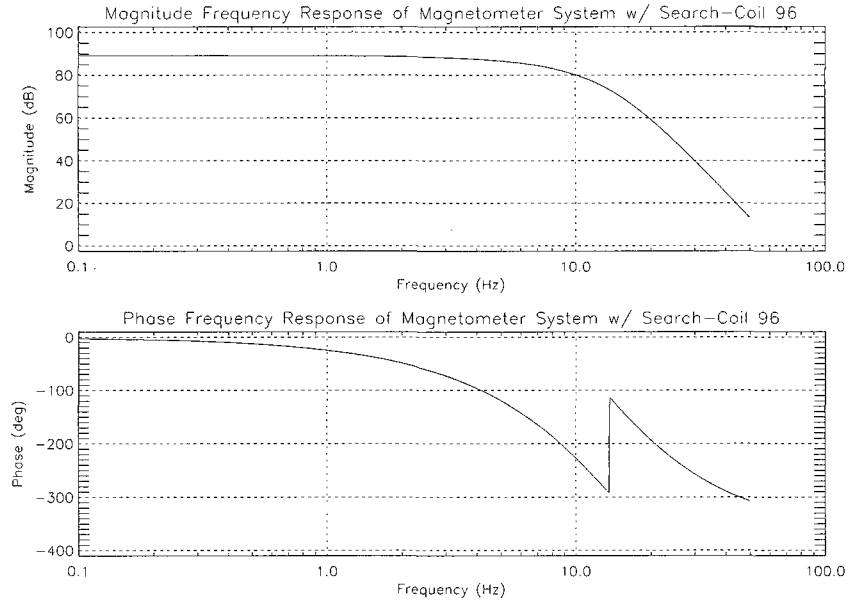

Figure B-17: Magnitude and phase frequency response of the overall magnetometer system model with the search-coil magnetic sensor.

Appendix C

The CHAMP Satellite Fluxgate Magnetometer Data Coordinate Transformation

The CHAMP data ($\mathbf{B}$) are originally given in a satellite coordinate system in which the X axis is approximately along the direction of the satellite track, the Z axis points downward (toward the center of the Earth), and the Y axis completes a right-handed set. A coordinate transformation is carried out for this study in order to examine the wave mode in the ionospheric ducting layer after the data are detrended to obtain time-varying magnetic fields ($\mathbf{b}$) by subtracting background magnetic fields ($\mathbf{B}_0$) as shown in Equation C.1 ($\mathbf{B}$ and $\mathbf{B}_0$ have to be in the identical coordinate system):

$$\mathbf{b} = \mathbf{B} - \mathbf{B}_0 \tag{C.1}$$

or by differentiating the data as shown in Equation C.2, in which the differential of $\mathbf{B}$ is obtained by subtracting a data point from another data point in a previous step and by dividing by a time step.

$$\mathbf{b} = \frac{d\mathbf{B}}{dt} = \frac{\mathbf{B}_n - \mathbf{B}_{n-1}}{t_n - t_{n-1}} \tag{C.2}$$

where n is a data point index (n=1, 2, 3). Either the IGRF model or smoothing the original data from the satellite can be used as background fields. In this study, smoothing of the original data from the satellite has been used as background field.

One of the three components in the new coordinate system represents a compressional wave component ($b_{\parallel}$). Compressional perturbations can be obtained by projecting the detrended data onto the background magnetic field. The other two components in the new coordinate system contain wave power perpendicular to the background magnetic field, which is, for this study, decomposed into perpendicular perturbations in the azimuthal ($b_{\perp\varphi}$) and in the meridional direction ($b_{\perp\theta}$), which conforms to the right-hand rule. The perpendicular azimuthal perturbation ($b_{\perp\varphi}$) is calculated by projecting the detrended data ($\mathbf{b}$) onto the azimuthal vector ($\hat{\varphi}$, normal of the magnetic meridian). The azimuthal vector ($\hat{\varphi}$) can be obtained by crossing the background magnetic field unit vector ($\mathbf{B}_0/B_0$) and the vertical field component from the original CHAMP data ($\mathbf{B}_z/B_z$) (i.e., $\hat{\varphi} = \mathbf{B}_0/B_0 \times \mathbf{B}_z/B_z$). The perpendicular meridional perturbation ($b_{\perp\theta}$), which completes the triad ($\hat{\theta} = \hat{\varphi} \times \mathbf{B}_0/B_0$), is then calculated by projecting the detrended data ($\mathbf{b}$) onto the meridional vector ($\hat{\theta}$). Figure C-1 describes the satellite coordinate system and its transformation to the new coordinate system. The new set of the three components is thus summarized as follows.

$$b_{\parallel} = \mathbf{b} \cdot \mathbf{B}_0/B_0 \tag{C.3}$$

$$b_{\perp\theta} = \mathbf{b} \cdot \hat{\theta} \tag{C.4}$$

$$b_{\perp\varphi} = \mathbf{b} \cdot \hat{\varphi} \tag{C.5}$$

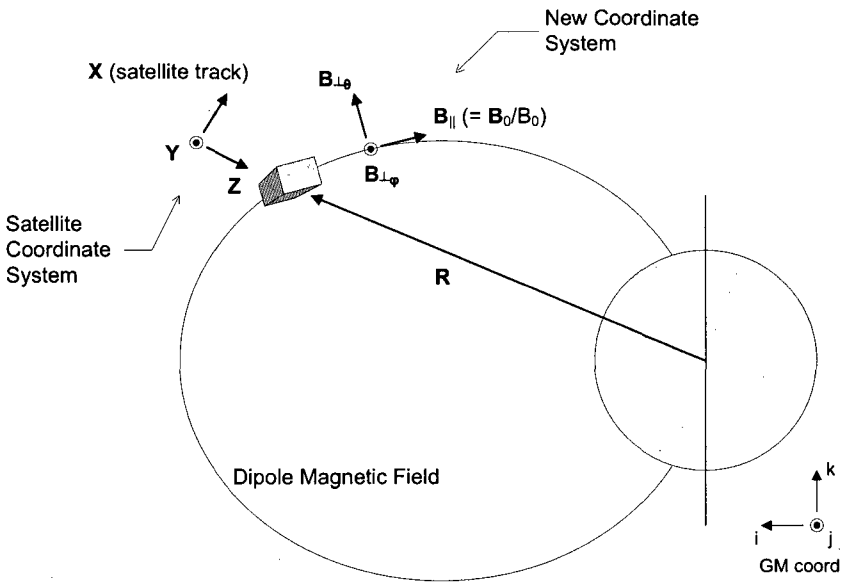

Figure C-1: Schematic diagram showing coordinate transformation from the CHAMP satellite coordinate system to the new coordinate system used in this study.

BIBLIOGRAPHY

Altman, C. & Fijalkow, E. (1980), 'The horizontal propagation of Pc1 pulsations in the ionosphere', *Planet. Space Sci.* **28**, 61–68.

Anderson, B. J., Denton, R. E., Ho, G., Hamilton, D. C., Fuselier, S. A. & Strangeway, R. J. (1996), 'Observational test of local proton cyclotron instability in the Earth's magnetosphere', *J. Geophys. Res.* **101**, 21527–21544.

Anderson, B. J., Erlandson, R. E. & Zanetti, L. J. (1992), 'A statistical study of Pc 1-2 magnetic pulsations in the equatorial magnetosphere. 1. Equatorial occurrence distributions.', *J. Geophys. Res.* **97**, 3075–3088.

Arnoldy, R. L., Dragoon, K., Cahill, Jr., L. J., Mende, S. B. & Rosenberg, T. J. (1982), 'Detailed correlations of magnetic field and riometer observations at L = 4.2 with pulsating aurora', *J. Geophys. Res.* **87**, 10449–10456.

Baker, K. B., Engebretson, M. J., Rodger, A. S. & Arnoldy, R. L. (1998), 'The coherence scale length of band-limited Pc3 pulsations in the ionosphere', *Geophys. Res. Lett.* **25**, 2357–2360.

Balanis, C. (1989), *Advanced Engineering Electomagnetics*, John and Wiley & Sons, New Jersey, USA.

Baranskiy, L. N. (1970), 'Some Characteristics of the Polarization of Pc1 Pulsations Associated with Their Waveguide Propagation', *Geomagn. and Aero.* **10**, 86–89.

Baumjohann, W. & Treumann, R. A. (1996), *Basic Space Plasma Physics*, Imperial College Press, London, UK.

Belova, E., Pchelkina, E., Lyatsky, W. & Pashin, A. (1997), 'The effect of ionospheric inhomogeneity on magnetic pulsation polarization: magnetic disturbance on the ground as a function of inhomogeneity magnitude', *J. Atmos. Solar. Terr. Phys.* **59**, 1945–1952.

Boll, R. & Overshott, K. J. (1989), *Magnetic Sensors*, Sensors, Vol. 5., VCH Publishers, New York, USA.

Bolshakova, O. V., Troitskaia, V. A. & Ivanov, K. G. (1980), 'High-latitude Pc1-2 geomagnetic pulsations and their connection with location of the dayside polar cusp', *Planet. Space Sci.* **28**, 1–7.

Born, M. & Wolf, E. (1999), *Principles of Optics 7th edition*, Cambridge University Press, New York, USA.

Brice, N. M. (1965), 'Generation of very low frequency and hydromagnetic emissions', *Nature* pp. 283–284.

Chaston, C. C., Bonnell, J. W., Carlson, C. W., Berthomier, M., Peticolas, L. M., Roth, I., McFadden, J. P., Ergun, R. E. & Strangeway, R. J. (2002), 'Electron acceleration in the ionospheric Alfven resonator', *J. Geophys. Res.* **107**, 1413.

Cornwall, J. M. (1965), 'Cyclotron Instabilities and Electromagnetic Emission in the Ultra Low Frequency and Very Low Frequency Ranges', *J. Geophys. Res.* **70**, 61–69.

Denton, R. E., Hudson, M. K. & Roth, I. (1992), 'Loss cone-driven ion cyclotron waves in the magnetosphere', *J. Geophys. Res.* **97**, 12093–12103.

Engebretson, M. J., Araki, T., Arnoldy, R. L., Carpenter, D. L., Doolittle, J. H., Fukunishi, H., Inan, U. S., LaBelle, J., Lanzerotti, L. J., Maclennan, C. G., Mende, S. B., Rosenberg, T. J., Sato, N., Sugiura, M., Taguchi, M., Wolfe, A. & Yamagishi, H. (1997), The United States Automatic Geophysical Observatory (AGO) Program in Antarctica, *in* M. Lockwood, M. N. Wild, & H. J. Opgenoorth, ed., 'Satellite-Ground Based Coordination Sourcebook', Vol. 1198 of *ESA Special Publication*, pp. 65–+.

Engebretson, M. J., Posch, J. L., Westerman, A. M., Otto, N. J., Slavin, J. A., Le, G., Strangeway, R. J. & Lessard, M. R. (2008), 'Temporal and spatial characteristics of Pc1 waves observed by ST5', *J. Geophys. Res.* **113**.

Erlandson, R. E., Mursula, K. & Bösinger, T. (1996), 'Simultaneous ground-satellite observations of structured Pc 1 pulsations', *J. Geophys. Res.* **101**, 27149–27156.

Fowler, R. A., Kotick, B. J. & Elliott, R. D. (1967), 'Polarization Analysis of Natural and Artificially Induced Geomagnetic Micropulsations', *J. Geophys. Res.* **72**, 2871–2883.

Fraser, B. J. (1975*a*), 'Ionospheric duct propagation and Pc 1 pulsation sources', *J. Geophys. Res.* **80**, 2790–2796.

Fraser, B. J. (1975*b*), 'Polarization of Pc 1 pulsations at high and middle latitudes', *J. Geophys. Res.* **80**, 2797–2807.

Fraser, B. J., Kemp, W. J. & Webster, D. J. (1989), 'Ground-satellite study of a Pc 1 ion cyclotron wave event', *J. Geophys. Res.* **94**, 11855–11863.

Fraser, B. J. & McPherron, R. L. (1982), 'Pc 1-2 magnetic pulsation spectra and heavy ion effects at synchronous orbit - ATS 6 results', *J. Geophys. Res.* **87**, 4560–4566.

Fraser, B. J. & Nguyen, T. S. (2001), 'Is the plasmapause a preferred source region of electromagnetic ion cyclotron waves in the magnetosphere?', *J. Atmos. Solar. Terr. Phys.* **63**, 1225–1247.

Fraser, B. J., Singer, H. J., Adrian, M. L., Gallagher, D. L. & Thomsen, M. F. (2005), 'The Relationship Between Plasma Density Structure and EMIC Waves at Geosynchronous Orbit', *Washington DC American Geophysical Union Geophysical Monograph Series* **159**, 55–70.

Fraser, B. J. & Summers, W. R. (1972), 'Simultaneous observations of Pc1 micropulsation polarization at four low latitude sites', *Ann. Geophys.* **28**, 697–708.

Fujita, S. (1988), 'Duct propagation of hydromagnetic waves in the upper ionosphere. II - Dispersion characteristics and loss mechanism', *J. Geophys. Res.* **93**, 14674–14682.

Fujita, S. & Tamao, T. (1988), 'Duct propagation of hydromagnetic waves in the upper ionosphere. I - Electromagnetic field disturbances in high latitudes associated with localized incidence of a shear Alfven wave', *J. Geophys. Res.* **93**, 14665–14673.

Greifinger, C. & Greifinger, P. (1973), 'Wave Guide Propagation of Micropulsations out of the Plane of the Geomagnetic Meridian', *J. Geophys. Res.* **78**, 4611–4618.

Greifinger, C. & Greifinger, P. S. (1968), 'Theory of Hydromagnetic Propagation in the Ionospheric Waveguide', *J. Geophys. Res.* **73**, 7473–7490.

Greifinger, P. (1972), 'Micropulsations from a Finite Source', *J. Geophys. Res.* **77**, 2392–2396.

Gurnett, D. A., Huff, R. L., Menietti, J. D., Burch, J. L., Winningham, J. D. & Shawhan, S. D. (1984), 'Correlated low-frequency electric and magnetic noise along the auroral field lines', *J. Geophys. Res.* **89**, 8971–8985.

Hayashi, K., Kokubun, S., Oguti, T., Tsuruda, K., Machida, S., Kitamura, T., Saka, O. & Watanabe, T. (1981), 'The extent of Pc 1 source region in high latitudes', *Can. J. Phys.* **59**, 1097–1105.

Horne, R. B. & Thorne, R. M. (1993), 'On the preferred source location for the convective amplification of ion cyclotron waves', *J. Geophys. Res.* **98**, 9233–9247.

Horne, R. B. & Thorne, R. M. (1994), 'Convective instabilities of electromagnetic ion cyclotron waves in the outer magnetosphere', *J. Geophys. Res.* **99**, 17259–17273.

Hu, Y. & Denton, R. E. (2009), 'Two-dimensional hybrid code simulation of electromagnetic ion cyclotron waves in a dipole magnetic field', *J. Geophys. Res.* **114**, 12217.

Inhester, B., Wedeken, U., Korth, A., Perraut, S. & Stokholm, M. (1984), 'Ground-satellite coordinated study of the April 5, 1979 events - Observation of O(+) cyclotron waves', *J. Geophys* **55**, 134–141.

Ivchenko, N., Marklund, G., Lynch, K., Pietrowski, D., Torbert, R., Primdahl, F. & Ranta, A. (1999), 'Quasiperiodic oscillations observed at the edge of an auroral arc by Auroral Turbulence 2', *Geophys. Res. Lett.* **26**, 3365–3368.

Iyemori, T. & Hayashi, K. (1989), 'PC 1 micropulsations observed by Magsat in the ionospheric F region', *J. Geophys. Res.* **94**, 93–100.

Iyemori, T., Sugiura, M., Oka, A., Morita, Y., Ishii, M., Slavin, J. A., Brace, L. H., Hoffman, R. A. & Winningham, J. D. (1994), 'Localized injection of large-amplitude Pc 1 waves and electron temperature enhancement near the plasmapause observed by DE2 in the upper ionosphere', *J. Geophys. Res.* **99**, 6187–6199.

Jacobs, J. A., Kato, Y., Matsushita, S. & Troitskaya, V. A. (1964), 'Classification of Geomagnetic Micropulsations', *J. Geophys. Res.* **69**, 180–181.

Jordanova, V. K., Farrugia, C. J., Thorne, R. M., Khazanov, G. V., Reeves, G. D. & Thomsen, M. F. (2001), 'Modeling ring current proton precipitation by electromagnetic ion cyclotron waves during the May 14-16, 1997, storm', *J. Geophys. Res.* **106**, 7–22.

Kangas, J., Guglielmi, A. & Pokhotelov, O. (1998), 'Morphology and physics of short-period magnetic pulsations', *Space Sci. Rev.* **83**, 435–512.

Kelley, M. C. (1989), *The Earth's Ionosphere - Plasma Physics and Electrodynamics*, Academic Press, Inc., San Diego, California, USA.

Kennel, C. F. & Petschek, H. E. (1966), 'Limit on Stably Trapped Particle Fluxes', *J. Geophys. Res.* **71**, 1–28.

Kivelson, M. G. & Russell, C. T. (1995), *Introduction to Space Physics*, Cambridge University Press, Cambridge, UK.

Klein, M. V. & Furtak, T. E. (1986), *Optics 2nd Edition*, John and Wiley & Sons, New Jersey, USA.

Kozyra, J. U., Jordanova, V. K., Horne, R. B. & Thorne, R. M. (1997), *Modeling of the Contribution of Electromagnetic Ion Cyclotron (EMIC) Waves to Stormtime Ring Current Erosion*, pp. 187–+.

Liemohn, H. B. (1967), 'Cyclotron-Resonance Amplification of VLF and ULF Whistlers', *J. Geophys. Res.* **72**, 39–55.

Lysak, R. L. (2004), 'Magnetosphere-ionosphere coupling by Alfvén waves at midlatitudes', *J. Geophys. Res.* **109**.

Manchester, R. N. (1966), 'Propagation of Pc 1 Micropulsations from High to Low Latitudes', *J. Geophys. Res.* **71**, 3749–3754.

Manchester, R. N. (1968), 'Correlation of Pc 1 Micropulsations at Spaced Stations', *J. Geophys. Res.* **73**, 3549–3556.

Manchester, R. N. (1970), 'Propagation of hydromagnetic emissions in the ionospheric duct', *Planet. Space Sci.* **18**, 299–307.

Manchester, R. N. & Fraser, B. J. (1970), 'Occurrence of hydromagnetic emissions at two southern hemisphere sites', *Planet. Space Sci.* **18**, 291–297.

Means, J. D. (1972), 'Use of the Three-Dimensional Covariance Matrix in Analyzing the Polarization Properties of Plane Waves', *J. Geophys. Res.* **77**, 5551–5559.

Meredith, N. P., Thorne, R. M., Horne, R. B., Summers, D., Fraser, B. J. & Anderson, R. R. (2003), 'Statistical analysis of relativistic electron energies for cyclotron resonance with EMIC waves observed on CRRES', *J. Geophys. Res.* **108**, 1250.

Muneer, T. (2004), *Solar Radiation and Daylight Models*, Elsevier, Boston, USA, pp. 5–20.

Mursula, K., Blomberg, L. G., Lindqvist, P., Marklund, G. T., Bräysy, T., Rasinkangas, R. & Tanskanen, P. (1994), 'Dispersive Pc1 bursts observed by Freja', *Geophys. Res. Lett.* **21**, 1851–1854.

Mursula, K., Bräysy, T., Niskala, K. & Russell, C. T. (2001), 'Pc1 pearls revisited: Structured electromagnetic ion cyclotron waves on Polar satellite and on ground', *J. Geophys. Res.* **106**, 29543–29553.

Neudegg, D. A., Fraser, B. J., Menk, F. W., Hansen, H. J., Burns, G. B., Morris, R. J. & Underwood, M. J. (1995), 'Sources and velocities of Pc1-2 ULF waves at high latitudes', *Geophys. Res. Lett.* **22**, 2965–2968.

Neudegg, D. A., Fraser, B. J., Menk, F. W., Waters, C. L., Burns, G. B. & Morris, R. J. (2000), 'ULF Wave Attenuation in the High Latitude Ionospheric Waveguide', *Adv. Space Res.* **25**, 1559–1565.

O'Brien, T. P. & Moldwin, M. B. (2003), 'Empirical plasmapause models from magnetic indices', *Geophys. Res. Lett.* **30**(4), 040000–1.

Plyasova-Bakounina, T. A., Kangas, J., Mursula, K., Molchanov, O. A. & Green, A. W. (1996), 'Pc 1-2 and Pc 4-5 pulsations observed at a network of high-latitude stations', *J. Geophys. Res.* **101**, 10965–10974.

Popecki, M., Arnoldy, R., Engebretson, M. J. & Cahill, Jr., L. J. (1993), 'High-latitude ground observations of Pc 1/2 micropulsations', *J. Geophys. Res.* **98**, 21481–21491.

Rankin, D. & Kurtz, R. (1970), 'Statistical Study of Micropulsation Polarizations', *J. Geophys. Res.* **75**, 5444–5458.

Southwood, D. J. & Hughes, W. J. (1985), 'Concerning the structure of Pi 2 pulsations', *J. Geophys. Res.* **90**, 386–392.

Summers, W. R. (1974), 'Production mechanisms for the observed behavior of the low latitude Pcl polarization ellipse', *Planet. Space Sci.* **22**, 801–809.

Summers, W. R. & Fraser, B. J. (1972), 'Polarization properties of Pc 1 micropulsations at low latitudes', *Planet. Space Sci.* **20**, 1323–1335.

Tepley, L. & Landshoff, R. K. (1966), 'Waveguide Theory for Ionospheric Propagation of Hydromagnetic Emissions', *J. Geophys. Res.* **71**, 1499–1504.

Thorne, R. M., Horne, R. B., Jordanova, V. K., Bortnik, J. & Glauert, S. (2006), Interaction of EMIC Waves With Thermal Plasma and Radiation Belt Particles, *in* K. Takahashi, P. J. Chi, R. E. Denton, & R. L. Lysak, ed., 'Magnetospheric ULF Waves: Synthesis and New Directions', Vol. 169 of *Washington DC American Geophysical Union Geophysical Monograph Series*, pp. 213–223.

Webster, D. J. & Fraser, B. J. (1985), 'Source regions of low-latitude Pcl pulsations and their relationship to the plasmapause', *Planet. Space Sci.* **33**, 777–793.

Yahnin, A. & Yahnina, T. (2007), 'Energetic proton precipitation related to ion cyclotron waves', *J. Atmos. Solar. Terr. Phys.* **69**, 1690–1706.

Young, D. T., Perraut, S., Roux, A., de Villedary, C., Gendrin, R., Korth, A., Kremser, G. & Jones, D. (1981), 'Wave-particle interactions near Ω_{He^+} observed on GEOS 1 and 2. I - Propagation of ion cyclotron waves in He^+-rich plasma', *J. Geophys. Res.* **86**, 6755–6772.